The translational landscape of SARS-CoV-2 and infected cells

Maritza Puray-Chavez[1,*], Kasyap Tenneti[1,*], Hung R. Vuong[1,*], Nakyung Lee[1], Yating Liu[2], Amjad Horani[3], Tao Huang[4], James Brett Case[5], Wei Yang[2], Michael S. Diamond[1,5,6], Steven L. Brody[4], Joseph Dougherty[2,7], Sebla B. Kutluay[1]

[1] Department of Molecular Microbiology, Washington University School of Medicine, Saint Louis, MO 63110, USA

[2] Department of Genetics, Washington University School of Medicine, Saint Louis, MO 63110, USA

[3] Department of Pediatrics, Allergy, Immunology and Pulmonary Medicine, Washington University School of Medicine, Saint Louis, MO 63110, USA

[4] Department of Medicine, Pulmonary and Critical Care Medicine, Washington University School of Medicine, Saint Louis, MO 63110, USA

[5] Department of Medicine, Infectious Disease Division, Washington University School of Medicine, Saint Louis, MO 63110, USA

[6] Department of Pathology & Immunology, Washington University School of Medicine, Saint Louis, MO 63110, USA

[7] Department of Psychiatry, Washington University School of Medicine, Saint Louis, MO 63110, USA

Correspondence: Kutluay@wustl.edu

Highlights

- Ribo-seq reveals key translationally regulated events in SARS-CoV-2 replication
- SARS-CoV-2 frameshifting is substantially more efficient than HIV-1
- SARS-CoV-2 infection results in transcriptional upregulation of inflammatory and interferon-stimulated genes
- SARS-CoV-2 disarms host responses at the level of mRNA translation

Summary

SARS-CoV-2, a betacoronavirus with a positive-sense RNA genome, has caused the ongoing COVID-19 pandemic. Although a large number of transcriptional profiling studies have been conducted in SARS-CoV-2 infected cells, little is known regarding the translational landscape of host and viral proteins. Here, using ribosome profiling in SARS-CoV-2-infected cells, we identify structural elements that regulate viral gene expression, alternative translation initiation events, as well as host responses regulated by mRNA translation. We found that the ribosome density was low within the SARS-CoV-2 frameshifting element but high immediately downstream, which suggests the utilization of a highly efficient ribosomal frameshifting strategy. In SARS-CoV-2-infected cells, although many chemokine, cytokine and interferon stimulated genes were upregulated at the mRNA level, they were not translated efficiently, suggesting a translational block that disarms host innate host responses. Together, these data reveal the key role of mRNA translation in SARS-CoV-2 replication and highlight unique mechanisms for therapeutic development.

KEYWORDS: SARS-CoV-2, ribosome profiling, ribo-seq, mRNA translation, virus replication, ribosomal frameshifting, virus-host interaction, immune response, translational repression

INTRODUCTION

The Coronavirus (CoV) group encompasses of a number of single-stranded, positive-sense RNA viruses with unusually large genomes (27-32 kb), which infect a wide range of animal species, including humans (Masters, 2006, Weiss and Navas-Martin, 2005). Previously, outbreaks of two members of this group, severe acute respiratory syndrome (SARS-CoV) and Middle East respiratory syndrome (MERS-CoV), have caused lethal respiratory illnesses in 2002 and 2012, respectively (de Wit et al., 2016). Presently, SARS-CoV-2, the causative agent of the ongoing Coronavirus Disease-2019 (COVID-19) pandemic, has infected millions of people worldwide and has devastated the global economy. Currently, there are limited options for antiviral or immunomodulatory treatment against SARS-CoV-2, with only few therapies being currently recommended for more severe COVID-19 cases. A basic understanding of the replicative mechanisms of SARS-CoV-2 and associated host responses potentially can foster the development of virus-specific therapies.

The first two-thirds of the 5' end of the SARS-CoV-2 genome is composed of two overlapping open reading frames (ORFs), ORF1a and ORF1b, which encode for two polyproteins, pp1a and pp1ab (Nakagawa et al., 2016). Pp1a is produced when translation of the genomic RNA terminates at the stop codon of ORF1a. Pp1ab is generated via a programmed -1 ribosomal frameshift (PRF) that occurs at the overlap between ORF1a and ORF1b, permitting the elongating ribosomes to bypass the termination signal in ORF1a (Plant and Dinman, 2008). Following synthesis, pp1a and pp1ab are cleaved by viral proteases to generate 15-16 mature nonstructural proteins (nsp) (Nakagawa et al., 2016). Many proteins encoded in ORF1b, are part the replication complex, thus making the -1 PRF to generate pp1ab a critical translational event for SARS-CoV-2 replication. Frameshifting in coronaviruses is regulated by a

highly conserved heptanucleotide slippery sequence (UUUAAAC) and an RNA pseudoknot structure a few nucleotides downstream (Plant and Dinman, 2008). The current models of PRF suggest that ribosomes stall upon encountering the pseudoknot (Plant et al., 2003, Korniy et al., 2019). This event presumably enhances the efficiency of ribosomal frameshifting by forcing the ribosomes to pause on the slippery sequence, which in turn promote the -1 slippage. Once the pseudoknot unwinds and resolves, the ribosome goes on to translate the alternate ORF.

Another well-known frameshifting mechanisms in human viruses is employed by retroviruses through a stem-loop structure that regulates the expression of Gag/Gag-Pol transcripts (Jacks et al., 1988, Wilson et al., 1988). Frameshifting here is thought essential for maintenance of the ratio of Gag and Gag-Pol polyproteins as well as viral infectivity (Shehu-Xhilaga et al., 2001, Garcia-Miranda et al., 2016). While frameshifting is thought to be highly inefficient in HIV-1, with only 5-10% of ribosomes continuing into the Pol ORF (Baril et al., 2003, Dulude et al., 2006, Jacks et al., 1988), CoV frameshifting is thought to occur at a much higher efficiency (Irigoyen et al., 2016). However, to date, the behavior of ribosomes within the frameshifting element for neither SARS-CoV-2 nor HIV-1 in infected cells has been empirically assessed.

In addition to hijacking the host translational machinery, SARS-CoV-2 can modulate host mRNA translation so as to suppress the immune system to ensure efficient propagation. Indeed, several viral proteins reportedly impair host gene expression post-transcriptionally (Lokugamage et al., 2012, Xiao et al., 2008, Kopecky-Bromberg et al., 2006, Huang et al., 2011, Zhou et al., 2008, Kamitani et al., 2009, Narayanan et al., 2008, Nakagawa et al., 2016). SARS-CoV nonstructural protein nsp1 induces endonucleolytic cleavage in the 5'-UTR of cellular mRNAs, accelerating their turnover,

but not in viral mRNAs (Kopecky-Bromberg et al., 2006). Furthermore, nsp1 tightly binds to the 40S ribosomal subunit and blocks translation initiation (Kamitani et al., 2009). This dual capacity to cleave host mRNAs and directly inhibit their translation may allow SARS-CoV-2 to overcome the type I IFN response in infected cells, as has been demonstrated for SARS-CoV (Narayanan et al., 2008). On the other hand, the bulk of published research on SARS-CoV- and SARS-CoV-2-host interactions has relied on transcriptional profiling to study the immune response to infection (Blanco-Melo et al., 2020, Butler et al., 2020, Menachery et al., 2014, Mitchell et al., 2013, Wilk et al., 2020, Zhou et al., 2020). Such approaches may not fully capture the host immune response to infection, in the face of viral mechanisms that block host mRNA translation.

Here, we have conducted in-depth ribosome profiling studies to gain insight into the role of translational regulation in SARS-CoV-2 replication and the resulting host responses. We found that ribosome occupancy on viral mRNAs was temporally regulated and partly dependent on RNA abundance. In addition, ribosomes engaged with novel translation initiation sites (TIS) and other potential regulatory elements on SARS-CoV-2 RNAs. Viral mRNAs encoding E, S and ORF1ab were more efficiently translated than other viral mRNAs, but the overall translation efficiency of viral mRNAs was not substantially different than cellular mRNAs. In addition, we found that ribosomes were depleted rather than enriched on the SARS-CoV-2 frameshifting site and SARS-CoV-2 frameshifting was more efficient than HIV-1. Remarkably, while numerous inflammatory chemokines, cytokines and ISGs were upregulated transcriptionally in SARS-CoV-2-infected cells, we found that many were not efficiently translated. Overall, our study defines the translational landscape of SARS-CoV-2-infected cells, revealing novel events that may promote viral replication and disarm host immune responses at the level of mRNA translation.

156 **RESULTS**

157

158 ***Ribosome profiling reveals key features of SARS-CoV-2 translational program***

159 To study the relationship between transcriptionally and translationally regulated events
160 at early and late phases of SARS-CoV-2 infection, Vero E6 cells infected at low and high
161 multiplicity of infection (MOIs, 0.1 and 2 plaque forming units [PFU]/cell, respectively))
162 were monitored by RNA-seq and ribo-seq during the course of infection (**Fig. 1A**). High
163 quality duplicate sequencing libraries with favorable mapping statistics were generated
164 (**Tables S1-S4)**. Of note, the length of sequences derived from ribo-seq ranged between
165 28-33 nucleotides (**Table S1-S4**), within the expected range of ribosome protected
166 fragments (Ingolia et al., 2012, Ingolia et al., 2009), and the majority of ribo-seq reads
167 mapped to coding sequences and 5' UTRs as expected (data not shown). For low MOI
168 infections, ~50% of the uniquely mapping RNA-seq reads were derived from SARS-CoV-
169 2 mRNAs by 24 hours post infection (hpi) (**Fig. 1B**). By 48 hpi >80% of the uniquely
170 mapping reads were viral (**Fig. 1B**) demonstrating that viral mRNAs quickly dominate the
171 total cellular mRNA pool. The percentage of SARS-CoV-2-derived mRNAs did not
172 increase further at 72 hpi (**Fig. 1B**), partly due to virus-induced cytotoxicity.
173 Comparatively, a smaller percentage of ribosome-associated mRNAs were derived from
174 SARS-CoV-2, approximating 20 to 40% at early and late time points in infection,
175 respectively (**Fig. 1C**). Despite their relative abundance in the cytosol, viral RNAs were
176 not specifically enriched in ribosome-bound pool. As we observed significant levels of
177 cytotoxicity at 72 hpi, we focused our analyses on the earlier 24 and 48 hpi time points.

178

179 Plotting of RNA-seq reads on the viral genome demonstrated that N and ORF10-derived
180 mRNAs were highly abundant throughout infection (**Fig. 1D-E, and S1**), a finding
181 consistent with previous RNA-seq studies (Kim et al., 2020, Huang et al., 2020).

182 Relatively low numbers of antisense transcripts, generally proportional to the amount of
183 sense transcripts, were also captured despite the polyA-based RNA purification (**Fig.**
184 **S1**). Furthermore, ribosomes were enriched on N mRNAs, with a high peak surrounding
185 the translation start site, at 24 hpi (**Fig. 1D**). We noted that ribosome occupancy fell
186 abruptly after the N stop codon, although footprints were still detectable within the
187 ORF10 coding sequence, with an average read count of 136 per nucleotide. A second
188 high ribosome occupancy site was observed within the M ORF at 24 hpi, again with a
189 distinct peak around the translation start site (**Fig. 1D**). ORFs downstream from S also
190 were bound by ribosomes, albeit at lower levels (**Fig. 1D**). By 48 hpi, we found that high
191 ribosome occupancy sites shifted from the N ORF to upstream ORFs, and numerous
192 high ribosome occupancy sites were observed throughout the viral RNAs (**Fig. 1E**). In
193 particular, at 48 hpi, ORF1a and ORF1b translation appeared to be particularly efficient,
194 considering the low level of mRNA abundance observed by RNA-seq (**Fig. 1E and**
195 **S2B**). Ribosome occupancy within ORF1a and ORF1b was non-uniform and did not
196 correlate with proteolytic cleavage events occurring within these polyproteins (**Fig. S2A-**
197 **B**). Ribosome footprints also were observed on antisense transcripts (**Fig. S3**), albeit
198 infrequently.
199
200 Similar to other CoVs, SARS-CoV-2 frameshifting is thought to be regulated by the
201 conserved heptanucleotide slippery sequence (UUUAAAC) and a RNA pseudoknot
202 downstream from it spanning nucleotides 13408-13540 (**Fig. 1F**). Of note, ribosome
203 occupancy was fairly low within the frameshifting site but increased immediately
204 following it (**Fig. 1G**), suggesting a relatively high efficiency of frameshifting. In addition,
205 ribosome density was also depleted ~100 nucleotides upstream of the frameshifting site
206 (**Fig. 1G**). We speculate that the pseudoknot structure may sterically hinder translating

207 ribosomes upstream of the frameshifting site or that the RNA structure may extend to
208 upstream sequences.
209
210 ***Kinetics of early translationally regulated events in SARS-CoV-2 replication***
211 To identify early translationally regulated events in SARS-CoV-2 replication, we
212 conducted similar experiments in Vero E6 cells infected at a higher MOI but monitored at
213 earlier times in infection (**Fig. 1A**). At 2 hpi, only a small fraction of mRNAs was derived
214 from SARS-CoV-2 RNAs, though by 12 hpi, nearly 80% of the total mRNA pool was viral
215 (**Fig. 2A**). Viral RNAs were more abundant in the ribosome bound pool at 2 hpi and by
216 12 hpi ~50% of the ribosome-protected fragments contained viral sequences (**Fig. 2B**).
217 As before, viral RNAs did not appear to be specifically enriched in the ribosome-bound
218 pool (**Fig. 2B**).
219
220 N and ORF10-derived sequences were the most abundant viral RNA species throughout
221 the infection (**Fig. 2C-G**) and consistent results were obtained from replicate
222 experiments (**Fig. S4-S5**). Analysis of ribosome footprints on viral RNAs at 2 hpi
223 revealed the presence of a high occupancy site (**Fig. 2C, Fig. S6A, and S7A**), which
224 accounted for the majority of ribo-seq reads derived from viral RNAs (**Fig. 2B**). This
225 region, spanning nucleotides 27371-27457 is located between ORF6 and ORF7, is not
226 fully conserved between SARS-CoV-2 and SARS-CoV (**Fig. S8A**), and is predicted to
227 form a structured hairpin loop with high probability (**Fig. S8B**). Reads that mapped to this
228 region displayed a length distribution around 29-34 nt, suggesting that they are authentic
229 ribosome protected fragments rather than aberrant products of PCR or digestion bias.
230 High ribosome occupancy in this region was maintained throughout the infection (**Fig.**
231 **S8C**) and across biological replicates (**Fig. S6A and S7A**).
232

233 Following a high MOI infection, ribosome occupancy on viral RNAs increased
234 significantly by 6 hpi, featuring N and M coding mRNAs constituting as the most
235 frequently translated RNAs (**Fig. 2D, Fig. S6B, and S7B**). Ribosome occupancy across
236 viral RNAs increased further by 12 hpi (**Fig. 2E, S6C and S7C**) and remained high
237 during the remainder of infection (**Fig. 2F, 2G, S6D, S6E, S7D and S7E**). Ribosome
238 footprints were non-uniform with numerous high and low frequency binding sites
239 observed reproducibly across viral RNAs (**Fig. 2C-G, S6, S7**). Of note, the frameshifting
240 element had a generally low ribosome density compared to the surrounding sequences
241 throughout the infection (**Fig. S9A-E**). Ribosome occupancy was low upstream of the
242 frameshifting site (**Fig. S9A-E**), again suggesting the possibility of an alternative RNA
243 structure and/or steric hindrance by the frameshifting element on translating ribosomes.
244
245 Analogous to SARS-CoV-2, HIV-1 also utilizes -1 ribosomal frameshifting, in this case
246 for generation of the Gag-Pol polyprotein (Jacks et al., 1988, Wilson et al., 1988). HIV-1
247 frameshifting is regulated by a slippery sequence followed by a structured hairpin loop
248 (Mouzakis et al., 2013, Staple and Butcher, 2005) (**Fig. S10B**). To compare the
249 frameshifting efficiency of SARS-CoV-2 to HIV-1, we next performed paired ribo-seq and
250 RNA-seq experiments in HIV-1-infected CD4+ T-cells (**Table S5 and S6**). In contrast to
251 SARS-CoV-2, ribosome occupancy was high within the HIV-1 frameshifting element but
252 dropped substantially 3' to it and remained low throughout the Pol ORF (**Fig. S10A and**
253 **10C**). This suggests that ribosomes may pause and accumulate within the frameshifting
254 site but only a small fraction of them continue translating into the Pol ORF, a finding that
255 agrees with prior estimates of low (5-10%) HIV-1 frameshifting efficiency (Biswas et al.,
256 2004, Dulude et al., 2006, Shehu-Xhilaga et al., 2001, Baril et al., 2003, Jacks et al.,
257 1988). Thus, we conclude that programmed ribosomal frameshifting is regulated through

258 distinct mechanisms between HIV-1 and SARS-CoV-2, despite the similar structural
259 elements that regulate this process.
260
261 We next tested whether SARS-CoV-2 can utilize alternative translation initiation, which is
262 increasingly recognized as a key post-transcriptional regulatory mechanism (Kwan and
263 Thompson, 2019, James and Smyth, 2018). To do so, ribo-seq experiments were
264 performed as in Fig. 2 but in the presence of harringtonine, which results in the
265 accumulation of ribosomes at translation initiation sites. In addition to accumulation of
266 ribosomes at the canonical start codons, harringtonine treatment resulted in
267 accumulation of ribosomes at alternative translation initiation sites during the course of
268 infection, albeit at generally lower frequencies. For example, at 6 hpi, an internal
269 noncanonical start codon 'UUG' within M ORF was utilized at ~30% of the time,
270 predicted to result in an out-of-frame peptide of 53 amino acids long (**Table S7**). An
271 alternative translation initiation codon 'AGG' at 21868 nt appeared to be utilized within S
272 at 6, 12 and 24 hpi, which would result in a short 18 amino acid peptide (**Table S7**).
273 Finally alternative translation initiation sites were observed within M, resulting in an out-
274 of-frame peptide and a truncated version of M (**Table S7**). Together, these results
275 provide the high resolution map of ribosomes on viral mRNAs during different stages of
276 infection and reveal key sequence and structural elements that influence SARS-CoV-2
277 translational program.
278
279 ***Ribo-seq in primary HBECs reveal a similar SARS-CoV-2 translational program***
280 To corroborate these findings in a more relevant cell culture system, we performed ribo-
281 seq studies in primary human bronchial epithelial cells (HBEC) grown at air-liquid
282 interface. Cells inoculated at an MOI of 0.5 were processed for RNA-seq and ribo-seq at
283 6, 24, 48 and 72 hpi. A parallel set of experiments were done at MOI of 1 and followed

284 during a shorter time course. In contrast to Vero cells, the progression of infection in
285 HBECs was relatively slow and a small percentage of the cells were infected (**Fig. S11**).
286 In line with this, the amount of newly synthesized viral RNAs was low at 6 hpi, although
287 by 24 hpi numerous virally derived sequences were present (**Table S8 and S9**). Similar
288 to experiments done in Vero E6 cells (**Fig. 1 and 2**), the majority of these sequences
289 were derived from subgenomic viral mRNAs coding for N and to a lesser extent
290 upstream ORFs including M, ORF6, ORF7 and ORF8 (**Fig. 3A**). The lower
291 permissiveness of these cells to infection resulted in few viral RNAs bound to ribosomes
292 at 6 hpi (**Table S8**). Ribosomes bound by viral RNAs were readily detected at 24, 48,
293 and 72 hpi, with N and M ORFs being the most frequently translated (**Fig. 3B-D**). We
294 found distinct accumulation of ribosomes within N, M and ORF1a translation start sites
295 as well as 5' end of ORF1a (**Fig. 3B-D**). Overall, these results suggest the presence of a
296 similar gene expression cascade in the primary HBECs in comparison to Vero E6 cells.
297
298 ***Inflammatory and innate immune mRNAs are inefficiently translated in SARS-CoV-***
299 ***2 infected cells***
300 Several studies have focused on the transcriptional landscape of innate responses to
301 SARS-CoV-2 (Blanco-Melo et al., 2020, Butler et al., 2020, Menachery et al., 2014,
302 Mitchell et al., 2013, Wilk et al., 2020, Zhou et al., 2020). However, currently there is little
303 evidence as to whether transcriptionally induced mRNAs are actually translated in the
304 setting of a virus that can in principle induce translational arrest (Nakagawa et al., 2016)
305 and ISGs (e.g. IFIT1 and PKR) that can inhibit mRNA translation (Li et al., 2015). Using
306 ribo-seq, we next assessed how cells respond to SARS-CoV-2 infection at a
307 translational level.
308

309 Paired RNA-seq and ribo-seq data (for high MOI infections) obtained from independent
310 and reproducible experiments (**Fig. S12**) were analyzed for differential gene expression
311 patterns. As early as 2 hpi, we found transcriptional upregulation of several chemokine
312 ligands (i.e.CXCL1, CXCL3, CXCL8) and transcription factors involved in cell cycle
313 regulation and induction of inflammation (i.e.NR4A3 and EGR3) (**Fig. 4A**). In contrast,
314 we noted a general trend in RNA downregulation (**Fig. 4A**), which persisted throughout
315 the infection (**Fig. 4B-C, and S13**). 6 hpi timepoint was also marked by upregulation of
316 chemokine ligands (CXCL1, CXCL3, CXCL8, CXCL11) (**Fig. 4B**) and by 12 hpi
317 numerous ISGs (e.g. IFIT family members, MX1, IFI44), IL1A and IFN-λ were also
318 upregulated (**Fig. 4C**). Remarkably, the majority of these transcript level changes were
319 not apparent in Ribo-seq data (**Fig. 4D-F and S14**), suggesting that mRNAs encoding
320 genes in the host defense responses may not be efficiently translated. Of note, this
321 pattern was not global. For example, EGR1, EGR3 and IFIH1, were induced at
322 equivalent levels both in RNA-seq and ribo-seq experiments (**Fig. S14**). This pattern
323 grossly continued at 24 and 48 hpi, though by 48 hpi upregulated genes were primarily
324 associated with cell death, likely reflecting viral and immune-mediated cytotoxicity (**Fig.
325 S15A, B**).
326
327 Time-course gene set enrichment analysis corroborated the differences between
328 transcriptional and translational responses in infected Vero cells. For example,
329 numerous sets of genes involved in chemokine, cytokine and interferon signaling were
330 upregulated at 2 hpi in the RNA-seq data set (**Fig. 5A**), but these changes were not
331 evident in the ribo-seq data set (**Fig. 5B**). Although at later time points both RNA-seq
332 and ribo-seq data sets were enriched in gene sets related to interferon responses,
333 inflammatory responses, IL2 and IL6 signaling, these responses appeared to be lower in
334 magnitude for ribo-seq data, with fewer genes enriched in each family and a significant

335 delay in kinetics (**Fig. 5A-B**). Together, these findings suggest that immune response
336 genes are translationally repressed and their expression significantly delayed in infected
337 cells.
338
339 Many of these findings held consistent for the low MOI infections. Analysis of
340 independent and reproducible RNA-seq (**Fig. S16A**) and Ribo-seq (Fig. **S16B**)
341 experiments revealed that transcription factors ATF3 and EGR1, key regulators of
342 inflammatory responses, were upregulated at 24 hpi alongside with numerous
343 chemokine ligands (i.e. CXCL1, CXCL8, CXCL10) and interleukin 6 (**Fig. 6A**). Of note,
344 despite the fact that Vero cells are known to be deficient in type-I IFN production, we
345 noted the upregulation of numerous ISGs (i.e. IFIT1, IFIT2, IFIT3) as well as IFN-lambda
346 at 24 hpi (**Fig. 6A**). The 48 hpi timepoint was marked by upregulation of genes involved
347 in cell cycle regulation and apoptosis (i.e. FOS, NR4A3), as well as inflammatory
348 cytokines such as IL-31 and ISGs including OASL (**Fig. 6B**). In line with our above
349 observations, the great majority of the transcriptionally upregulated genes were not
350 translationally upregulated at 24 hpi (**Fig. 6C**) and 48 hpi (**Fig.6D**). Interleukins IL11 and
351 IL1A stood out as immune-related genes that were translationally upregulated at 24 and
352 48 hpi, respectively (**Fig. 6C, D**)
353
354 Although a small percentage of cells in the primary airway culture system described
355 above were infected, analysis of differentially expressed transcripts revealed significant
356 and consistent trends in gene expression profiles upon infection. For example, we found
357 that gene sets involved in inflammatory response, interferon alpha, interferon gamma,
358 IL2 and IL6 signaling were upregulated as early as 6 hpi by RNA-seq, despite the lack of
359 observable virus replication (**Fig. S17A**). At 48 hpi, the transcriptional landscape was
360 marked by the upregulation of other sets of genes involved in IL2 and IL6 signaling,

361 inflammation, complement and hypoxia, amongst others (**Fig. S17A**). Many of these
362 responses were tuned down or non-existent in the ribo-seq data set (**Fig. S17B**),
363 suggesting that mRNA translation may similarly be repressed in this more relevant cell
364 culture system.
365
366 SARS-CoV-2 infection also induced significant alternative translation initiation from
367 numerous cellular mRNAs (**Table S10**). Of note, a highly significant increase in
368 utilization of a downstream start codon was observed within the S100A4 mRNA and an
369 mRNA coding for an unknown protein (LOC103221995) at 2 hpi (**Table S10**). Other
370 alternative translation initiation events were observed for S100A10, EXOSC7, and in
371 mRNAs coding for proteins with unknown functions including C11H12orf75 and
372 LOC103221995 as listed in Table S10. Taken together, these findings suggest that
373 alternative translation initiation may help diversify host responses and immunity.
374
375 ***Comparison of SARS-CoV-2 and host mRNA translation efficiencies***
376 We next assessed the translational efficiency of cellular host response genes in infected
377 cells and how this compared to viral mRNA translation. In mock-infected cells, most
378 cellular mRNAs were translated at levels proportional to their mRNA abundance (**Fig.**
379 **7A**). Notable outliers included mRNAs encoding for ribosomal subunits, which were
380 translated less efficiently as observed before (Riba et al., 2019), and DDX25 RNA
381 helicase, which constituted one of the most efficiently translated mRNAs (**Fig. 7A**). The
382 translational efficiency of viral mRNAs was not substantially different than the majority of
383 cellular mRNAs with ORF1AB, S and E mRNAs translated at a modestly higher
384 efficiency and the remainder of viral mRNAs at a lower efficiency than average, a pattern
385 that did not vary with progression of infection (**Fig. 7B-F**). Thus, the high abundance of
386 viral mRNAs, as opposed to a specific regulated mechanism, likely ensures the

abundance of viral proteins. Consistent with our earlier observations, we found that the differentially expressed chemokine ligands and ISGs generally were translated less efficiently (**Fig. 7C-D and S14**). Of note numerous cellular genes with unknown functions were translationally upregulated in infected cells (**Fig. 7B-F**).

DISCUSSION

Here we utilized ribosome profiling (ribo-seq) coupled with RNA-seq to study the translational events that regulate viral gene expression and host responses over the course of SARS-CoV-2 infection. SARS-CoV-2 replicates rapidly, with viral RNAs constituting the great majority of the total mRNA pool soon after infection. Our data show that viral mRNA abundance is the main determinant of viral protein expression and SARS-CoV-2 mRNAs sequester ribosomes from the translating pool by competition, simply outnumbering the host counterparts. Notwithstanding certain viral mRNAs (i.e. those encoding S, E and ORF1ab) were translated more efficiently translated than others. In addition, we show that ribosome occupancy on viral RNAs is uneven, changes during the course of infection, and alternative translation initiation sites and RNA structural elements may be utilized. Analysis of mRNA translation in infected cells uncovered that inflammatory and innate responses can be dampened by inefficient mRNA translation in SARS-CoV-2 –infected cells. Together, our study provides an in-depth picture of translationally regulated events in SARS-CoV-2 replication and reveal that impairment of host mRNA translation may allow SARS-CoV-2 to evade host immunity.

We observed that SARS-CoV-2 RNA structure is designed to employ efficient frameshifting to speed replication. Ribosomal frameshifting requires a heptanucleotide slippery sequence and a RNA pseudoknot, generally a H-type, positioned six to eight

413 nucleotides downstream (Giedroc and Cornish, 2009). Multiple models for ribosomal
414 frameshifting posit that the ribosome pauses at the slippery sequence upon
415 encountering the pseudoknot, which is resistant to unwinding (Farabaugh, 1996,
416 Dinman, 2012). While paused, ribosomes either stay in-frame or slip -1 nt before
417 resuming translation. A corollary of this notion is that the stimulatory structure, in turn,
418 enhances frameshifting efficiency by promoting ribosomal pausing. In line with this, we
419 observed low ribosome occupancy in the SARS-CoV-2 frameshifting site (**Fig. 1G and**
420 **S9**). Notably, ribosome pausing extended 100 nucleotides upstream of the frameshifting
421 site, suggesting an alternative frameshifting structure that includes upstream sequences
422 or steric hindrance imposed by the pseudoknot structure. Ribosome density downstream
423 of the frameshifting site within the ORF1b was remarkably high, suggesting high
424 efficiency of frameshifting in spite of ribosomal pausing.

425 The behavior of ribosomes was drastically different between the SARS-CoV-2 and HIV-1
426 frameshifting sites. In contrast to SARS-CoV-2, ribosomes accumulated within the HIV-1
427 frameshifting element and only a small fraction of them continued into the Pol ORF,
428 suggesting a significantly lower efficiency of frameshifting. We hypothesize that both
429 sequence-specific and structural features contribute to SARS-CoV-2 frameshifting
430 efficiency. It is thought that HIV-1 has a particularly slippery sequence (UUUUUUA) as
431 compared to SARS-CoV-2 (UUUAAAC), which may underlie this difference (Giedroc and
432 Cornish, 2009). In addition, structures downstream of the slippery sequence may have
433 an impact (Plant and Dinman, 2008). For example, the HIV-1 frameshifting element is
434 predicted to have a simpler pseudoknot (Chang et al., 1999, Parkin et al., 1992, Brierley
435 and Dos Ramos, 2006, Huang et al., 2014) or hairpin loop structure (Mouzakis et al.,
436 2013, Staple and Butcher, 2005). In particular, previous studies suggest that
437 frameshifting efficiency positively correlates with the mechanical stability and

438 thermodynamic stability of the pseudoknot and stem loop, respectively (Hansen et al.,
439 2007, Chen et al., 2009, Bidou et al., 1997). In addition, host proteins can also affect
440 frameshifting. Of note, an interferon-stimulated gene (ISG) product, known as C19orf66
441 (Shiftless), has recently been demonstrated to impair HIV-1 replication through inhibition
442 of HIV-1 programmed frameshifting (Wang et al., 2019). Altogether, our data suggest
443 that SARS-CoV-2 and HIV-1 frameshifting occurs through distinct mechanisms. It
444 remains to be determined how distinct elements within the frameshifting site affect and
445 whether other viral or cellular proteins are involved in modulating the frameshifting
446 efficiencies of these viruses.

447 SARS-CoV-2 mRNA translation may be regulated by other structural elements. For
448 example, we observed a high ribosome occupancy site that is present throughout the
449 course of infection and located between ORF6 and ORF7 (**Fig. 2C, S8**). This site is
450 computationally predicted to form a structured hairpin loop that may trigger ribosomal
451 pausing during translation of genomic viral RNA and thus lead to the observed high
452 ribosome occupancy (**Fig. S8**). Of note, ribosome occupancy within this region fell after
453 harringtonine treatment, suggesting that it may serve a function other than translation
454 initiation (not shown). While the biological role of this RNA structure is not apparent, it
455 may play a role in regulating the relative expression of ORF6 and ORF7 (depending on if
456 the structure persists in subgenomic mRNAs), or serve as a translation pause site within
457 the genomic RNA. Other potential functions of this element include co-translational
458 protein folding, protein targeting, or co-translational degradation of both mRNA and
459 nascent peptide following pausing.
460
461 In addition, our study demonstrates that alternative, non-canonical translational start
462 sites internal to several viral genes such as S, E and M, can result in truncated isoforms

463 or short peptides (**Table S7**). While their presence still needs to be validated, this raises
464 the question of whether viral protein isoforms may play important biological role during
465 infection. Utilization of alternative translational initiation sites in response to infection also
466 appeared to be utilized within host mRNAs (**Table S10**), including members of the S100
467 family, which play key roles in regulation of cell cycle progression, cell motility, invasion,
468 autophagy, angiogenesis and membrane trafficking (Donato et al., 2013, Marenholz et
469 al., 2004). Of note, extracellular S100A4 may function as a regulator of inflammation and
470 can stimulate tumor cells to secrete proinflammatory cytokines (Bettum et al., 2014, Li et
471 al., 2020). On the other hand, S100A10 may function as a pro-viral factor (Bharadwaj et
472 al., 2013, Liu et al., 2015, Taylor et al., 2018) and has also been suggested to play
473 important roles in the life cycle of numerous viruses that target epithelial cells (Taylor et
474 al., 2018).
475
476 Our study provides the first in depth picture of how host cell responses to SARS-CoV-2
477 are regulated at a post-transcriptional level. This is of utmost importance given that
478 several SARS-CoV proteins have been reported to suppress host translation and that
479 numerous genes involved in innate immunity act to block mRNA translation. Such
480 regulatory events would be completely neglected in transcriptomic screens. In fact, we
481 observed upregulation of proinflammatory chemokines as early as 2 hpi followed by a
482 more delayed induction of ISGs, a finding in line with previous observations in
483 immortalized lung cell lines (Blanco-Melo et al., 2020). However, the increase in
484 transcript abundance did not correlate with higher levels of translation and majority of
485 them appeared to be translated at a low efficiency (**Fig. 7 and S14**).
486
487 The apparent low translation efficiency of host response mRNAs may be mediated by
488 the SARS-CoV-2 protein nsp1 that was reported to associate tightly with the 40S

489 ribosomal subunit to prevent binding of capped mRNA and thus inhibit the formation of
490 the translation initiation complex (Narayanan et al., 2015). We cannot rule out that the
491 translational suppression may also be contributed by the host's attempt to curb viral
492 replication, including members of the IFIT family with known functions in translation
493 inhibition (Hyde and Diamond, 2015, Fensterl and Sen, 2015, Reynaud et al., 2015,
494 Daffis et al., 2010, Diamond and Farzan, 2013). A further alternative is that the
495 translation of these mRNAs is inherently inefficient due to presence of unique 5' UTR
496 structures.
497
498 While COVID-19 pathogenesis is in part due to virus-induced destruction of infected
499 cells, elevated production of inflammatory mediators and the virus-induced
500 immunopathology are thought to play a big role in SARS-CoV-2-induced lung injury
501 (Channappanavar and Perlman, 2017, Perlman and Dandekar, 2005). Our findings
502 suggest that immune responses in actively infected cells may be dampened or delayed
503 for SARS-CoV-2 to efficiently replicate and release viral progeny. As such, it is possible
504 that the elevated levels of inflammatory mediators in vivo is due to infection of immune
505 cell subsets, such as monocytes and macrophages, that are less permissive to SARS-
506 CoV-2 but can sense and respond to infection by secretion of immune modulatory
507 molecules (Jafarzadeh et al., 2020).
508
509 Taken together, we provide novel insight into how translational regulation shapes SARS-
510 CoV-2 replication and host responses. Our finding that induction of inflammatory and
511 innate immune responses can be limited at the level of mRNA translation provides a
512 paradigm shifting mechanism of how SARS-CoV-2 can encounter immune responses.
513 Modulation of viral RNA structures and proteins that regulate mRNA translation will
514 undoubtedly provide a unique avenue for therapeutic development.

515 **ACKNOWLEDGEMENTS:** We would like to thank members of the Diamond lab for
516 reagents and support. This work was supported by Washington University startup funds
517 for SBK, R21 AI145669 to SBK and JD, National Science Foundation Graduate
518 Research Fellowship under Grant No. DGE-1745038 to KV, Stephen I. Morse
519 postdoctoral fellowship to MPC, Helen Hay Whitney Foundation postdoctoral fellowship
520 to J.B.C., and the Dorothy R. and Hubert C. Moog Professorship to SLB.

521

522 **AUTHOR CONTRIBUTIONS:** MPC, HRV, AH, TH, JBC conducted the experiments. KT,
523 NL, YL, WY conducted the bioinformatics analysis. HRV and SBK wrote the original
524 manuscript with input from MSD, SLB, JD, JBC.

525

526 **FIGURE LEGENDS**

527 **Figure 1. Ribo-seq reveals uneven ribosome occupancy on SARS-CoV-2 RNAs**
528 **during low MOI infection.** (A) Schematic diagram of Ribo-seq and RNA-seq
529 experiments conducted in this study. Vero E6 cells were infected at 0.1 pfu/cell and cells
530 were processed for RNA-seq and Ribo-seq at 24, 48 and 72 hpi. (B, C) Percentage of
531 RNA-seq (B) and Ribo-seq (C) reads uniquely mapping to SARS-CoV-2 and cellular
532 transcripts at the indicated time points post infection. Individual data points indicate
533 biological replicates. (D, E) Ribo-seq and RNA-seq reads (counts) along the viral
534 genome at 24 hpi (D) and 48 hpi (E). Schematic diagram of SARS2 genome features
535 shown below is co-linear. Red arrows denote translation initiation sites. (F) Predicted
536 secondary structure of the frameshifting site is depicted. (G) Ribo-seq read counts at
537 48hpi within the SARS2 frameshifting site. The position of the frameshifting element is
538 indicated with the red rectangle.

539

540 **Figure 2. Changes in ribosome occupancy on the SARS-CoV-2 genome during**
541 **high MOI infection.** Vero E6 cells were infected at 2 pfu/cell and processed for RNA-
542 seq and Ribo-seq at 2, 6, 12, 24 and 48 hpi. (A, B) Percentage of RNA-seq (A) and
543 Ribo-seq (B) reads uniquely mapping to SARS-CoV-2 and cellular transcripts at the
544 indicated time points post-infection. Individual data points indicate biological replicates.
545 (C-G) Ribo-seq and RNA-seq reads (counts) mapping to the viral genome at 2 hpi (C), 6
546 hpi (D), 12 hpi (E), 24 hpi (F) and 48 hpi (G) are shown. Schematic diagram of SARS2
547 genome features illustrated below in co-linear.
548
549 **Figure 3. Ribo-seq experiments in primary HBEC cultures grown at ALI.** HBECs
550 grown at ALI were infected with SARS-CoV-2 at a MOI of 0.5 i.u./cell and processed for
551 RNA-seq at 24 hpi (A) and ribosome profiling at 24 (B), 48 (C) and 72 (D) hpi. Ribo-seq
552 reads (counts, y-axis) along the viral genome (x-axis) is shown. Schematic diagram of
553 SARS2 genome features shown below is co-linear.
554
555 **Figure 4. Differentially transcribed and translated host genes in SARS-CoV-2-**
556 **infected cells (high MOI).** Vero E6 cells were infected at 2 pfu/cell and processed for
557 RNA-seq at 2 hpi and Ribo-seq at 2 hpi (A, D), 6 hpi (B, E), and 12 hpi (C, F). Heatmaps
558 show the $\log_2$ counts per million mapped reads (cpm) of the top differentially expressed
559 genes (FDR<0.05, fold change>2) derived from two independent experiments. Scale of
560 each graph is shown below.
561
562 **Figure 5. Expression dynamics of differentially transcribed cellular mRNAs in**
563 **response to SARS-CoV-2 infection.** Time-course gene set analysis (TcGSA) was
564 performed on the RNA-seq (A) and Ribo-seq (B) data derived from the above
565 experiments. The heatmap shows an under (blue) or an over (red) expression for each

significant gene set. The numbers next to each gene set indicate a particular subset of genes which trend differently from other genes within the same gene set.

Figure 6. Differentially transcribed and translated host genes in SARS-CoV-2-infected cells (low MOI). Vero E6 cells were infected at 0.1 pfu/cell and cells were processed for RNA-seq (A, B) and Ribo-seq (C, D) at 24 and 48 hpi. Heatmaps show the counts per million mapped reads (cpm) of the top differentially expressed genes (FDR<0.05, fold change>2) derived from two independent experiments. Scale of each graph is shown below.

Figure 7. Comparison of SARS-CoV-2 and host mRNA translation efficiencies. Translation efficiencies of viral and host mRNAs were assessed as described in Materials and Methods. Plots show translational efficiencies of host mRNAs in mock infected cells (A), 2 (B), and 48hpi (C) as these samples all had low or zero viral replication, as well as viral and host mRNAs in infected cells at 6 hpi (C), 12 hpi (D) and 24 hpi (E). Translational efficiencies of key differentially expressed genes derived from RNA-seq and Ribo-seq are represented by orange circles. Reference genes with notably high and low translational efficiencies are represented by blue circles. Viral genes are represented by red circles.

592 **MATERIALS AND METHODS**

593 **Chemicals and reagents.** Standard laboratory chemicals were obtained from reputable
594 suppliers such as Sigma-Aldrich. Cycloheximide (CHX) was obtained from Sigma,
595 dissolved in ethanol and stored at -20°C. Harringtonine (HT) was purchased from LKT
596 Laboratories, Inc., resuspended in DMSO and stored in aliquots of 2 mg/mL at -20°C.
597

598 **Plasmids and viruses.** A proviral plasmid encoding the full length HIV-1 genome was
599 obtained from NIH AIDS Reagents. HIV-1 stocks were generated by transfection of
600 Human embryonic kidney cell line, HEK293T, with proviral plasmids and collection of cell
601 culture supernatants two days after. Viruses were treated by DNase to avoid plasmid
602 carryover and concentrated by Lenti-X concentrator. HIV-1 stocks were titered on TZM-
603 bl cells by conventional methods. $CD4^+$ T-cells activated for 4-5 days were used for HIV-
604 1 infections. SARS-CoV-2 strain 2019-nCoV/USA-WA1/2020 was obtained from Natalie
605 Thornburg at the Centers for Disease Control and Prevention (CDC), propagated in Vero
606 CCL-81 cells and titrated on Vero E6 cells by focus-forming assays.
607

608 **Cells and infections.** HEK293T and TZM-bl cells were obtained from ATCC and NIH
609 AIDS Reagent Program respectively and were maintained in Dulbecco's Modified
610 Eagle's Medium (DMEM) (high glucose), supplemented with 10% fetal bovine serum
611 (FBS) in a humidified incubator at 37°C with 5% CO_2. For isolation of primary $CD4^+$ T-
612 cells, buffy coats (from anonymous healthy blood donors from Mississippi Blood Center)
613 were separated by Ficoll and $CD4^+$ T-cells purified using RosetteSep Human CD4+ T-
614 cell enrichment kit (STEMCELL Technologies). $CD4^+$ T-cells cells were maintained in
615 Roswell Park Memorial Institute 1640 medium (RPMI) supplemented with 10% heat-
616 inactivated FBS and L-glutamine. Activation of $CD4^+$ T cells was achieved by addition of
617 25 U/ml of interleukin-2 (IL-2) and $CD4^+$ T-cell activation Dynabeads (Life Technologies).

618 $CD4^+$ T-cells activated for 4-5 days were used for HIV-1 infections. Vero CCL-81 and
619 Vero E6 were cultured in DMEM supplemented with 10% FBS and 10 mM HEPES pH
620 7.4. For SARS-CoV-2 infections, Vero E6 cells were incubated with SARS-CoV-2
621 inoculum in DMEM-supplemented with 2% FBS for an hour in a humidified incubator at
622 37°C, after which the initial inoculum was removed and replaced by cell culture media.
623
624 Primary human bronchial epithelial cells (HBECs) grown at air-liquid interface (ALI).
625 Human airway epithelial cells were isolated from surgical excess of tracheobronchial
626 segments of lungs donated for transplantation as previously described and were exempt
627 from regulation by US Department of Health and Human Services regulation 45 Code of
628 Federal Regulations Part 46 (Horani et al., 2012). Tracheobronchial cells were expanded
629 in culture, seeded on supported membranes (Transwell; Corning, Inc.), and
630 differentiated using ALI conditions as detailed before (You et al., 2002, Horani et al.,
631 2018).
632
633 **Ribosome profiling.** Ribosome profiling (Ribo-seq) was performed as described before
634 with the following modifications (Ingolia et al., 2009, Ingolia et al., 2012). Mock- and HIV-
635 1- or SARS-CoV-2-infected cells were treated with complete cell culture media
636 supplemented with 0.1 mg/mL CHX for 1 min at room temperature followed by one
637 round of wash in ice-cold PBS supplemented with 0.1 mg/mL CHX. Cells were lysed in
638 1X mammalian polysome lysis buffer (20 mM Tris·HCl (pH 7.4), 150 mM NaCl, 5 mM
639 $MgCl_2$, 1% Triton X-100, 0.1% NP-40, 1 mM DTT, 10 units of DNase I, with 0.1 mg/mL
640 CHX). The cells were then triturated by repeated pipetting and incubated with lysis buffer
641 for at least 20 min to ensure virus inactivation. Lysates were centrifuged for 10 min at
642 ≥20,000 g at 4°C for clarification. The supernatants were split into multiple aliquots, with
643 SDS added to one aliquot to a final concentration of 1% for downstream RNA-seq

644 sample preparation, and flash frozen in a 70% ethanol/dry ice bath or directly placed at -
645 80°C. Lysates were treated with RNase I (5U/OD_{260}) and ribosome-protected fragments
646 were isolated via centrifugation through Microspin S-400 HR columns (GE Healthcare)
647 and purified using the RNA Clean and Concentrator kit (Zymo Research). Recovered
648 ribosome-bound fragments (RBFs) are then subjected to rRNA depletion using RiboZero
649 beads from the TruSeq Stranded Total RNA Library Prep Gold kit (Illumina) and purified
650 using Zymo RNA Clean and Concentrator kit. Fragments were then end-labeled with γ-
651 ^{32}P-ATP using T4 polynucleotide kinase (NEB), separated on 15% TBE-Urea gels and
652 visualized by autoradiography. RNA fragments of ~30 nt were excised from the gels and
653 purified as detailed before in 400 µL of 0.4 M NaCl supplemented with 4 µL
654 SUPERaseIN. 3' and 5' adapters were sequentially ligated as in a previously described
655 protocol (Kutluay et al., 2014, Kutluay and Bieniasz, 2016), reverse transcribed and PCR
656 amplified. Libraries were then sequenced on HiSeq-2000 or NextSeq 500 platforms
657 (Illumina) at the Genome Technology Access Center or the Edison Family Center for
658 Genome Sciences & Systems Biology, respectively, at Washington University School of
659 Medicine.
660
661 **RNA-seq.** An aliquot of cell lysates harvested from ribosome profiling (Ribo-seq)
662 experiments above was processed in parallel for RNA-seq using TruSeq Stranded
663 mRNA library prep (Illumina). RNA-seq libraries were constructed using TruSeq RNA
664 single-index adapters and deep sequenced as above at Washington University in St.
665 Louis.
666
667 **Data analysis.**
668

669 ***Mapping.*** Generated RNA-seq and Ribo-seq data were analyzed by publicly available
670 software and custom scripts. In brief, for Ribo-seq, reads were separated based on
671 barcodes and the adapters trimmed using BBDuk (http://jgi.doe.gov/data-and-
672 tools/bb-tools/) and FastX Toolkit (http://hannonlab.cshl.edu/fastx_toolkit/). The
673 resulting reads were mapped to the viral genome/transcriptome using the Bowtie aligner
674 (Langmead et al., 2009), and to the African green monkey (AGM) genome (*Chlorocebus*
675 *sabaeus*) in STAR (Dobin et al., 2013). For AGM alignments, reads were first mapped
676 to rRNA to remove any rRNA-derived reads not completely removed by depletion kits,
677 and then mapped to the AGM genome. RNA-seq reads were similarly mapped to the
678 viral and AGM genomes using STAR, although the rRNA alignment step was omitted.
679 For AGM alignments, mapped reads were annotated using the featureCounts package
680 and GTF files freely available from NCBI and Ensembl.
681
682 ***Statistical Analysis:*** Differential gene expression analysis was carried out using the
683 featureCounts output files via the edgeR package (Robinson et al., 2010), available from
684 Bioconductor. Efforts in this area focused on determining upregulated genes using
685 individual Ribo-seq and RNA-seq experiments, as well as the analysis of log-fold change
686 differences between Ribo-seq and RNA-seq to discover translationally regulated genes.
687 These same files and packages were also used to generate quality control plots and
688 graphics highlighting differentially expressed genes. The calculation of translational
689 efficiency involved normalizing counts to account for library size in edgeR to generate
690 log2 counts-per-million ($\log_2$CPM) estimates for each gene in Ribo-seq and RNA-seq,
691 and subtracting log2CPM RNA-seq from log2CPM Ribo-seq to provide an estimate of
692 the difference in expression level between Ribo-seq and RNA-seq for a given gene.
693

694 Additionally, the R package TcGSA was used to determine individual host genes and
695 gene sets differentially regulated over time (Hejblum et al., 2015). The normalized gene
696 counts at each time-point were provided as input, along with the 'hallmark' Gene Matrix
697 file containing annotated sets of processes and associated genes, downloaded from
698 GSEA (Subramanian et al., 2005, Mootha et al., 2003). As output, the program provides
699 clusters of genes within each gene set, which follow particular trends. From these
700 clusters, individual genes differentially regulated over time were extracted and plotted as
701 heatmaps in R.
702
703 Downstream analysis of sets of differential genes involved the use of goseq (Young et
704 al., 2010) and KEGGREST R packages (Tenenbaum, 2020). These programs use a list
705 of differential genes generated by edgeR to provide gene ontology analysis and enriched
706 biochemical pathways. Additionally, the R package biomart was used to retrieve
707 annotations and generate counts within the UTRs of human genes, after removing
708 repetitive low-complexity elements such as LINEs and retroviral sequences using the
709 hg19RepeatMasker GTF from UCSC. The R package riboWaltz (Lauria et al., 2018)
710 was utilized to determine the location of ribosomal P-sites with respect to the 5' end of
711 reads, as well as illustrating triplet periodicity and determining the percentage of reads
712 within each frame in CDS and UTR . Finally, the metagene R package (Beauparlant,
713 2020) was applied to generate an aggregate analysis of ribosomal density downstream
714 of start codons and upstream of stop codons in the corresponding genome.
715
716 Alternative TIS sites in both host and viral reads were found using the Ribo-TISH
717 package (Zhang et al., 2017). For viral TIS, analysis was carried out in the 'predict' mode
718 comparing samples mock-treated or treated with harringtonine at each timepoint (with
719 replicates). This was replicated for host analysis, although with the additional step of

720 analysis in the 'diff' mode to predict TIS differentially regulated between infected and
721 uninfected cells.
722
723 ***Viral Counts:*** Viral read density plots were generated using the SAM file from viral
724 genome alignment. The SAMtools (Li et al., 2009) package was used to create an
725 mpileup file containing information about the read density, strandedness, mapping
726 quality, and nucleotide identity at each position. Custom scripts then were utilized to
727 create files providing only the nucleotide identity and number of counts at each position
728 for both sense and antisense reads. These were then visualized by scripts written in R.
729
730 As SARS-CoV-2 generates chimeric subgenomic mRNAs (sgRNAs) in addition to its
731 genomic RNA (gRNA), featureCounts could not be used to accurately estimate viral
732 gene counts from RNASeq due to the presence of nested 3' sequences. Therefore, in
733 order to visualize and enumerate such chimeric sequences the BWA aligner (Li and
734 Durbin, 2009) was used in 'mem' mode on viral RNASeq reads. After generating this
735 alignment using the default parameters and same reference SARS-CoV-2 FASTA file as
736 above, chimeric reads were isolated by searching for all reads containing the 'SA' tag
737 and the SARS TRS sequence, 'AAACGAAC'. SARS-CoV-2 gRNAs were extracted by
738 searching for all reads containing the first 15-20 bases of the ORF1A coding sequence
739 (CDS), as these sequences would only be present in full-length SARS-CoV-2 genomes.
740 This provided the sequences and alignment locations of the chimeric and genomic
741 reads, which were then visualized using R. For sgRNAs, the viral gene corresponding to
742 each transcript was determined by locating the CDS with the nearest downstream start
743 site. This data, together with the number of gRNAs was used to calculate relative
744 percentages of viral transcripts and, together with the total number of mapped viral
745 reads, allowed for the tabulation of viral gene counts at each time point. For ribosome

746 profiling data, featureCounts was used to enumerate the number of viral reads, as
747 ribosomes only translate the first gene on each transcript and so footprints from nested
748 3' gene were low enough to be negligible.
749
750
751
752
753
754
755
756
757
758
759
760
761
762
763
764
765
766
767
768
769
770
771

SUPPLEMENTARY FIGURE LEGENDS

Figure S1. RNA-seq on sense and antisense SARS-CoV-2 transcripts during low MOI infection (Supplemental to Figure 1). Data derived from experiments described in Figure 1 and a replicate experiment were plotted to demonstrate the number of reads that map to sense vs. antisense transcripts at 24 (A) and 48 (B) hpi. Schematic diagram of SARS-CoV-2 genome features shown below is co-linear.

Figure S2. Ribosome occupancy on the SARS-CoV-2 genome during low MOI infection (Supplemental to Figure 1). Vero E6 cells were infected at 0.1 pfu/cell and cells were processed for RNA-seq and Ribo-seq as in Figure 1. Ribo-seq and RNA-seq reads (counts) mapping to the first 20000 nucleotides (ORF1ab) of the viral genome at 24 (A) and 48 (B) hpi with constituent non-structural proteins (NSPs) shown below is co-linear.

Figure S3. Ribosome occupancy on sense and antisense SARS-CoV-2 transcripts during low MOI infection (Supplemental to Figure 1). Ribo-seq data derived from the two independent experiments described in Figure 1 were plotted to demonstrate the number of reads mapping to sense and antisense transcripts at 24 (A, C) and 48 (B, D) hpi. Schematic diagram of SARS2 genome features shown below is co-linear.

Figure S4. RNA-seq on sense and antisense SARS-CoV-2 transcripts during high MOI infection (Supplemental to Figure 2). RNA-seq data derived from experiments described in Figure 1 were plotted to demonstrate the number of reads that map to sense and. antisense transcripts at 2 hpi (A), 6 hpi (B), 12 hpi (C), 24 hpi (D) and 48 hpi (E). Schematic diagram of SARS2 genome features shown below is co-linear.

798 **Figure S5. Reproducibility of RNA-seq experiments (Supplemental to Figure 2).**
799 RNA-seq data derived from a replicate experiment described in Figure 1 were plotted to
800 demonstrate the number of reads that map to sense vs. antisense transcripts at 2 hpi
801 (A), 6 hpi (B), 12 hpi (C), 24 hpi (D) and 48 hpi (E). Schematic diagram of SARS2
802 genome features shown below is co-linear.
803
804 **Figure S6. Ribosome occupancy on sense and antisense SARS-CoV-2 transcripts**
805 **during high MOI infection (Supplemental to Figure 2).** Ribo-seq data derived from
806 experiments described in Figure 1 were plotted to demonstrate the number of reads that
807 map to sense vs. antisense transcripts at 2 hpi (A), 6 hpi (B), 12 hpi (C), 24 hpi (D) and
808 48 hpi (E). Schematic diagram of SARS2 genome features shown below is co-linear.
809
810 **Figure S7. Reproducibility of Ribo-seq experiments (Supplemental to Figure 2).**
811 Ribo-seq data derived from a replicate experiment described in Figure 1 were plotted to
812 demonstrate the number of reads that map to sense vs. antisense transcripts at 2 hpi
813 (A), 6 hpi (B), 12 hpi (C), 24 hpi (D) and 48 hpi (E). Schematic diagram of SARS2
814 genome features shown below is co-linear.
815
816 **Figure S8. Properties of the high ribosome occupancy site located between 27371-**
817 **27457 nt (supplemental to Figure 2).** (A) Sequence homology of the high ribosome
818 occupancy site between SARS-CoV-2 27371-27457nts and SARS-CoV (27243-27336).
819 (B) Predicted secondary structure of the SARS-CoV-2 sequence at 27371-27457nts
820 using RNAstructure. (C) Ribosome occupancy surrounding nucleotides 27371-27457 at
821 the indicated time points post-infection.
822

823 **Figure S9. Ribosome occupancy remains low within the SARS-CoV-2**
824 **frameshifting site throughout infection (supplemental to Figure 2).** Ribosome
825 occupancy surrounding and within the frameshifting site at the indicated time points
826 post-infection (derived from Ribo-seq experiments in Figure 2) is shown. Red bars
827 indicate the position of the frameshifting element.
828
829 **Figure S10. RIbo-seq in HIV-1-infected cells reveals structural elements that**
830 **regulate translation (supplemental to Figure 2).** Primary CD4+ T-cells were infected
831 with HIV-1_{NL4-3}/VSV-G at an MOI of 2 and infected cells processed for RNA-seq and
832 Ribo-seq at 24 hpi. (A) Ribo-seq and RNA-seq reads (counts) mapping to the HIV-1
833 genome is shown. Schematic diagram of HIV-1 genome features shown below is co-
834 linear. (B) Secondary structure prediction of the HIV-1 ribosome frameshifting element is
835 shown. (C) Ribosome occupancy within the frameshifting site is shown.
836
837 **Figure S11. SARS-CoV-2 infection of primary HBECs grown at ALI (supplemental**
838 **to Figure 3).** Primary HBEC cultures were infected with SARS-CoV-2 at an MOI of 0.5
839 i.u./cell and fixed at 72 hpi. Cells were probed with anti-spike (anti-S) and anti-
840 nucleoprotein (anti-N) antibodies and imaged by microscopy.
841
842 **Figure S12. Reproducibility of RNA-seq and ribo-seq data sets (supplemental to**
843 **Figure 4). (A)** Correlation of $\log_2$(counts per million mapped reads) for each gene
844 derived from RNA-seq experiments is shown. **(B)** Correlation of $\log_2$ counts per million
845 mapped reads for each gene derived from ribo-seq experiments is shown.
846
847 **Figure S13. SARS-CoV-2 infection induces a general decrease in host mRNA**
848 **expression (high MOI, supplemental to Figure 4).** Vero E6 cells were infected at 2

849 pfu/cell and cells were processed for RNA-seq. Volcano plots show the log_2 fold-change
850 (x-axis) vs. significance (-log(Pvalue), y-axis) of host genes at 2 hpi (A), 6 hpi (B), 12 hpi
851 (C), 24 hpi (D) and 48 hpi (E). Top differentially expressed genes (FDR<0.05, fold
852 change>2) are indicated by blue dots.
853
854 **Figure S14. SARS-CoV-2 infection results in lower translation rates for mRNAs**
855 **coding for immune responses (supplemental to Figure 4).** Expression levels (fold
856 change over mock) of select immune-related mRNAs that were significantly upregulated
857 in RNA-seq data set were compared to expression levels derived from ribo-seq data set.
858
859 **Figure S15. Differentially transcribed and translated host genes in SARS-CoV-2-**
860 **infected cells (supplemental to Figure 4).** Vero E6 cells were infected at 2 pfu/cell and
861 processed for RNA-seq at 2 hpi and Ribo-seq at 24 hpi (A, C) and 48 hpi (B, D).
862 Heatmaps show the log_2 counts per million mapped reads (cpm) of the top differentially
863 expressed genes (FDR<0.05, fold change>2) derived from two independent
864 experiments. Scale of each graph is shown below.
865
866 **Figure S16. Reproducibility of RNA-seq and ribo-seq data sets (supplemental to**
867 **Figure 7). (A)** Correlation of log_2(counts per million mapped reads) for each gene
868 derived from RNA-seq experiments (low MOI) is shown. **(B)** Correlation of log_2 counts
869 per million mapped reads for each gene derived from ribo-seq experiments (low MOI) is
870 shown.
871
872 **Figure S17. Transcriptional responses of HBECs to SARS-CoV-2.** HBECs grown at
873 ALI were infected with SARS-CoV-2 at a MOI of 0.5 i.u./cell and processed for RNA-seq

874 (A) and ribo-seq (B) at 6, 24 and 48 hpi. Data were analyzed for trends in gene set
875 enrichment over the period of infection.
876
877
878
879
880
881
882
883
884
885
886
887
888
889
890
891
892
893
894
895
896
897
898
899

REFERENCES

BARIL, M., DULUDE, D., GENDRON, K., LEMAY, G. & BRAKIER-GINGRAS, L. 2003. Efficiency of a programmed -1 ribosomal frameshift in the different subtypes of the human immunodeficiency virus type 1 group M. *RNA,* 9**,** 1246-53.

BEAUPARLANT, C. J., LAMAZE, F.C., SAMB, R., LIPPENS, C., DESCHENES, A.L., DROIT, A. 2020. metagene: A package to produce metagene plots. R package version 2.20.0. .

BETTUM, I. J., VASILIAUSKAITE, K., NYGAARD, V., CLANCY, T., PETTERSEN, S. J., TENSTAD, E., MAELANDSMO, G. M. & PRASMICKAITE, L. 2014. Metastasis-associated protein S100A4 induces a network of inflammatory cytokines that activate stromal cells to acquire pro-tumorigenic properties. *Cancer Lett,* 344**,** 28-39.

BHARADWAJ, A., BYDOUN, M., HOLLOWAY, R. & WAISMAN, D. 2013. Annexin A2 heterotetramer: structure and function. *Int J Mol Sci,* 14**,** 6259-305.

BIDOU, L., STAHL, G., GRIMA, B., LIU, H., CASSAN, M. & ROUSSET, J. P. 1997. In vivo HIV-1 frameshifting efficiency is directly related to the stability of the stem-loop stimulatory signal. *RNA,* 3**,** 1153-8.

BISWAS, P., JIANG, X., PACCHIA, A. L., DOUGHERTY, J. P. & PELTZ, S. W. 2004. The human immunodeficiency virus type 1 ribosomal frameshifting site is an invariant sequence determinant and an important target for antiviral therapy. *J Virol,* 78**,** 2082-7.

BLANCO-MELO, D., NILSSON-PAYANT, B. E., LIU, W. C., UHL, S., HOAGLAND, D., MOLLER, R., JORDAN, T. X., OISHI, K., PANIS, M., SACHS, D., WANG, T. T., SCHWARTZ, R. E., LIM, J. K., ALBRECHT, R. A. & TENOEVER, B. R. 2020. Imbalanced Host Response to SARS-CoV-2 Drives Development of COVID-19. *Cell,* 181**,** 1036-1045 e9.

BRIERLEY, I. & DOS RAMOS, F. J. 2006. Programmed ribosomal frameshifting in HIV-1 and the SARS-CoV. *Virus Res,* 119**,** 29-42.

BUTLER, D. J., MOZSARY, C., MEYDAN, C., DANKO, D., FOOX, J., ROSIENE, J., SHAIBER, A., AFSHINNEKOO, E., MACKAY, M., SEDLAZECK, F. J., IVANOV, N. A., SIERRA, M., POHLE, D., ZIETZ, M., GISLADOTTIR, U., RAMLALL, V., WESTOVER, C. D., RYON, K., YOUNG, B., BHATTACHARYA, C., RUGGIERO, P., LANGHORST, B. W., TANNER, N., GAWRYS, J., MELESHKO, D., XU, D., STEEL, P. A. D., SHEMESH, A. J., XIANG, J., THIERRY-MIEG, J., THIERRY-MIEG, D., SCHWARTZ, R. E., IFTNER, A., BEZDAN, D., SIPLEY, J., CONG, L., CRANEY, A., VELU, P., MELNICK, A. M., HAJIRASOULIHA, I., HORNER, S. M., IFTNER, T., SALVATORE, M., LODA, M., WESTBLADE, L. F., CUSHING, M., LEVY, S., WU, S., TATONETTI, N., IMIELINSKI, M., RENNERT, H. & MASON, C. E. 2020. Shotgun Transcriptome and Isothermal Profiling of SARS-CoV-2 Infection Reveals Unique Host Responses, Viral Diversification, and Drug Interactions. *bioRxiv*.

CHANG, S. Y., SUTTHENT, R., AUEWARAKUL, P., APICHARTPIYAKUL, C., ESSEX, M. & LEE, T. H. 1999. Differential stability of the mRNA secondary structures in the frameshift site of various HIV type 1 viruses. *AIDS Res Hum Retroviruses,* 15**,** 1591-6.

CHANNAPPANAVAR, R. & PERLMAN, S. 2017. Pathogenic human coronavirus infections: causes and consequences of cytokine storm and immunopathology. *Semin Immunopathol,* 39**,** 529-539.

CHEN, G., CHANG, K. Y., CHOU, M. Y., BUSTAMANTE, C. & TINOCO, I., JR. 2009. Triplex structures in an RNA pseudoknot enhance mechanical stability and

950 increase efficiency of -1 ribosomal frameshifting. *Proc Natl Acad Sci U S A,* 106**,**
951 12706-11.
952 DAFFIS, S., SZRETTER, K. J., SCHRIEWER, J., LI, J., YOUN, S., ERRETT, J., LIN, T.
953 Y., SCHNELLER, S., ZUST, R., DONG, H., THIEL, V., SEN, G. C., FENSTERL,
954 V., KLIMSTRA, W. B., PIERSON, T. C., BULLER, R. M., GALE, M., JR., SHI, P.
955 Y. & DIAMOND, M. S. 2010. 2'-O methylation of the viral mRNA cap evades host
956 restriction by IFIT family members. *Nature,* 468**,** 452-6.
957 DE WIT, E., VAN DOREMALEN, N., FALZARANO, D. & MUNSTER, V. J. 2016. SARS
958 and MERS: recent insights into emerging coronaviruses. *Nat Rev Microbiol,* 14**,**
959 523-34.
960 DIAMOND, M. S. & FARZAN, M. 2013. The broad-spectrum antiviral functions of IFIT
961 and IFITM proteins. *Nat Rev Immunol,* 13**,** 46-57.
962 DINMAN, J. D. 2012. Mechanisms and implications of programmed translational
963 frameshifting. *Wiley Interdiscip Rev RNA,* 3**,** 661-73.
964 DOBIN, A., DAVIS, C. A., SCHLESINGER, F., DRENKOW, J., ZALESKI, C., JHA, S.,
965 BATUT, P., CHAISSON, M. & GINGERAS, T. R. 2013. STAR: ultrafast universal
966 RNA-seq aligner. *Bioinformatics,* 29**,** 15-21.
967 DONATO, R., CANNON, B. R., SORCI, G., RIUZZI, F., HSU, K., WEBER, D. J. &
968 GECZY, C. L. 2013. Functions of S100 proteins. *Curr Mol Med,* 13**,** 24-57.
969 DULUDE, D., BERCHICHE, Y. A., GENDRON, K., BRAKIER-GINGRAS, L. &
970 HEVEKER, N. 2006. Decreasing the frameshift efficiency translates into an
971 equivalent reduction of the replication of the human immunodeficiency virus type
972 1. *Virology,* 345**,** 127-36.
973 FARABAUGH, P. J. 1996. Programmed translational frameshifting. *Microbiol Rev,* 60**,**
974 103-34.
975 FENSTERL, V. & SEN, G. C. 2015. Interferon-induced Ifit proteins: their role in viral
976 pathogenesis. *J Virol,* 89**,** 2462-8.
977 GARCIA-MIRANDA, P., BECKER, J. T., BENNER, B. E., BLUME, A., SHERER, N. M. &
978 BUTCHER, S. E. 2016. Stability of HIV Frameshift Site RNA Correlates with
979 Frameshift Efficiency and Decreased Virus Infectivity. *J Virol,* 90**,** 6906-6917.
980 GIEDROC, D. P. & CORNISH, P. V. 2009. Frameshifting RNA pseudoknots: structure
981 and mechanism. *Virus Res,* 139**,** 193-208.
982 HANSEN, T. M., REIHANI, S. N., ODDERSHEDE, L. B. & SORENSEN, M. A. 2007.
983 Correlation between mechanical strength of messenger RNA pseudoknots and
984 ribosomal frameshifting. *Proc Natl Acad Sci U S A,* 104**,** 5830-5.
985 HEJBLUM, B. P., SKINNER, J. & THIEBAUT, R. 2015. Time-Course Gene Set Analysis
986 for Longitudinal Gene Expression Data. *PLoS Comput Biol,* 11**,** e1004310.
987 HORANI, A., DRULEY, T. E., ZARIWALA, M. A., PATEL, A. C., LEVINSON, B. T., VAN
988 ARENDONK, L. G., THORNTON, K. C., GIACALONE, J. C., ALBEE, A. J.,
989 WILSON, K. S., TURNER, E. H., NICKERSON, D. A., SHENDURE, J., BAYLY,
990 P. V., LEIGH, M. W., KNOWLES, M. R., BRODY, S. L., DUTCHER, S. K. &
991 FERKOL, T. W. 2012. Whole-exome capture and sequencing identifies HEATR2
992 mutation as a cause of primary ciliary dyskinesia. *Am J Hum Genet,* 91**,** 685-93.
993 HORANI, A., USTIONE, A., HUANG, T., FIRTH, A. L., PAN, J., GUNSTEN, S. P.,
994 HASPEL, J. A., PISTON, D. W. & BRODY, S. L. 2018. Establishment of the early
995 cilia preassembly protein complex during motile ciliogenesis. *Proc Natl Acad Sci*
996 *U S A,* 115**,** E1221-E1228.
997 HUANG, C., LOKUGAMAGE, K. G., ROZOVICS, J. M., NARAYANAN, K., SEMLER, B.
998 L. & MAKINO, S. 2011. SARS coronavirus nsp1 protein induces template-
999 dependent endonucleolytic cleavage of mRNAs: viral mRNAs are resistant to
1000 nsp1-induced RNA cleavage. *PLoS Pathog,* 7**,** e1002433.

1001 HUANG, J., HUME, A. J., ABO, K. M., WERDER, R. B., VILLACORTA-MARTIN, C.,
1002 ALYSANDRATOS, K. D., BEERMANN, M. L., SIMONE-ROACH, C., OLEJNIK,
1003 J., SUDER, E. L., BULLITT, E., HINDS, A., SHARMA, A., BOSMANN, M.,
1004 WANG, R., HAWKINS, F., BURKS, E. J., SAEED, M., WILSON, A. A.,
1005 MUHLBERGER, E. & KOTTON, D. N. 2020. SARS-CoV-2 Infection of Pluripotent
1006 Stem Cell-derived Human Lung Alveolar Type 2 Cells Elicits a Rapid Epithelial-
1007 Intrinsic Inflammatory Response. *bioRxiv*.
1008 HUANG, X., YANG, Y., WANG, G., CHENG, Q. & DU, Z. 2014. Highly conserved RNA
1009 pseudoknots at the Gag-Pol junction of HIV-1 suggest a novel mechanism of -1
1010 ribosomal frameshifting. *RNA,* 20**,** 587-93.
1011 HYDE, J. L. & DIAMOND, M. S. 2015. Innate immune restriction and antagonism of viral
1012 RNA lacking 2-O methylation. *Virology,* 479-480**,** 66-74.
1013 INGOLIA, N. T., BRAR, G. A., ROUSKIN, S., MCGEACHY, A. M. & WEISSMAN, J. S.
1014 2012. The ribosome profiling strategy for monitoring translation in vivo by deep
1015 sequencing of ribosome-protected mRNA fragments. *Nat Protoc,* 7**,** 1534-50.
1016 INGOLIA, N. T., GHAEMMAGHAMI, S., NEWMAN, J. R. & WEISSMAN, J. S. 2009.
1017 Genome-wide analysis in vivo of translation with nucleotide resolution using
1018 ribosome profiling. *Science,* 324**,** 218-23.
1019 IRIGOYEN, N., FIRTH, A. E., JONES, J. D., CHUNG, B. Y., SIDDELL, S. G. &
1020 BRIERLEY, I. 2016. High-Resolution Analysis of Coronavirus Gene Expression
1021 by RNA Sequencing and Ribosome Profiling. *PLoS Pathog,* 12**,** e1005473.
1022 JACKS, T., POWER, M. D., MASIARZ, F. R., LUCIW, P. A., BARR, P. J. & VARMUS, H.
1023 E. 1988. Characterization of ribosomal frameshifting in HIV-1 gag-pol expression.
1024 *Nature,* 331**,** 280-3.
1025 JAFARZADEH, A., CHAUHAN, P., SAHA, B., JAFARZADEH, S. & NEMATI, M. 2020.
1026 Contribution of monocytes and macrophages to the local tissue inflammation and
1027 cytokine storm in COVID-19: Lessons from SARS and MERS, and potential
1028 therapeutic interventions. *Life Sci***,** 118102.
1029 JAMES, C. C. & SMYTH, J. W. 2018. Alternative mechanisms of translation initiation: An
1030 emerging dynamic regulator of the proteome in health and disease. *Life Sci,* 212**,**
1031 138-144.
1032 KAMITANI, W., HUANG, C., NARAYANAN, K., LOKUGAMAGE, K. G. & MAKINO, S.
1033 2009. A two-pronged strategy to suppress host protein synthesis by SARS
1034 coronavirus Nsp1 protein. *Nat Struct Mol Biol,* 16**,** 1134-40.
1035 KIM, D., LEE, J. Y., YANG, J. S., KIM, J. W., KIM, V. N. & CHANG, H. 2020. The
1036 Architecture of SARS-CoV-2 Transcriptome. *Cell,* 181**,** 914-921 e10.
1037 KOPECKY-BROMBERG, S. A., MARTINEZ-SOBRIDO, L. & PALESE, P. 2006. 7a
1038 protein of severe acute respiratory syndrome coronavirus inhibits cellular protein
1039 synthesis and activates p38 mitogen-activated protein kinase. *J Virol,* 80**,** 785-93.
1040 KORNIY, N., SAMATOVA, E., ANOKHINA, M. M., PESKE, F. & RODNINA, M. V. 2019.
1041 Mechanisms and biomedical implications of -1 programmed ribosome
1042 frameshifting on viral and bacterial mRNAs. *FEBS Lett,* 593**,** 1468-1482.
1043 KUTLUAY, S. B. & BIENIASZ, P. D. 2016. Analysis of HIV-1 Gag-RNA Interactions in
1044 Cells and Virions by CLIP-seq. *Methods Mol Biol,* 1354**,** 119-31.
1045 KUTLUAY, S. B., ZANG, T., BLANCO-MELO, D., POWELL, C., JANNAIN, D.,
1046 ERRANDO, M. & BIENIASZ, P. D. 2014. Global changes in the RNA binding
1047 specificity of HIV-1 gag regulate virion genesis. *Cell,* 159**,** 1096-1109.
1048 KWAN, T. & THOMPSON, S. R. 2019. Noncanonical Translation Initiation in Eukaryotes.
1049 *Cold Spring Harb Perspect Biol,* 11.

1050 LANGMEAD, B., TRAPNELL, C., POP, M. & SALZBERG, S. L. 2009. Ultrafast and
1051 memory-efficient alignment of short DNA sequences to the human genome.
1052 *Genome Biol,* 10**,** R25.
1053 LAURIA, F., TEBALDI, T., BERNABO, P., GROEN, E. J. N., GILLINGWATER, T. H. &
1054 VIERO, G. 2018. riboWaltz: Optimization of ribosome P-site positioning in
1055 ribosome profiling data. *PLoS Comput Biol,* 14**,** e1006169.
1056 LI, H. & DURBIN, R. 2009. Fast and accurate short read alignment with Burrows-
1057 Wheeler transform. *Bioinformatics,* 25**,** 1754-60.
1058 LI, H., HANDSAKER, B., WYSOKER, A., FENNELL, T., RUAN, J., HOMER, N.,
1059 MARTH, G., ABECASIS, G., DURBIN, R. & GENOME PROJECT DATA
1060 PROCESSING, S. 2009. The Sequence Alignment/Map format and SAMtools.
1061 *Bioinformatics,* 25**,** 2078-9.
1062 LI, M. M., MACDONALD, M. R. & RICE, C. M. 2015. To translate, or not to translate:
1063 viral and host mRNA regulation by interferon-stimulated genes. *Trends Cell Biol,*
1064 25**,** 320-9.
1065 LI, Z., LI, Y., LIU, S. & QIN, Z. 2020. Extracellular S100A4 as a key player in fibrotic
1066 diseases. *J Cell Mol Med,* 24**,** 5973-5983.
1067 LIU, Y., MYRVANG, H. K. & DEKKER, L. V. 2015. Annexin A2 complexes with S100
1068 proteins: structure, function and pharmacological manipulation. *Br J Pharmacol,*
1069 172**,** 1664-76.
1070 LOKUGAMAGE, K. G., NARAYANAN, K., HUANG, C. & MAKINO, S. 2012. Severe
1071 acute respiratory syndrome coronavirus protein nsp1 is a novel eukaryotic
1072 translation inhibitor that represses multiple steps of translation initiation. *J Virol,*
1073 86**,** 13598-608.
1074 MARENHOLZ, I., HEIZMANN, C. W. & FRITZ, G. 2004. S100 proteins in mouse and
1075 man: from evolution to function and pathology (including an update of the
1076 nomenclature). *Biochem Biophys Res Commun,* 322**,** 1111-22.
1077 MASTERS, P. S. 2006. The molecular biology of coronaviruses. *Adv Virus Res,* 66**,** 193-
1078 292.
1079 MENACHERY, V. D., EISFELD, A. J., SCHAFER, A., JOSSET, L., SIMS, A. C., PROLL,
1080 S., FAN, S., LI, C., NEUMANN, G., TILTON, S. C., CHANG, J., GRALINSKI, L.
1081 E., LONG, C., GREEN, R., WILLIAMS, C. M., WEISS, J., MATZKE, M. M.,
1082 WEBB-ROBERTSON, B. J., SCHEPMOES, A. A., SHUKLA, A. K., METZ, T. O.,
1083 SMITH, R. D., WATERS, K. M., KATZE, M. G., KAWAOKA, Y. & BARIC, R. S.
1084 2014. Pathogenic influenza viruses and coronaviruses utilize similar and
1085 contrasting approaches to control interferon-stimulated gene responses. *mBio,* 5**,**
1086 e01174-14.
1087 MITCHELL, H. D., EISFELD, A. J., SIMS, A. C., MCDERMOTT, J. E., MATZKE, M. M.,
1088 WEBB-ROBERTSON, B. J., TILTON, S. C., TCHITCHEK, N., JOSSET, L., LI, C.,
1089 ELLIS, A. L., CHANG, J. H., HEEGEL, R. A., LUNA, M. L., SCHEPMOES, A. A.,
1090 SHUKLA, A. K., METZ, T. O., NEUMANN, G., BENECKE, A. G., SMITH, R. D.,
1091 BARIC, R. S., KAWAOKA, Y., KATZE, M. G. & WATERS, K. M. 2013. A network
1092 integration approach to predict conserved regulators related to pathogenicity of
1093 influenza and SARS-CoV respiratory viruses. *PLoS One,* 8**,** e69374.
1094 MOOTHA, V. K., LINDGREN, C. M., ERIKSSON, K. F., SUBRAMANIAN, A., SIHAG, S.,
1095 LEHAR, J., PUIGSERVER, P., CARLSSON, E., RIDDERSTRALE, M., LAURILA,
1096 E., HOUSTIS, N., DALY, M. J., PATTERSON, N., MESIROV, J. P., GOLUB, T.
1097 R., TAMAYO, P., SPIEGELMAN, B., LANDER, E. S., HIRSCHHORN, J. N.,
1098 ALTSHULER, D. & GROOP, L. C. 2003. PGC-1alpha-responsive genes involved
1099 in oxidative phosphorylation are coordinately downregulated in human diabetes.
1100 *Nat Genet,* 34**,** 267-73.

1101 MOUZAKIS, K. D., LANG, A. L., VANDER MEULEN, K. A., EASTERDAY, P. D. &
1102 BUTCHER, S. E. 2013. HIV-1 frameshift efficiency is primarily determined by the
1103 stability of base pairs positioned at the mRNA entrance channel of the ribosome.
1104 *Nucleic Acids Res,* 41**,** 1901-13.
1105 NAKAGAWA, K., LOKUGAMAGE, K. G. & MAKINO, S. 2016. Viral and Cellular mRNA
1106 Translation in Coronavirus-Infected Cells. *Adv Virus Res,* 96**,** 165-192.
1107 NARAYANAN, K., HUANG, C., LOKUGAMAGE, K., KAMITANI, W., IKEGAMI, T.,
1108 TSENG, C. T. & MAKINO, S. 2008. Severe acute respiratory syndrome
1109 coronavirus nsp1 suppresses host gene expression, including that of type I
1110 interferon, in infected cells. *J Virol,* 82**,** 4471-9.
1111 NARAYANAN, K., RAMIREZ, S. I., LOKUGAMAGE, K. G. & MAKINO, S. 2015.
1112 Coronavirus nonstructural protein 1: Common and distinct functions in the
1113 regulation of host and viral gene expression. *Virus Res,* 202**,** 89-100.
1114 PARKIN, N. T., CHAMORRO, M. & VARMUS, H. E. 1992. Human immunodeficiency
1115 virus type 1 gag-pol frameshifting is dependent on downstream mRNA secondary
1116 structure: demonstration by expression in vivo. *J Virol,* 66**,** 5147-51.
1117 PERLMAN, S. & DANDEKAR, A. A. 2005. Immunopathogenesis of coronavirus
1118 infections: implications for SARS. *Nat Rev Immunol,* 5**,** 917-27.
1119 PLANT, E. P. & DINMAN, J. D. 2008. The role of programmed-1 ribosomal frameshifting
1120 in coronavirus propagation. *Front Biosci,* 13**,** 4873-81.
1121 PLANT, E. P., JACOBS, K. L., HARGER, J. W., MESKAUSKAS, A., JACOBS, J. L.,
1122 BAXTER, J. L., PETROV, A. N. & DINMAN, J. D. 2003. The 9-A solution: how
1123 mRNA pseudoknots promote efficient programmed -1 ribosomal frameshifting.
1124 *RNA,* 9**,** 168-74.
1125 REYNAUD, J. M., KIM, D. Y., ATASHEVA, S., RASALOUSKAYA, A., WHITE, J. P.,
1126 DIAMOND, M. S., WEAVER, S. C., FROLOVA, E. I. & FROLOV, I. 2015. IFIT1
1127 Differentially Interferes with Translation and Replication of Alphavirus Genomes
1128 and Promotes Induction of Type I Interferon. *PLoS Pathog,* 11**,** e1004863.
1129 RIBA, A., DI NANNI, N., MITTAL, N., ARHNE, E., SCHMIDT, A. & ZAVOLAN, M. 2019.
1130 Protein synthesis rates and ribosome occupancies reveal determinants of
1131 translation elongation rates. *Proc Natl Acad Sci U S A,* 116**,** 15023-15032.
1132 ROBINSON, M. D., MCCARTHY, D. J. & SMYTH, G. K. 2010. edgeR: a Bioconductor
1133 package for differential expression analysis of digital gene expression data.
1134 *Bioinformatics,* 26**,** 139-40.
1135 SHEHU-XHILAGA, M., CROWE, S. M. & MAK, J. 2001. Maintenance of the Gag/Gag-
1136 Pol ratio is important for human immunodeficiency virus type 1 RNA dimerization
1137 and viral infectivity. *J Virol,* 75**,** 1834-41.
1138 STAPLE, D. W. & BUTCHER, S. E. 2005. Solution structure and thermodynamic
1139 investigation of the HIV-1 frameshift inducing element. *J Mol Biol,* 349**,** 1011-23.
1140 SUBRAMANIAN, A., TAMAYO, P., MOOTHA, V. K., MUKHERJEE, S., EBERT, B. L.,
1141 GILLETTE, M. A., PAULOVICH, A., POMEROY, S. L., GOLUB, T. R., LANDER,
1142 E. S. & MESIROV, J. P. 2005. Gene set enrichment analysis: a knowledge-
1143 based approach for interpreting genome-wide expression profiles. *Proc Natl*
1144 *Acad Sci U S A,* 102**,** 15545-50.
1145 TAYLOR, J. R., SKEATE, J. G. & KAST, W. M. 2018. Annexin A2 in Virus Infection.
1146 *Front Microbiol,* 9**,** 2954.
1147 TENENBAUM, D. 2020. KEGGREST: Client-side REST access to KEGG. R package
1148 version 1.6.4.
1149 WANG, X., XUAN, Y., HAN, Y., DING, X., YE, K., YANG, F., GAO, P., GOFF, S. P. &
1150 GAO, G. 2019. Regulation of HIV-1 Gag-Pol Expression by Shiftless, an Inhibitor
1151 of Programmed -1 Ribosomal Frameshifting. *Cell,* 176**,** 625-635 e14.

1152 WEISS, S. R. & NAVAS-MARTIN, S. 2005. Coronavirus pathogenesis and the emerging
1153 pathogen severe acute respiratory syndrome coronavirus. *Microbiol Mol Biol*
1154 *Rev,* 69**,** 635-64.
1155 WILK, A. J., RUSTAGI, A., ZHAO, N. Q., ROQUE, J., MARTINEZ-COLON, G. J.,
1156 MCKECHNIE, J. L., IVISON, G. T., RANGANATH, T., VERGARA, R., HOLLIS,
1157 T., SIMPSON, L. J., GRANT, P., SUBRAMANIAN, A., ROGERS, A. J. & BLISH,
1158 C. A. 2020. A single-cell atlas of the peripheral immune response in patients with
1159 severe COVID-19. *Nat Med,* 26**,** 1070-1076.
1160 WILSON, W., BRADDOCK, M., ADAMS, S. E., RATHJEN, P. D., KINGSMAN, S. M. &
1161 KINGSMAN, A. J. 1988. HIV expression strategies: ribosomal frameshifting is
1162 directed by a short sequence in both mammalian and yeast systems. *Cell,* 55**,**
1163 1159-69.
1164 XIAO, H., XU, L. H., YAMADA, Y. & LIU, D. X. 2008. Coronavirus spike protein inhibits
1165 host cell translation by interaction with eIF3f. *PLoS One,* 3**,** e1494.
1166 YOU, Y., RICHER, E. J., HUANG, T. & BRODY, S. L. 2002. Growth and differentiation of
1167 mouse tracheal epithelial cells: selection of a proliferative population. *Am J*
1168 *Physiol Lung Cell Mol Physiol,* 283**,** L1315-21.
1169 YOUNG, M. D., WAKEFIELD, M. J., SMYTH, G. K. & OSHLACK, A. 2010. Gene
1170 ontology analysis for RNA-seq: accounting for selection bias. *Genome Biol,* 11**,**
1171 R14.
1172 ZHANG, P., HE, D., XU, Y., HOU, J., PAN, B. F., WANG, Y., LIU, T., DAVIS, C. M.,
1173 EHLI, E. A., TAN, L., ZHOU, F., HU, J., YU, Y., CHEN, X., NGUYEN, T. M.,
1174 ROSEN, J. M., HAWKE, D. H., JI, Z. & CHEN, Y. 2017. Genome-wide
1175 identification and differential analysis of translational initiation. *Nat Commun,* 8**,**
1176 1749.
1177 ZHOU, B., LIU, J., WANG, Q., LIU, X., LI, X., LI, P., MA, Q. & CAO, C. 2008. The
1178 nucleocapsid protein of severe acute respiratory syndrome coronavirus inhibits
1179 cell cytokinesis and proliferation by interacting with translation elongation factor
1180 1alpha. *J Virol,* 82**,** 6962-71.
1181 ZHOU, Z., REN, L., ZHANG, L., ZHONG, J., XIAO, Y., JIA, Z., GUO, L., YANG, J.,
1182 WANG, C., JIANG, S., YANG, D., ZHANG, G., LI, H., CHEN, F., XU, Y., CHEN,
1183 M., GAO, Z., YANG, J., DONG, J., LIU, B., ZHANG, X., WANG, W., HE, K., JIN,
1184 Q., LI, M. & WANG, J. 2020. Heightened Innate Immune Responses in the
1185 Respiratory Tract of COVID-19 Patients. *Cell Host Microbe,* 27**,** 883-890 e2.
1186

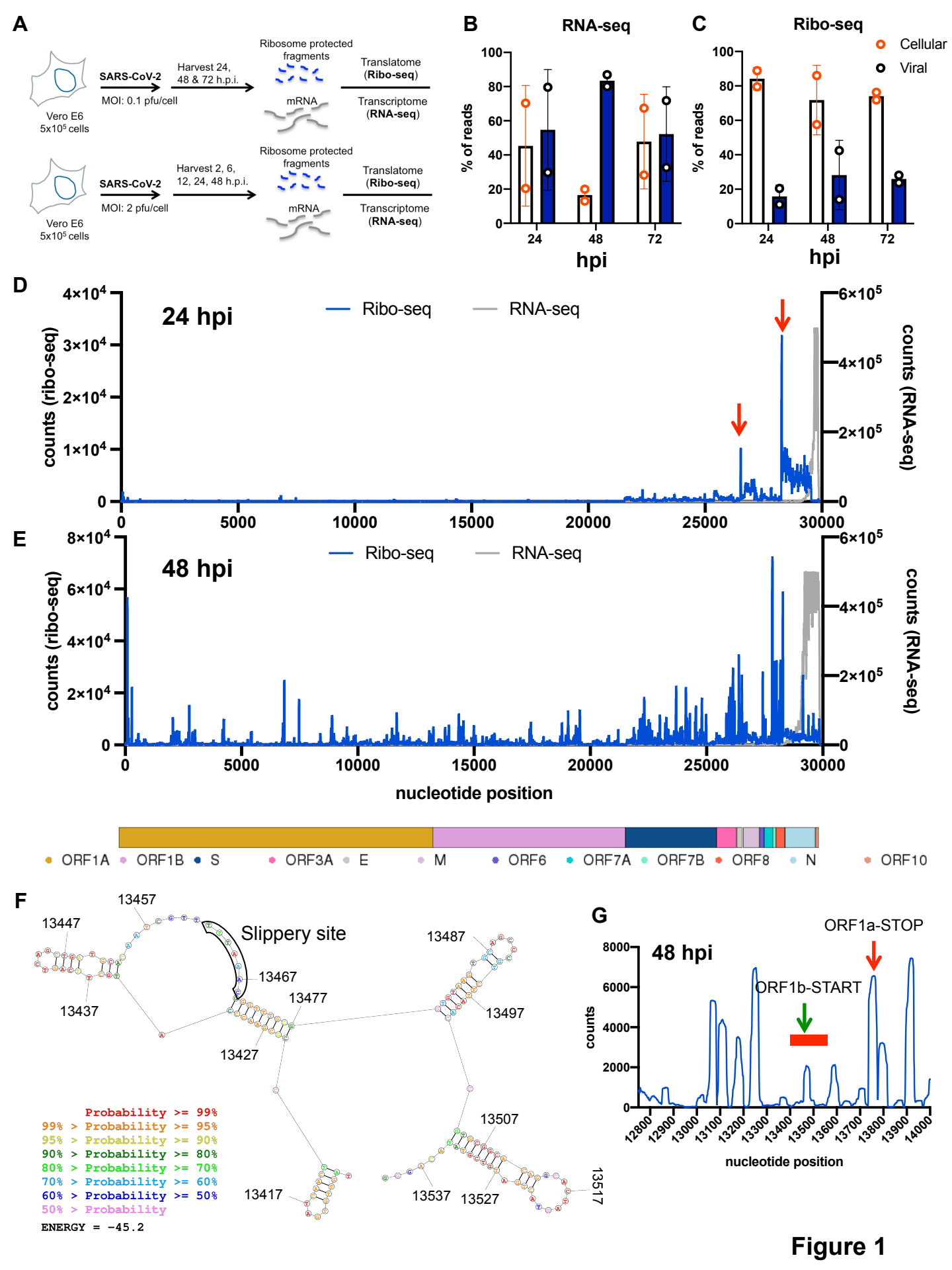
A
SARS-CoV-2
MOI: 0.1 pfu/cell
Harvest 24, 48 & 72 h.p.i.
Vero E6 5x10^5 cells
Ribosome protected fragments
mRNA
Translatome (Ribo-seq)
Transcriptome (RNA-seq)
SARS-CoV-2
MOI: 2 pfu/cell
Harvest 2, 6, 12, 24, 48 h.p.i.
Vero E6 5x10^5 cells
Ribosome protected fragments
mRNA
Translatome (Ribo-seq)
Transcriptome (RNA-seq)
B
RNA-seq
% of reads
hpi
C
Ribo-seq
Cellular
Viral
% of reads
hpi
D
24 hpi
Ribo-seq
RNA-seq
counts (ribo-seq)
counts (RNA-seq)
E
48 hpi
Ribo-seq
RNA-seq
counts (ribo-seq)
counts (RNA-seq)
nucleotide position
ORF1A
ORF1B
S
ORF3A
E
M
ORF6
ORF7A
ORF7B
ORF8
N
ORF10
F
Slippery site
13457
13447
13437
13467
13477
13427
13487
13497
13507
13517
13537
13527
13417
Probability >= 99%
99% > Probability >= 95%
95% > Probability >= 90%
90% > Probability >= 80%
80% > Probability >= 70%
70% > Probability >= 60%
60% > Probability >= 50%
50% > Probability
ENERGY = -45.2
G
48 hpi
ORF1a-STOP
ORF1b-START
counts
nucleotide position

Figure 1

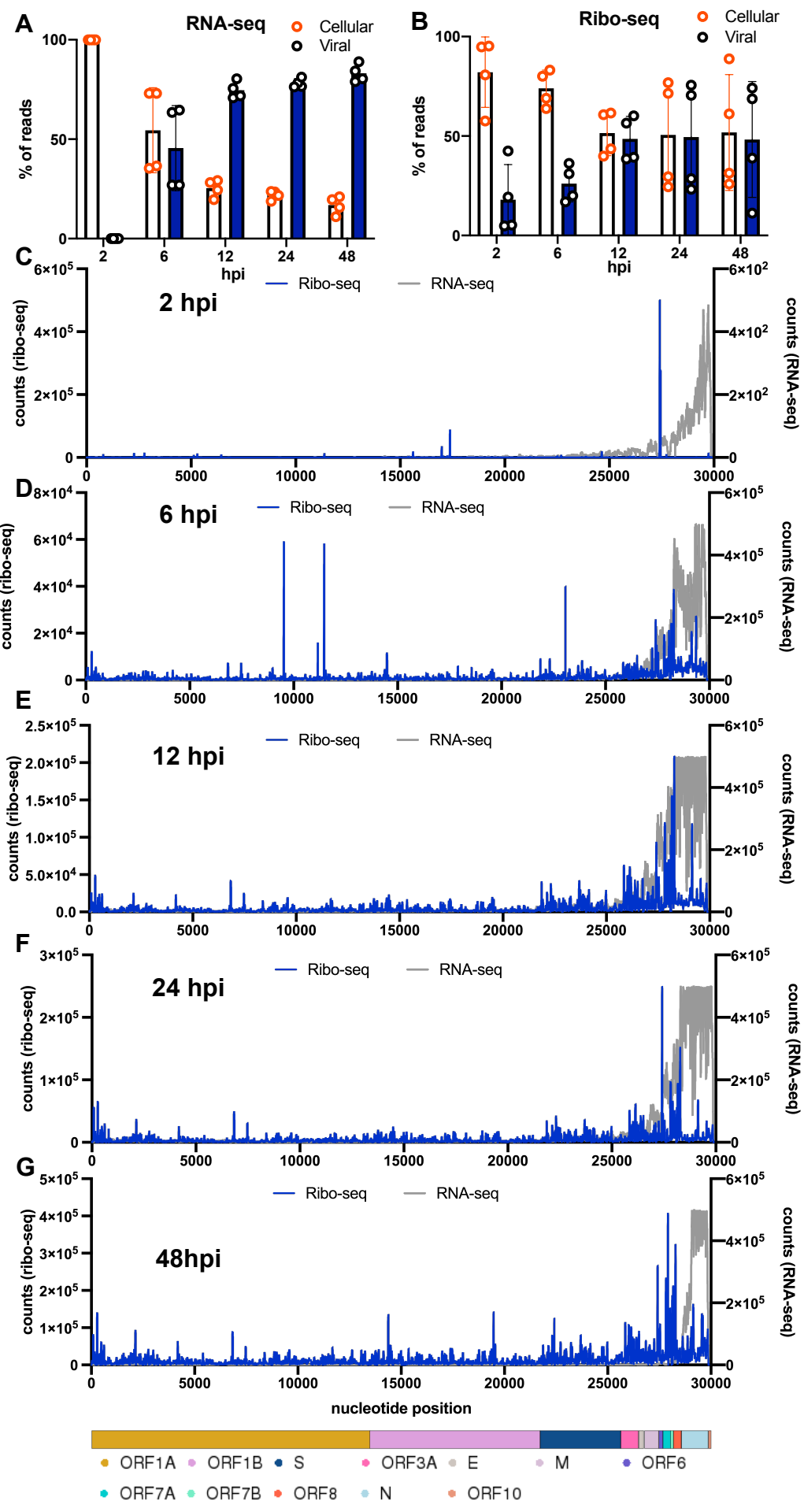
A
RNA-seq
Cellular
Viral
% of reads
hpi
B
Ribo-seq
Cellular
Viral
% of reads
hpi
C
2 hpi
Ribo-seq
RNA-seq
counts (ribo-seq)
counts (RNA-seq)
D
6 hpi
Ribo-seq
RNA-seq
counts (ribo-seq)
counts (RNA-seq)
E
12 hpi
Ribo-seq
RNA-seq
counts (ribo-seq)
counts (RNA-seq)
F
24 hpi
Ribo-seq
RNA-seq
counts (ribo-seq)
counts (RNA-seq)
G
48hpi
Ribo-seq
RNA-seq
counts (ribo-seq)
counts (RNA-seq)
nucleotide position
ORF1A
ORF1B
S
ORF3A
E
M
ORF6
ORF7A
ORF7B
ORF8
N
ORF10

Figure 2

HBECs

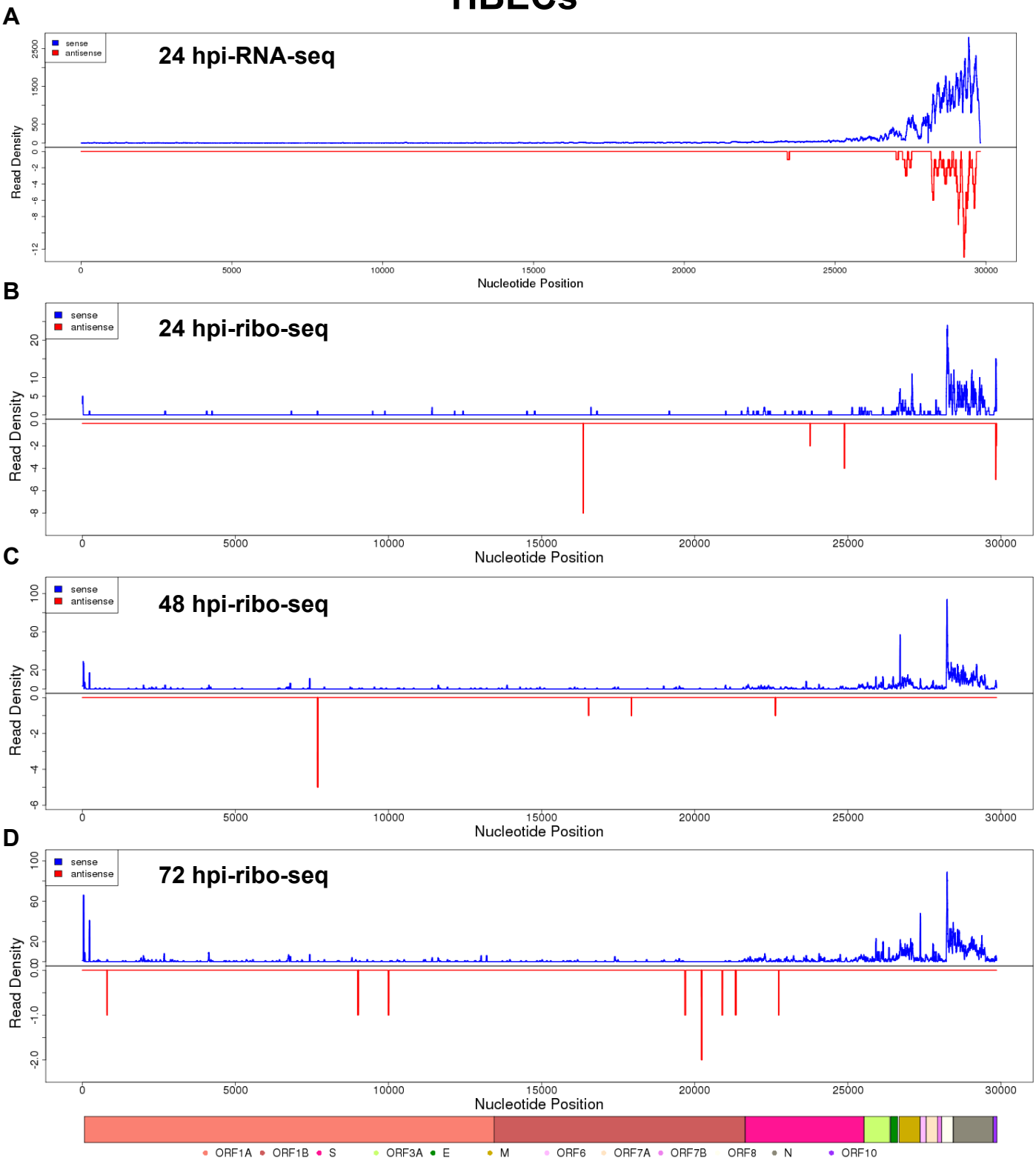

Figure 3

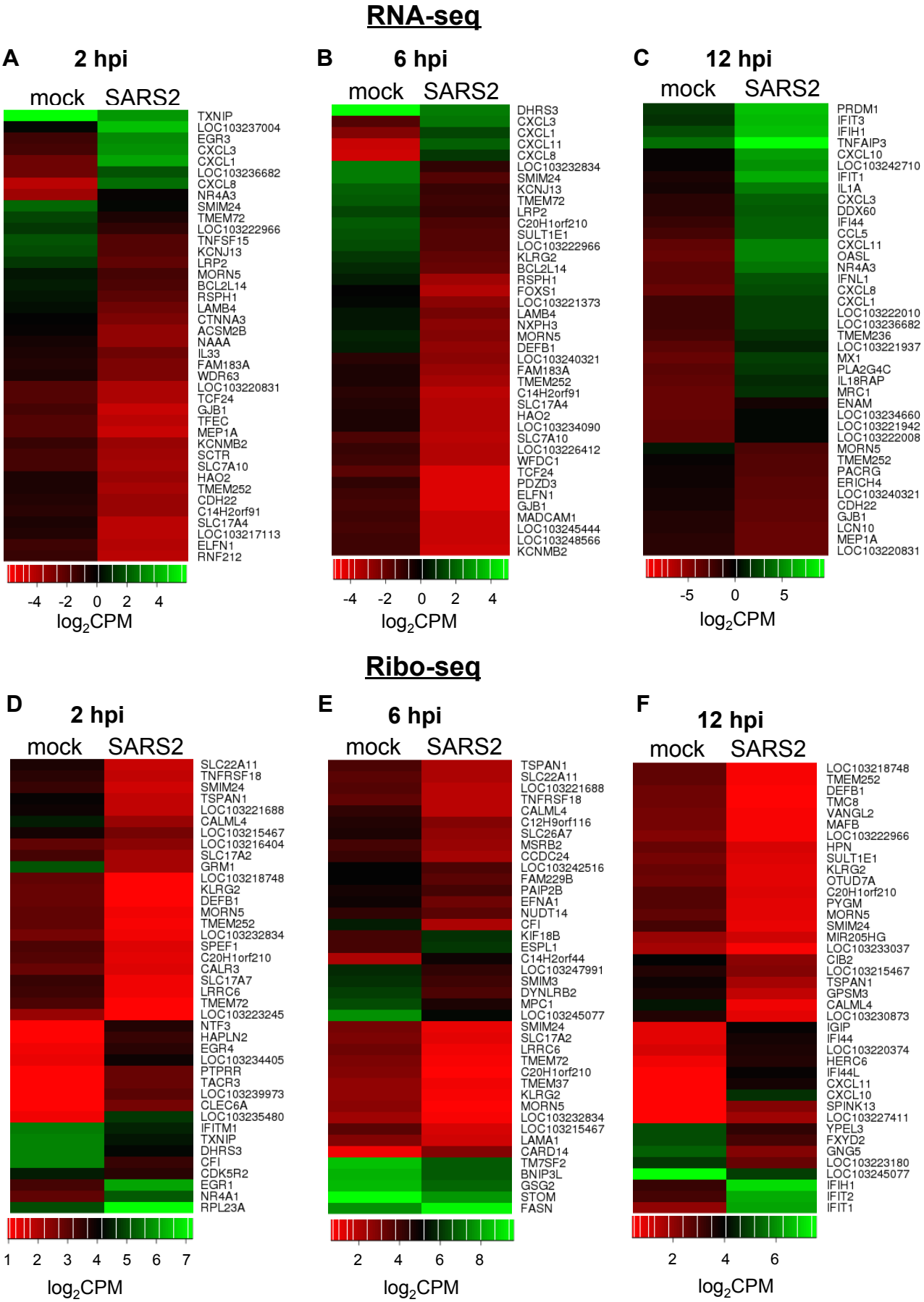
RNA-seq
A
2 hpi
mock
SARS2
TXNIP
LOC103237004
EGR3
CXCL3
CXCL1
LOC103236682
CXCL8
NR4A3
SMIM24
TMEM72
LOC103222966
TNFSF15
KCNJ13
LRP2
MORN5
BCL2L14
RSPH1
LAMB4
CTNNA3
ACSM2B
NAAA
IL33
FAM183A
WDR63
LOC103220831
TCF24
GJB1
TFEC
MEP1A
KCNMB2
SCTR
SLC7A10
HAO2
TMEM252
CDH22
C14H2orf91
SLC17A4
LOC103217113
ELFN1
RNF212
-4 -2 0 2 4
log2CPM
B
6 hpi
mock
SARS2
DHRS3
CXCL3
CXCL1
CXCL11
CXCL8
LOC103232834
SMIM24
KCNJ13
TMEM72
LRP2
C20H1orf210
SULT1E1
LOC103222966
KLRG2
BCL2L14
RSPH1
FOXS1
LOC103221373
LAMB4
NXPH3
MORN5
DEFB1
LOC103240321
FAM183A
TMEM252
C14H2orf91
SLC17A4
HAO2
LOC103234090
SLC7A10
LOC103226412
WFDC1
TCF24
PDZD3
ELFN1
GJB1
MADCAM1
LOC103245444
LOC103248566
KCNMB2
-4 -2 0 2 4
log2CPM
C
12 hpi
mock
SARS2
PRDM1
IFIT3
IFIH1
TNFAIP3
CXCL10
LOC103242710
IFIT1
IL1A
CXCL3
DDX60
IFI44
CCL5
CXCL11
OASL
NR4A3
IFNL1
CXCL8
CXCL1
LOC103222010
LOC103236682
TMEM236
LOC103221937
MX1
PLA2G4C
IL18RAP
MRC1
ENAM
LOC103234660
LOC103221942
LOC103222008
MORN5
TMEM252
PACRG
ERICH4
LOC103240321
CDH22
GJB1
LCN10
MEP1A
LOC103220831
-5 0 5
log2CPM
Ribo-seq
D
2 hpi
mock
SARS2
SLC22A11
TNFRSF18
SMIM24
TSPAN1
LOC103221688
CALML4
LOC103215467
LOC103216404
SLC17A2
GRM1
LOC103218748
KLRG2
DEFB1
MORN5
TMEM252
LOC103232834
SPEF1
C20H1orf210
CALR3
SLC17A7
LRRC6
TMEM72
LOC103223245
NTF3
HAPLN2
EGR4
LOC103234405
PTPRR
TACR3
LOC103239973
CLEC6A
LOC103235480
IFITM1
TXNIP
DHRS3
CFI
CDK5R2
EGR1
NR4A1
RPL23A
1 2 3 4 5 6 7
log2CPM
E
6 hpi
mock
SARS2
TSPAN1
SLC22A11
LOC103221688
TNFRSF18
CALML4
C12H9orf116
SLC26A7
MSRB2
CCDC24
LOC103242516
FAM229B
PAIP2B
EFNA1
NUDT14
CFI
KIF18B
ESPL1
C14H2orf44
LOC103247991
SMIM3
DYNLRB2
MPC1
LOC103245077
SMIM24
SLC17A2
LRRC6
TMEM72
C20H1orf210
TMEM37
KLRG2
MORN5
LOC103232834
LOC103215467
LAMA1
CARD14
TM7SF2
BNIP3L
GSG2
STOM
FASN
2 4 6 8
log2CPM
F
12 hpi
mock
SARS2
LOC103218748
TMEM252
DEFB1
TMC8
VANGL2
MAFB
LOC103222966
HPN
SULT1E1
KLRG2
OTUD7A
C20H1orf210
PYGM
MORN5
SMIM24
MIR205HG
LOC103233037
CIB2
LOC103215467
TSPAN1
GPSM3
CALML4
LOC103230873
IGIP
IFI44
LOC103220374
HERC6
IFI44L
CXCL11
CXCL10
SPINK13
LOC103227411
YPEL3
FXYD2
GNG5
LOC103223180
LOC103245077
IFIH1
IFIT2
IFIT1
2 4 6
log2CPM

Figure 4

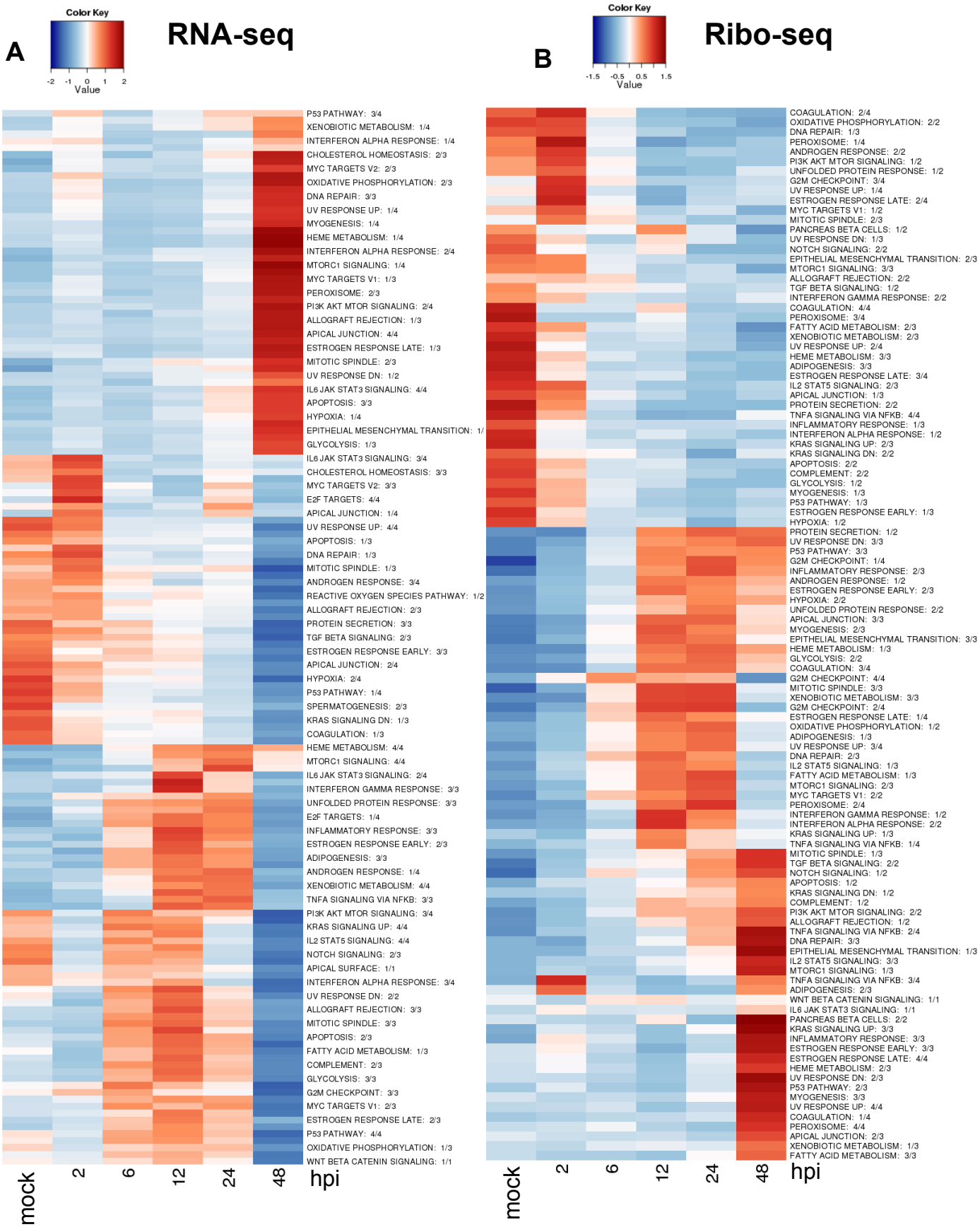
A
Color Key
-2 -1 0 1 2
Value
RNA-seq
P53 PATHWAY: 3/4
XENOBIOTIC METABOLISM: 1/4
INTERFERON ALPHA RESPONSE: 1/4
CHOLESTEROL HOMEOSTASIS: 2/3
MYC TARGETS V2: 2/3
OXIDATIVE PHOSPHORYLATION: 2/3
DNA REPAIR: 3/3
UV RESPONSE UP: 1/4
MYOGENESIS: 1/4
HEME METABOLISM: 1/4
INTERFERON ALPHA RESPONSE: 2/4
MTORC1 SIGNALING: 1/4
MYC TARGETS V1: 1/3
PEROXISOME: 2/3
PI3K AKT MTOR SIGNALING: 2/4
ALLOGRAFT REJECTION: 1/3
APICAL JUNCTION: 4/4
ESTROGEN RESPONSE LATE: 1/3
MITOTIC SPINDLE: 2/3
UV RESPONSE DN: 1/2
IL6 JAK STAT3 SIGNALING: 4/4
APOPTOSIS: 3/3
HYPOXIA: 1/4
EPITHELIAL MESENCHYMAL TRANSITION: 1/
GLYCOLYSIS: 1/3
IL6 JAK STAT3 SIGNALING: 3/4
CHOLESTEROL HOMEOSTASIS: 3/3
MYC TARGETS V2: 3/3
E2F TARGETS: 4/4
APICAL JUNCTION: 1/4
UV RESPONSE UP: 4/4
APOPTOSIS: 1/3
DNA REPAIR: 1/3
MITOTIC SPINDLE: 1/3
ANDROGEN RESPONSE: 3/4
REACTIVE OXYGEN SPECIES PATHWAY: 1/2
ALLOGRAFT REJECTION: 2/3
PROTEIN SECRETION: 3/3
TGF BETA SIGNALING: 2/3
ESTROGEN RESPONSE EARLY: 3/3
APICAL JUNCTION: 2/4
HYPOXIA: 2/4
P53 PATHWAY: 1/4
SPERMATOGENESIS: 2/3
KRAS SIGNALING DN: 1/3
COAGULATION: 1/3
HEME METABOLISM: 4/4
MTORC1 SIGNALING: 4/4
IL6 JAK STAT3 SIGNALING: 2/4
INTERFERON GAMMA RESPONSE: 3/3
UNFOLDED PROTEIN RESPONSE: 3/3
E2F TARGETS: 1/4
INFLAMMATORY RESPONSE: 3/3
ESTROGEN RESPONSE EARLY: 2/3
ADIPOGENESIS: 3/3
ANDROGEN RESPONSE: 1/4
XENOBIOTIC METABOLISM: 4/4
TNFA SIGNALING VIA NFKB: 3/3
PI3K AKT MTOR SIGNALING: 3/4
KRAS SIGNALING UP: 4/4
IL2 STAT5 SIGNALING: 4/4
NOTCH SIGNALING: 2/3
APICAL SURFACE: 1/1
INTERFERON ALPHA RESPONSE: 3/4
UV RESPONSE DN: 2/2
ALLOGRAFT REJECTION: 3/3
MITOTIC SPINDLE: 3/3
APOPTOSIS: 2/3
FATTY ACID METABOLISM: 1/3
COMPLEMENT: 2/3
GLYCOLYSIS: 3/3
G2M CHECKPOINT: 3/3
MYC TARGETS V1: 2/3
ESTROGEN RESPONSE LATE: 2/3
P53 PATHWAY: 4/4
OXIDATIVE PHOSPHORYLATION: 1/3
WNT BETA CATENIN SIGNALING: 1/1
mock
2
6
12
24
48
hpi
B
Color Key
-1.5 -0.5 0.5 1.5
Value
Ribo-seq
COAGULATION: 2/4
OXIDATIVE PHOSPHORYLATION: 2/2
DNA REPAIR: 1/3
PEROXISOME: 1/4
ANDROGEN RESPONSE: 2/2
PI3K AKT MTOR SIGNALING: 1/2
UNFOLDED PROTEIN RESPONSE: 1/2
G2M CHECKPOINT: 3/4
UV RESPONSE UP: 1/4
ESTROGEN RESPONSE LATE: 2/4
MYC TARGETS V1: 1/2
MITOTIC SPINDLE: 2/3
PANCREAS BETA CELLS: 1/2
UV RESPONSE DN: 1/3
NOTCH SIGNALING: 2/2
EPITHELIAL MESENCHYMAL TRANSITION: 2/3
MTORC1 SIGNALING: 3/3
ALLOGRAFT REJECTION: 2/2
TGF BETA SIGNALING: 1/2
INTERFERON GAMMA RESPONSE: 2/2
COAGULATION: 4/4
PEROXISOME: 3/4
FATTY ACID METABOLISM: 2/3
XENOBIOTIC METABOLISM: 2/3
UV RESPONSE UP: 2/4
HEME METABOLISM: 3/3
ADIPOGENESIS: 3/3
ESTROGEN RESPONSE LATE: 3/4
IL2 STAT5 SIGNALING: 2/3
APICAL JUNCTION: 1/3
PROTEIN SECRETION: 2/2
TNFA SIGNALING VIA NFKB: 4/4
INFLAMMATORY RESPONSE: 1/3
INTERFERON ALPHA RESPONSE: 1/2
KRAS SIGNALING UP: 2/3
KRAS SIGNALING DN: 2/2
APOPTOSIS: 2/2
COMPLEMENT: 2/2
GLYCOLYSIS: 1/2
MYOGENESIS: 1/3
P53 PATHWAY: 1/3
ESTROGEN RESPONSE EARLY: 1/3
HYPOXIA: 1/2
PROTEIN SECRETION: 1/2
UV RESPONSE DN: 3/3
P53 PATHWAY: 3/3
G2M CHECKPOINT: 1/4
INFLAMMATORY RESPONSE: 2/3
ANDROGEN RESPONSE: 1/2
ESTROGEN RESPONSE EARLY: 2/3
HYPOXIA: 2/2
UNFOLDED PROTEIN RESPONSE: 2/2
APICAL JUNCTION: 3/3
MYOGENESIS: 2/3
EPITHELIAL MESENCHYMAL TRANSITION: 3/3
HEME METABOLISM: 1/3
GLYCOLYSIS: 2/2
COAGULATION: 3/4
G2M CHECKPOINT: 4/4
MITOTIC SPINDLE: 3/3
XENOBIOTIC METABOLISM: 3/3
G2M CHECKPOINT: 2/4
ESTROGEN RESPONSE LATE: 1/4
OXIDATIVE PHOSPHORYLATION: 1/2
ADIPOGENESIS: 1/3
UV RESPONSE UP: 3/4
DNA REPAIR: 2/3
IL2 STAT5 SIGNALING: 1/3
FATTY ACID METABOLISM: 1/3
MTORC1 SIGNALING: 2/3
MYC TARGETS V1: 2/2
PEROXISOME: 2/4
INTERFERON GAMMA RESPONSE: 1/2
INTERFERON ALPHA RESPONSE: 2/2
KRAS SIGNALING UP: 1/3
TNFA SIGNALING VIA NFKB: 1/4
MITOTIC SPINDLE: 1/3
TGF BETA SIGNALING: 2/2
NOTCH SIGNALING: 1/2
APOPTOSIS: 1/2
KRAS SIGNALING DN: 1/2
COMPLEMENT: 1/2
PI3K AKT MTOR SIGNALING: 2/2
ALLOGRAFT REJECTION: 1/2
TNFA SIGNALING VIA NFKB: 2/4
DNA REPAIR: 3/3
EPITHELIAL MESENCHYMAL TRANSITION: 1/3
IL2 STAT5 SIGNALING: 3/3
MTORC1 SIGNALING: 1/3
TNFA SIGNALING VIA NFKB: 3/4
ADIPOGENESIS: 2/3
WNT BETA CATENIN SIGNALING: 1/1
IL6 JAK STAT3 SIGNALING: 1/1
PANCREAS BETA CELLS: 2/2
KRAS SIGNALING UP: 3/3
INFLAMMATORY RESPONSE: 3/3
ESTROGEN RESPONSE EARLY: 3/3
ESTROGEN RESPONSE LATE: 4/4
HEME METABOLISM: 2/3
UV RESPONSE DN: 2/3
P53 PATHWAY: 2/3
MYOGENESIS: 3/3
UV RESPONSE UP: 4/4
COAGULATION: 1/4
PEROXISOME: 4/4
APICAL JUNCTION: 2/3
XENOBIOTIC METABOLISM: 1/3
FATTY ACID METABOLISM: 3/3
mock
2
6
12
24
48
hpi

Figure 5

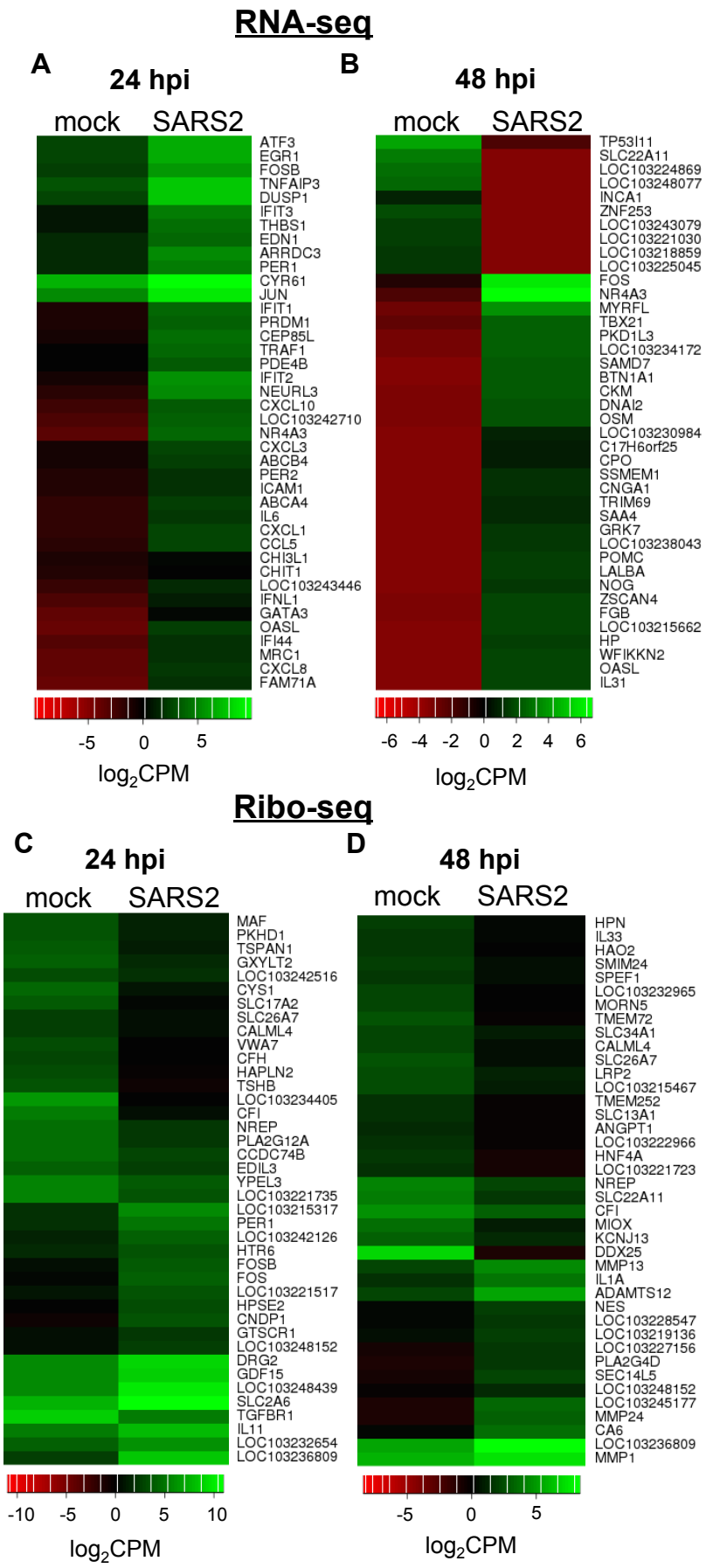
RNA-seq
A
24 hpi
mock
SARS2
ATF3
EGR1
FOSB
TNFAIP3
DUSP1
IFIT3
THBS1
EDN1
ARRDC3
PER1
CYR61
JUN
IFIT1
PRDM1
CEP85L
TRAF1
PDE4B
IFIT2
NEURL3
CXCL10
LOC103242710
NR4A3
CXCL3
ABCB4
PER2
ICAM1
ABCA4
IL6
CXCL1
CCL5
CHI3L1
CHIT1
LOC103243446
IFNL1
GATA3
OASL
IFI44
MRC1
CXCL8
FAM71A
-5 0 5
log2CPM
B
48 hpi
mock
SARS2
TP53I11
SLC22A11
LOC103224869
LOC103248077
INCA1
ZNF253
LOC103243079
LOC103221030
LOC103218859
LOC103225045
FOS
NR4A3
MYRFL
TBX21
PKD1L3
LOC103234172
SAMD7
BTN1A1
CKM
DNAI2
OSM
LOC103230984
C17H6orf25
CPO
SSMEM1
CNGA1
TRIM69
SAA4
GRK7
LOC103238043
POMC
LALBA
NOG
ZSCAN4
FGB
LOC103215662
HP
WFIKKN2
OASL
IL31
-6 -4 -2 0 2 4 6
log2CPM
Ribo-seq
C
24 hpi
mock
SARS2
MAF
PKHD1
TSPAN1
GXYLT2
LOC103242516
CYS1
SLC17A2
SLC26A7
CALML4
VWA7
CFH
HAPLN2
TSHB
LOC103234405
CFI
NREP
PLA2G12A
CCDC74B
EDIL3
YPEL3
LOC103221735
LOC103215317
PER1
LOC103242126
HTR6
FOSB
FOS
LOC103221517
HPSE2
CNDP1
GTSCR1
LOC103248152
DRG2
GDF15
LOC103248439
SLC2A6
TGFBR1
IL11
LOC103232654
LOC103236809
-10 -5 0 5 10
log2CPM
D
48 hpi
mock
SARS2
HPN
IL33
HAO2
SMIM24
SPEF1
LOC103232965
MORN5
TMEM72
SLC34A1
CALML4
SLC26A7
LRP2
LOC103215467
TMEM252
SLC13A1
ANGPT1
LOC103222966
HNF4A
LOC103221723
NREP
SLC22A11
CFI
MIOX
KCNJ13
DDX25
MMP13
IL1A
ADAMTS12
NES
LOC103228547
LOC103219136
LOC103227156
PLA2G4D
SEC14L5
LOC103248152
LOC103245177
MMP24
CA6
LOC103236809
MMP1
-5 0 5
log2CPM

Figure 6

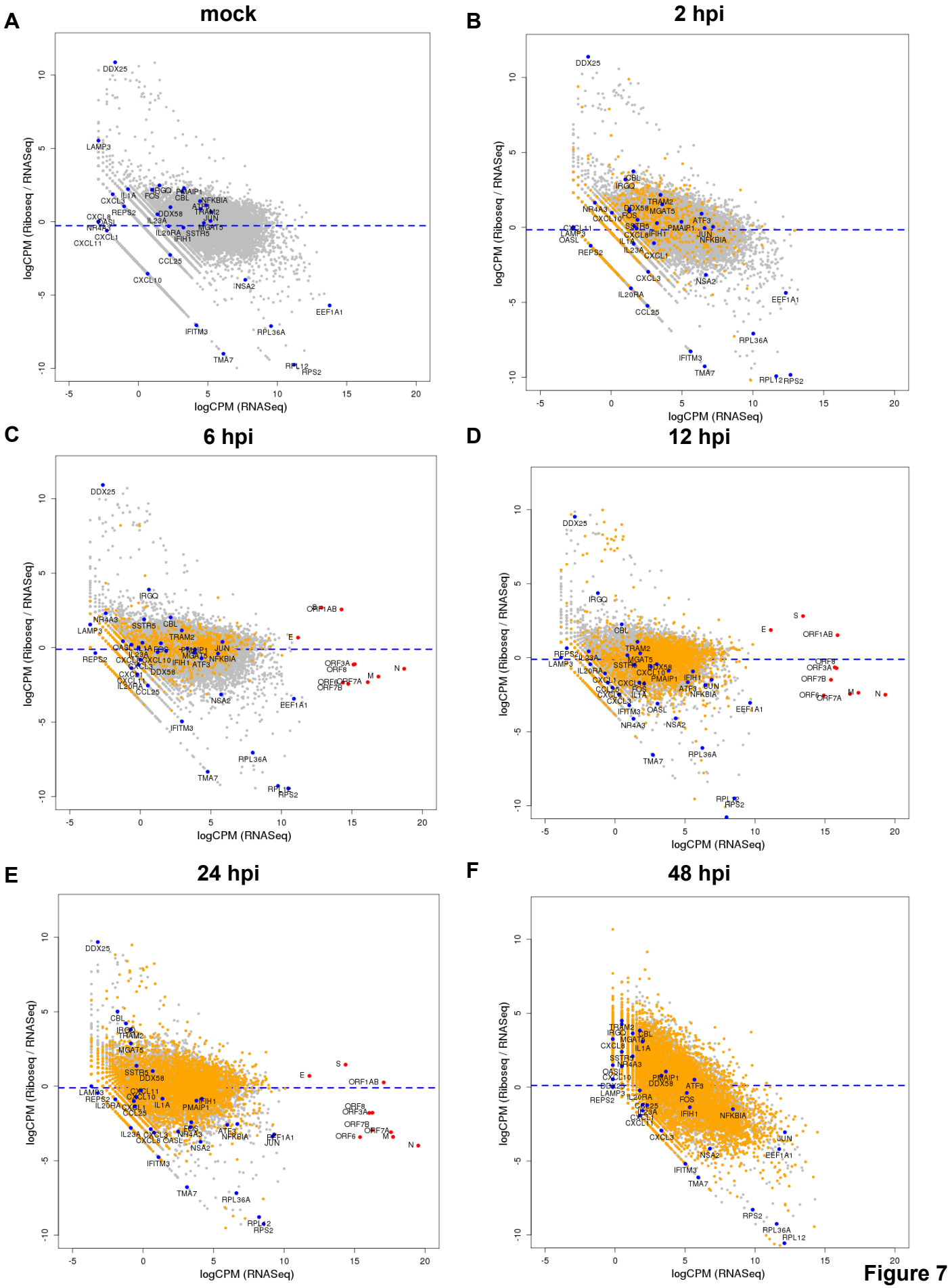
A
mock
B
2 hpi
C
6 hpi
D
12 hpi
E
24 hpi
F
48 hpi
logCPM (Riboseq / RNASeq)
logCPM (RNASeq)

Figure 7

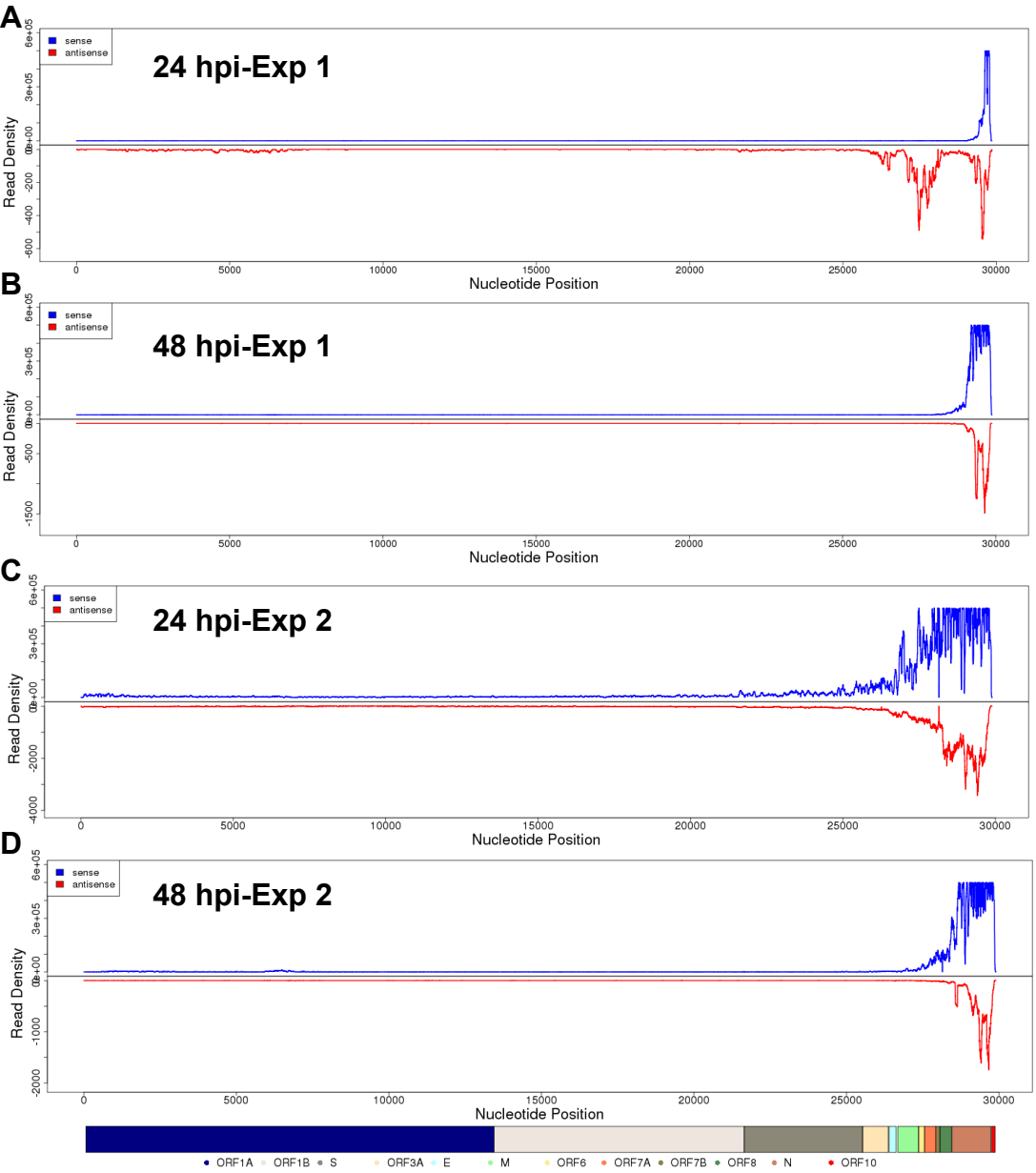
A
24 hpi-Exp 1
sense
antisense
Read Density
Nucleotide Position
B
48 hpi-Exp 1
C
24 hpi-Exp 2
D
48 hpi-Exp 2
ORF1A
ORF1B
S
ORF3A
E
M
ORF6
ORF7A
ORF7B
ORF8
N
ORF10

Figure S1

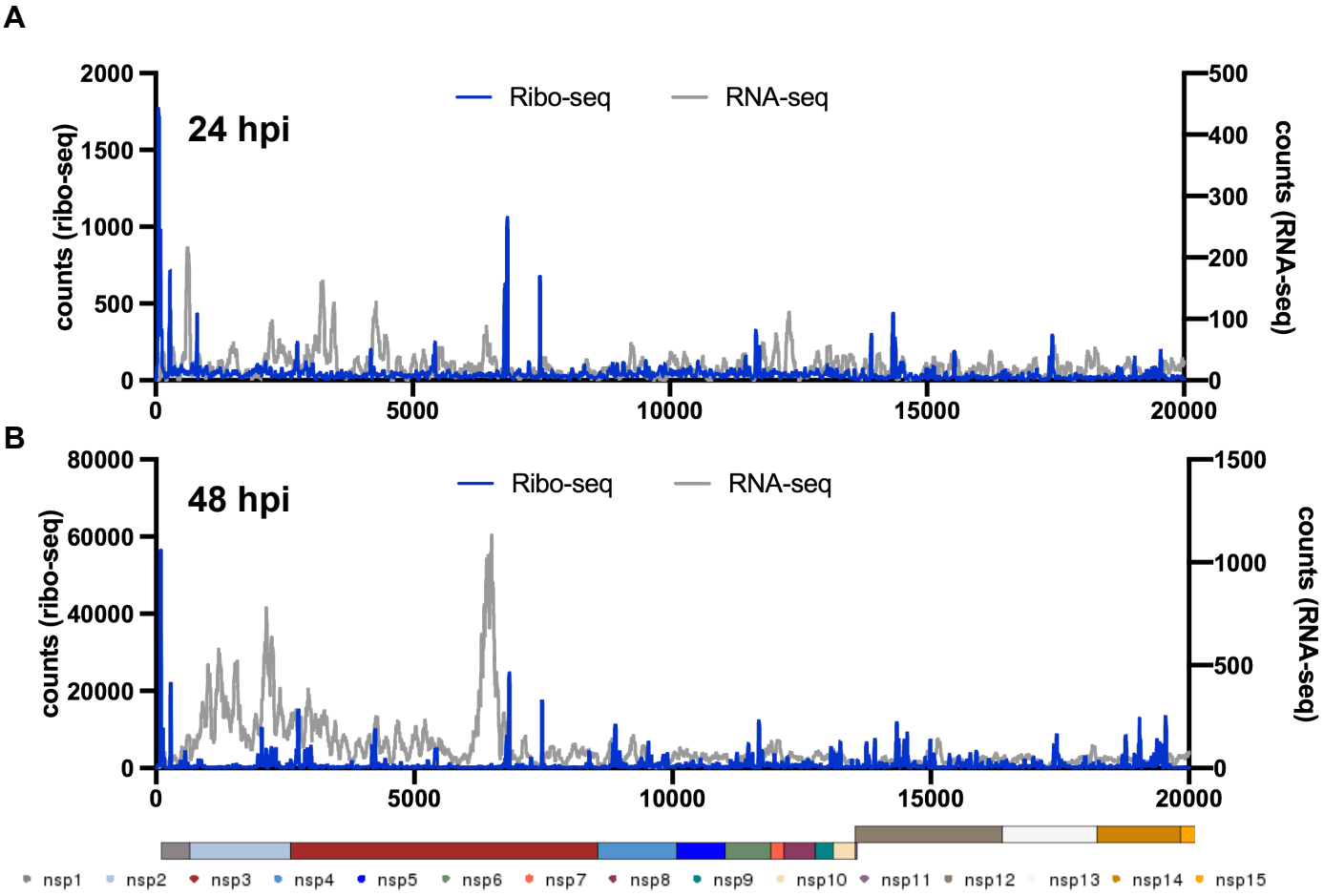
A
24 hpi
Ribo-seq
RNA-seq
counts (ribo-seq)
counts (RNA-seq)
2000
1500
1000
500
0
500
400
300
200
100
0
0
5000
10000
15000
20000
B
48 hpi
Ribo-seq
RNA-seq
counts (ribo-seq)
counts (RNA-seq)
80000
60000
40000
20000
0
1500
1000
500
0
0
5000
10000
15000
20000
nsp1
nsp2
nsp3
nsp4
nsp5
nsp6
nsp7
nsp8
nsp9
nsp10
nsp11
nsp12
nsp13
nsp14
nsp15

Figure S2

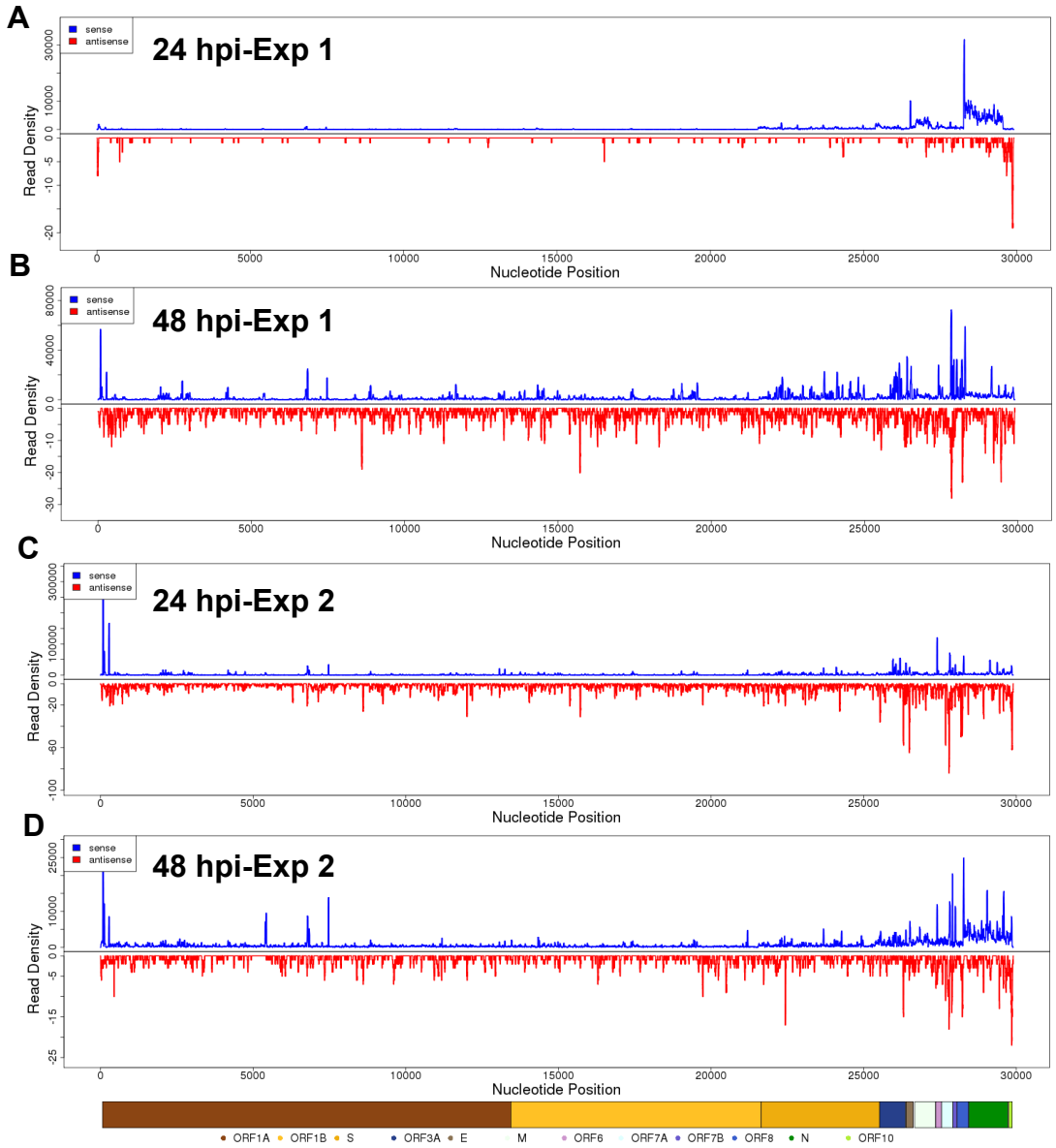
A
sense
antisense
24 hpi-Exp 1
Read Density
Nucleotide Position
B
48 hpi-Exp 1
C
24 hpi-Exp 2
D
48 hpi-Exp 2
ORF1A
ORF1B
S
ORF3A
E
M
ORF6
ORF7A
ORF7B
ORF8
N
ORF10

Figure S3

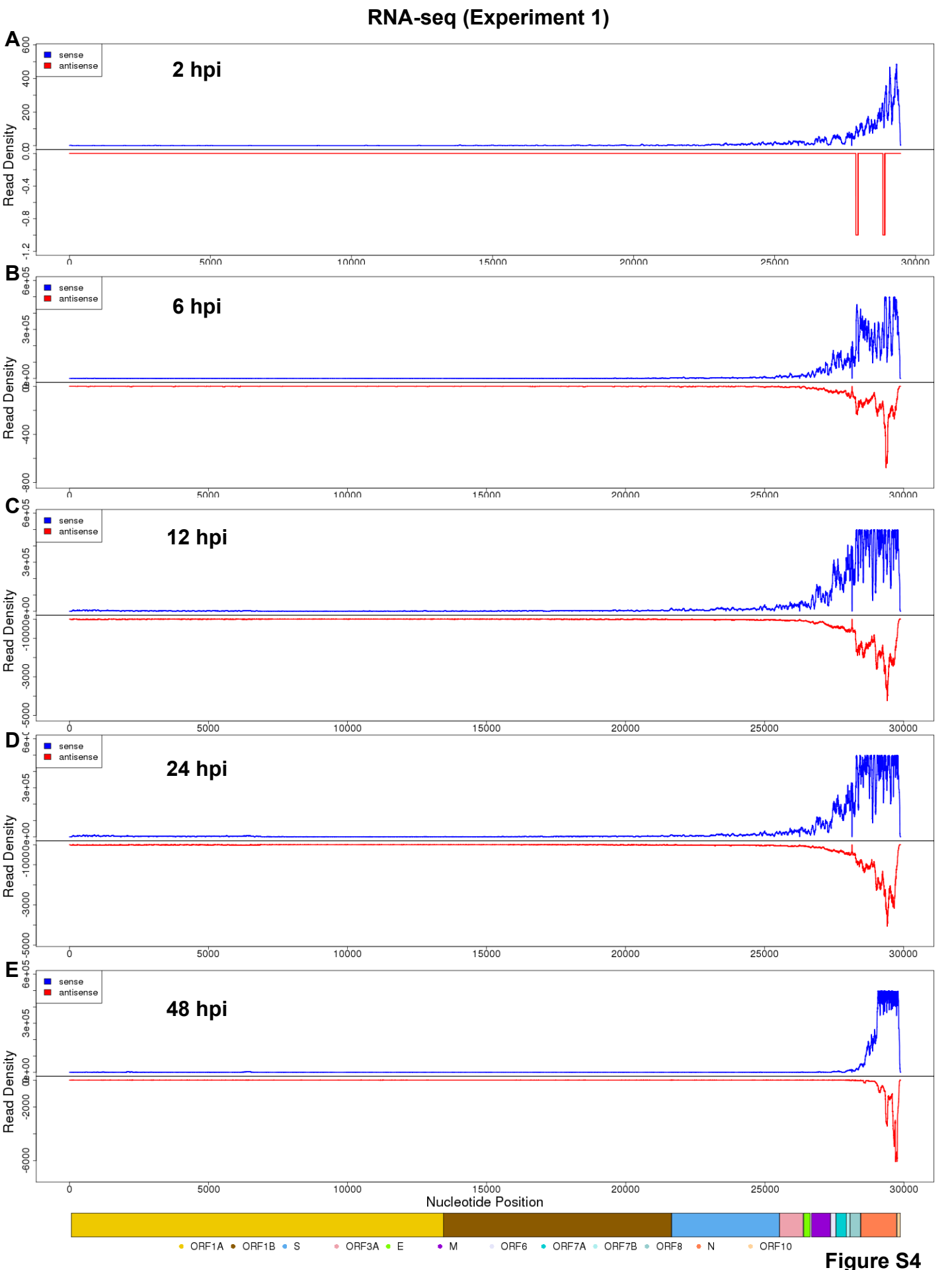
RNA-seq (Experiment 1)
A
2 hpi
B
6 hpi
C
12 hpi
D
24 hpi
E
48 hpi
sense
antisense
Read Density
Nucleotide Position
ORF1A
ORF1B
S
ORF3A
E
M
ORF6
ORF7A
ORF7B
ORF8
N
ORF10

Figure S4

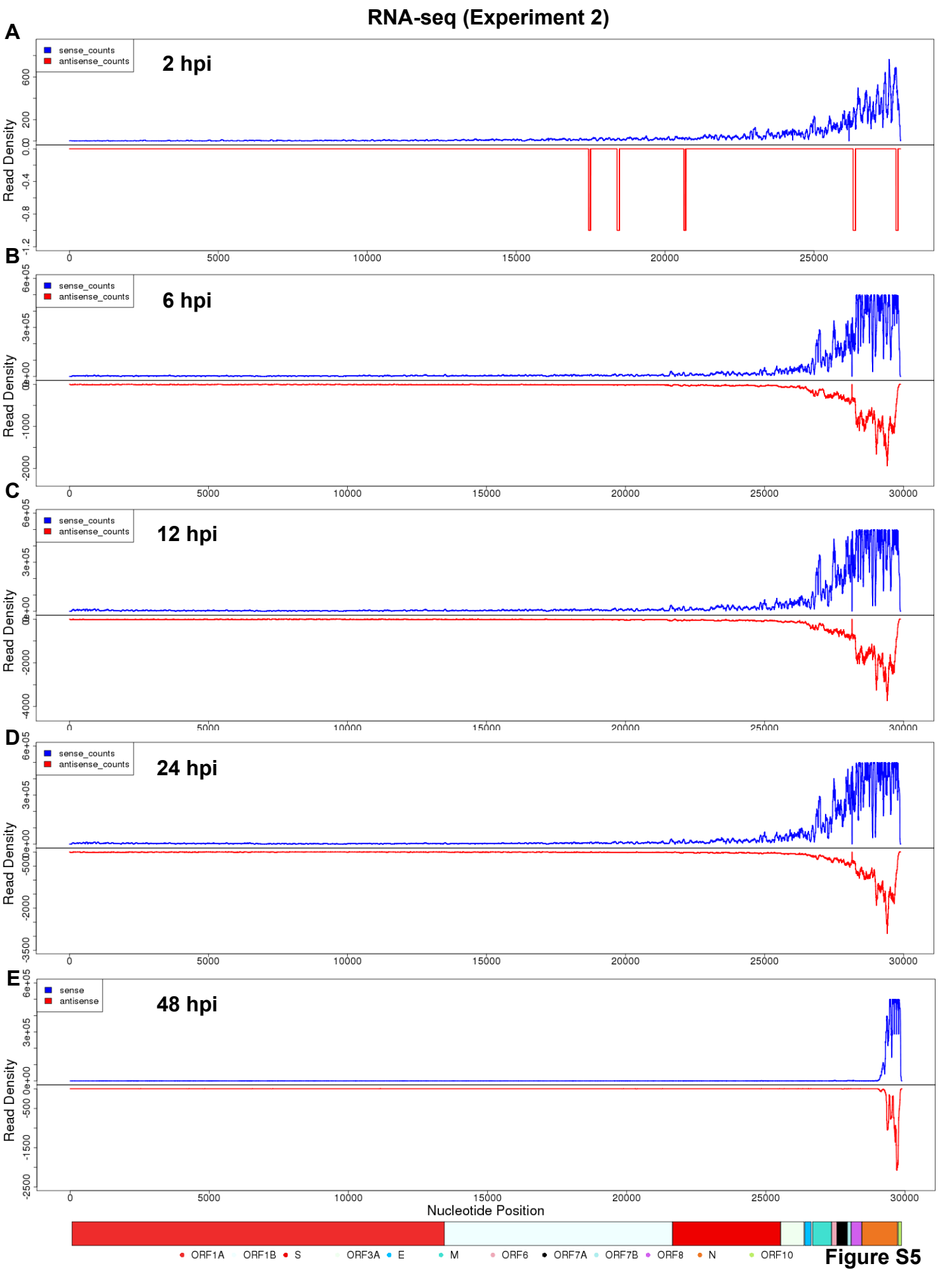
RNA-seq (Experiment 2)
A
2 hpi
sense_counts
antisense_counts
Read Density
B
6 hpi
C
12 hpi
D
24 hpi
E
48 hpi
sense
antisense
Nucleotide Position
ORF1A
ORF1B
S
ORF3A
E
M
ORF6
ORF7A
ORF7B
ORF8
N
ORF10
Figure S5

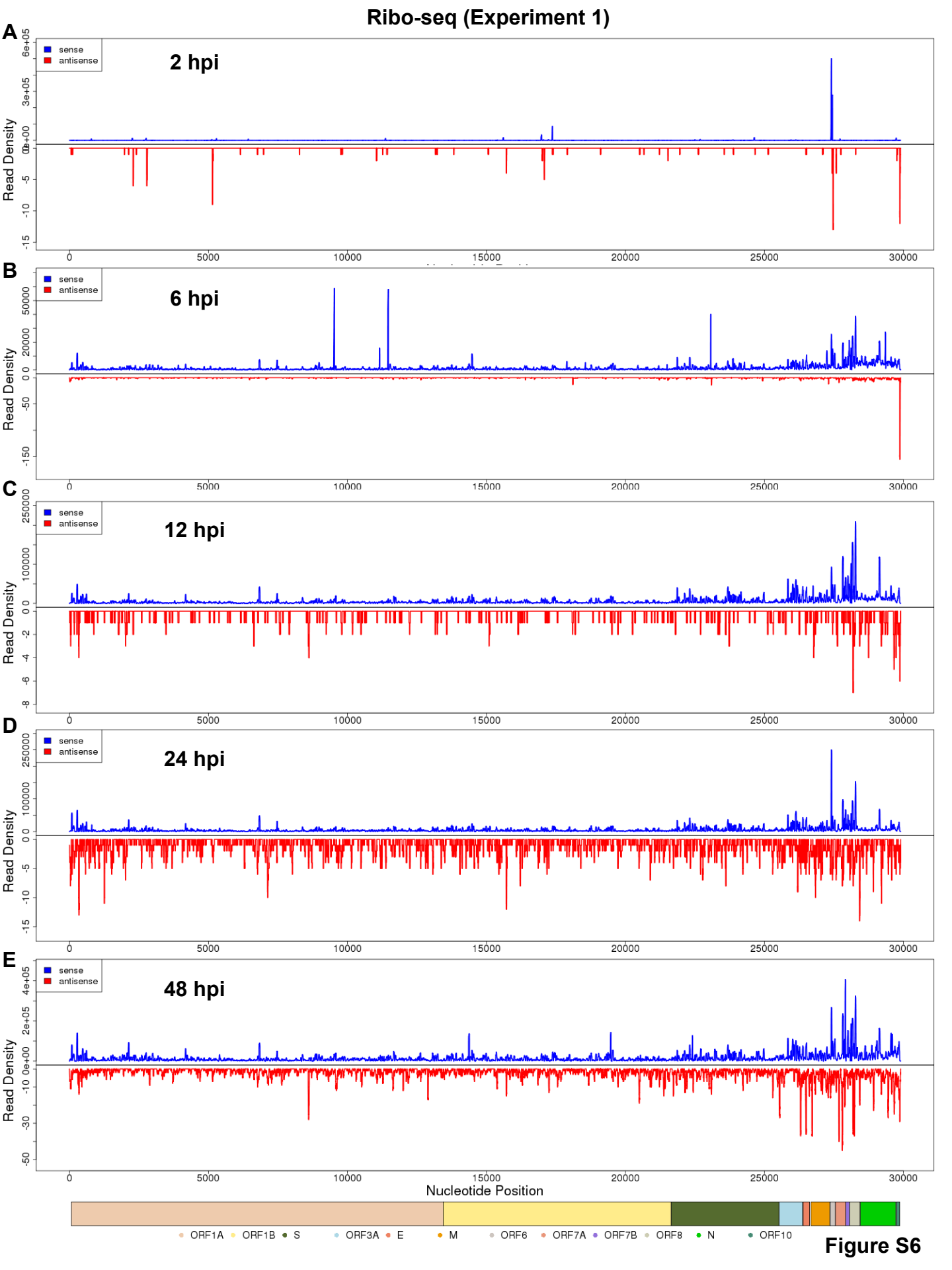
Ribo-seq (Experiment 1)
A
2 hpi
B
6 hpi
C
12 hpi
D
24 hpi
E
48 hpi
sense
antisense
Read Density
Nucleotide Position
ORF1A
ORF1B
S
ORF3A
E
M
ORF6
ORF7A
ORF7B
ORF8
N
ORF10

Figure S6

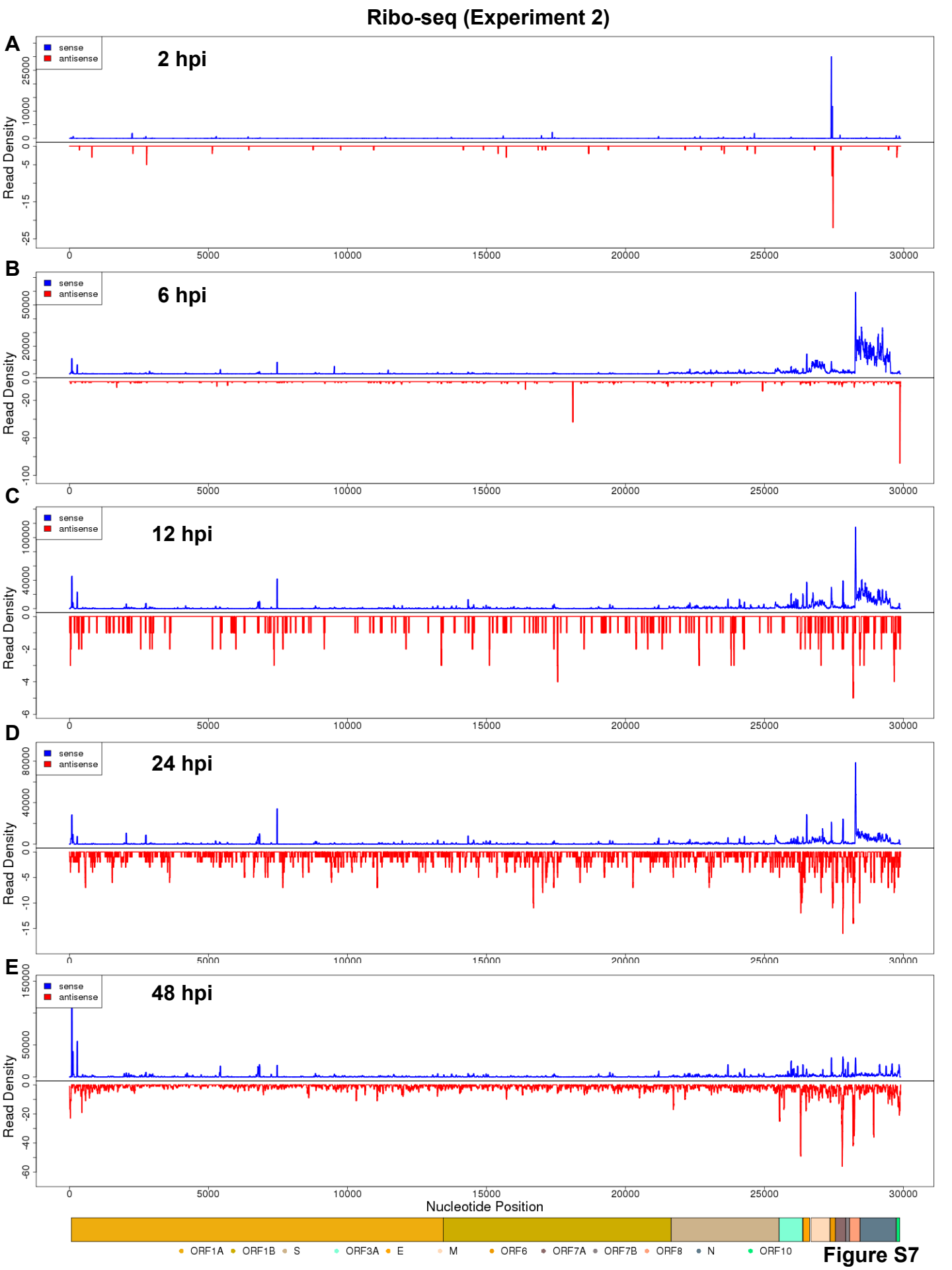
Ribo-seq (Experiment 2)
A
2 hpi
B
6 hpi
C
12 hpi
D
24 hpi
E
48 hpi
sense
antisense
Read Density
Nucleotide Position
ORF1A
ORF1B
S
ORF3A
E
M
ORF6
ORF7A
ORF7B
ORF8
N
ORF10

Figure S7

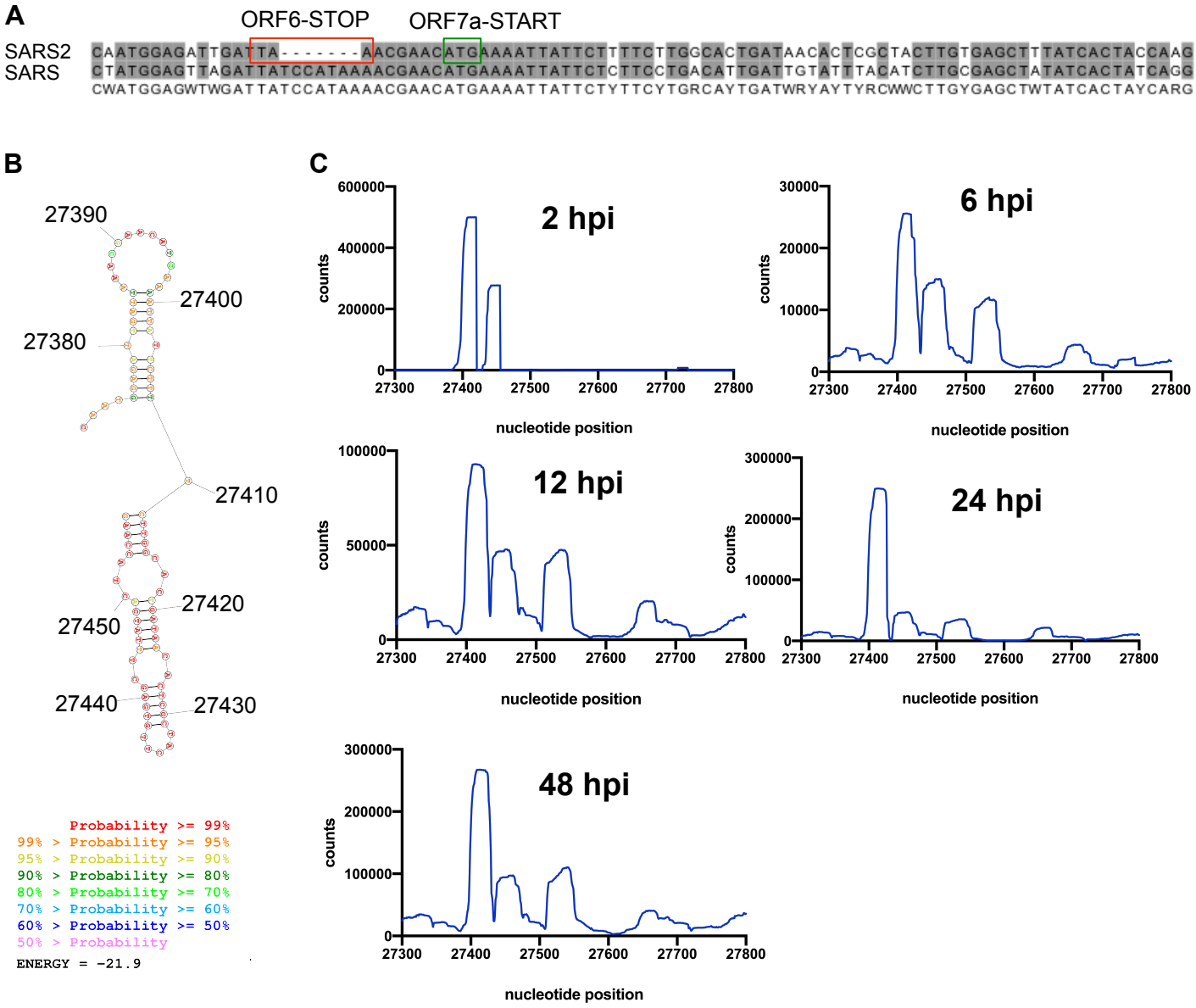
A
ORF6-STOP
ORF7a-START
SARS2
SARS
B
27390
27400
27380
27410
27420
27450
27440
27430
Probability >= 99%
99% > Probability >= 95%
95% > Probability >= 90%
90% > Probability >= 80%
80% > Probability >= 70%
70% > Probability >= 60%
60% > Probability >= 50%
50% > Probability
ENERGY = -21.9
C
2 hpi
6 hpi
12 hpi
24 hpi
48 hpi
counts
nucleotide position

Figure S8

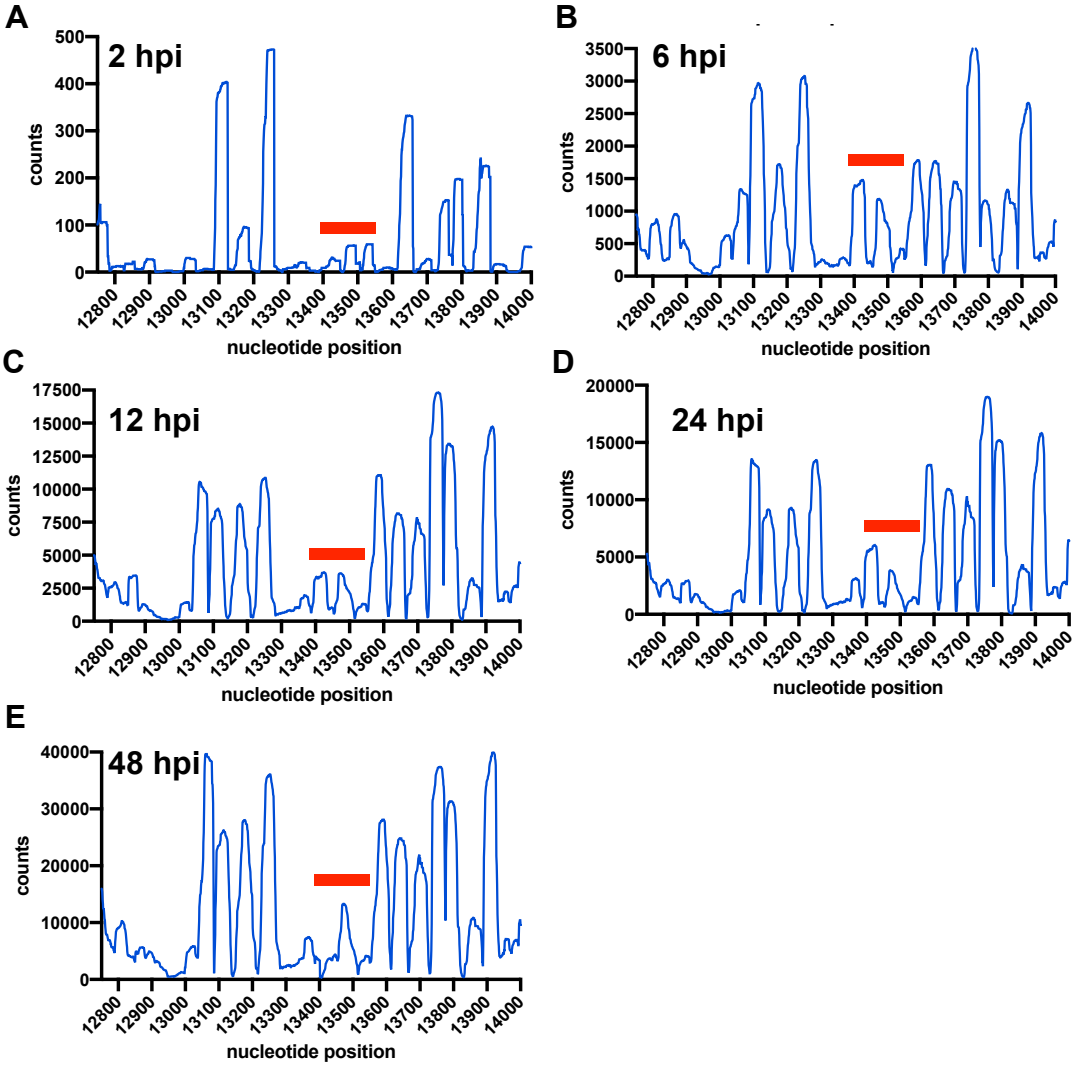
A
2 hpi
counts
nucleotide position
B
6 hpi
counts
nucleotide position
C
12 hpi
counts
nucleotide position
D
24 hpi
counts
nucleotide position
E
48 hpi
counts
nucleotide position

Figure S9

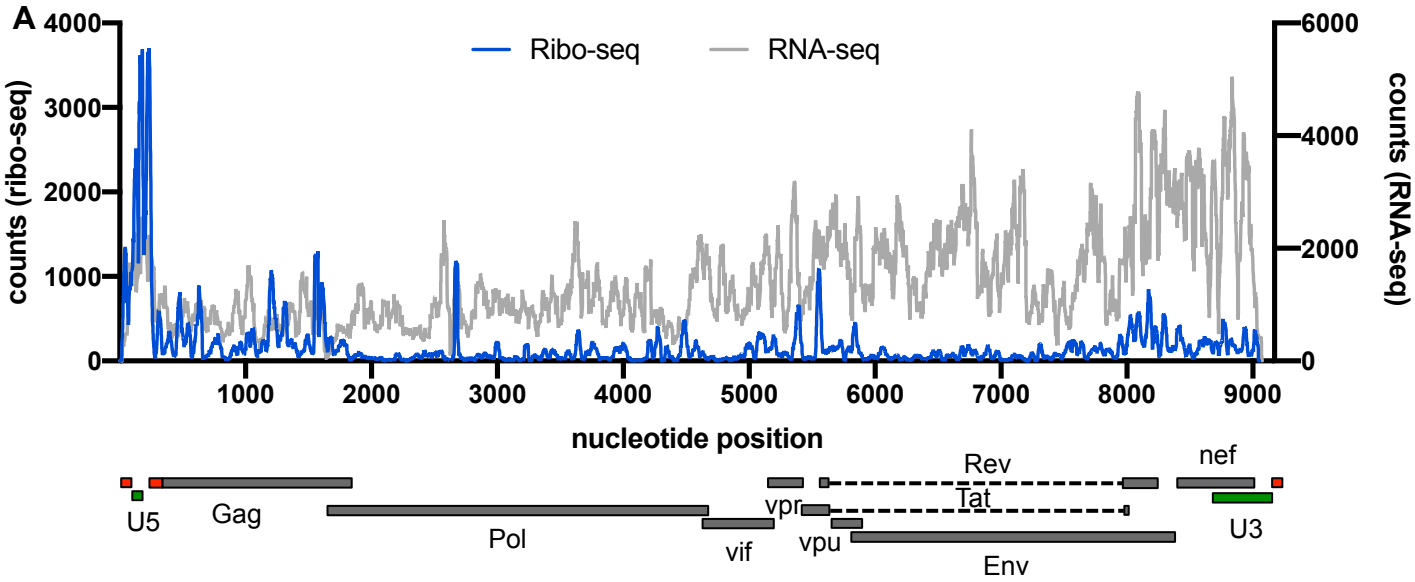

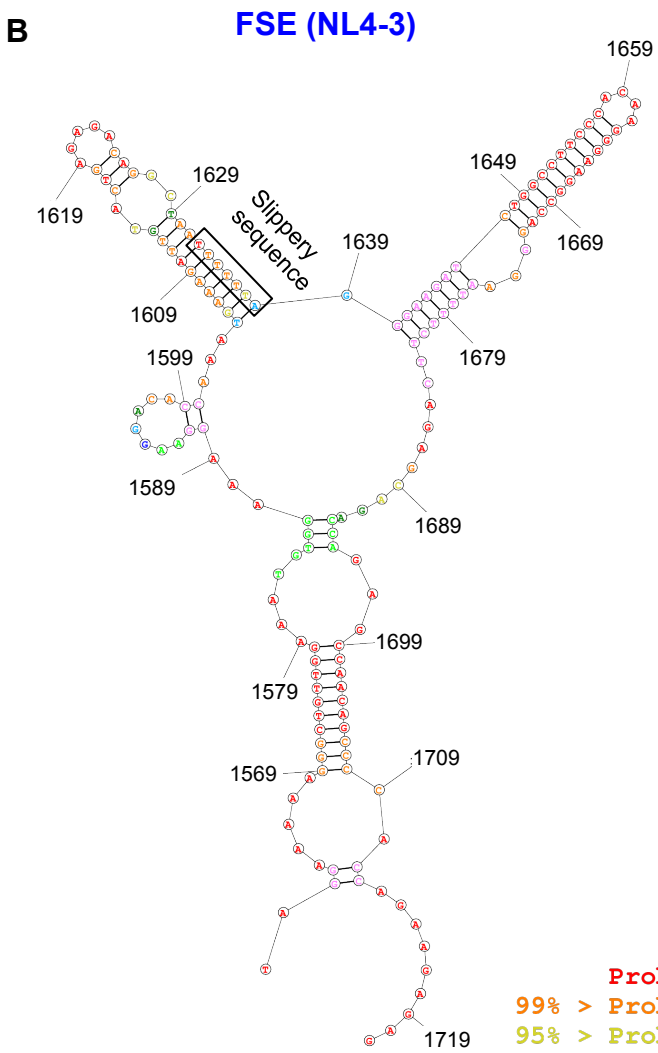

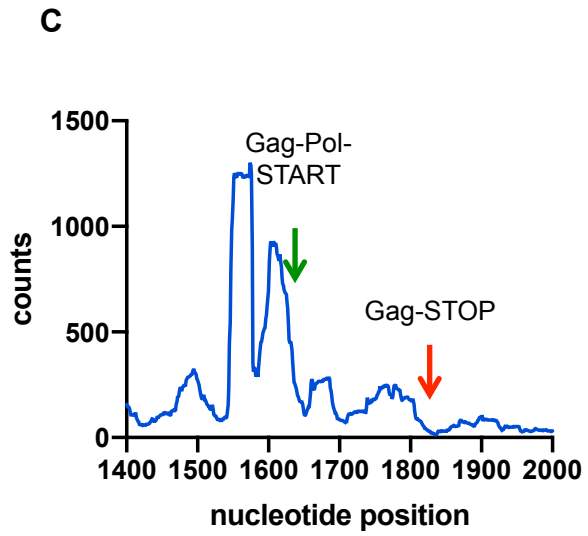

Probability >= 99%
99% > Probability >= 95%
95% > Probability >= 90%
90% > Probability >= 80%
80% > Probability >= 70%
70% > Probability >= 60%
60% > Probability >= 50%
50% > Probability

ENERGY = -53.7 HIV-1559-1720

Figure S10

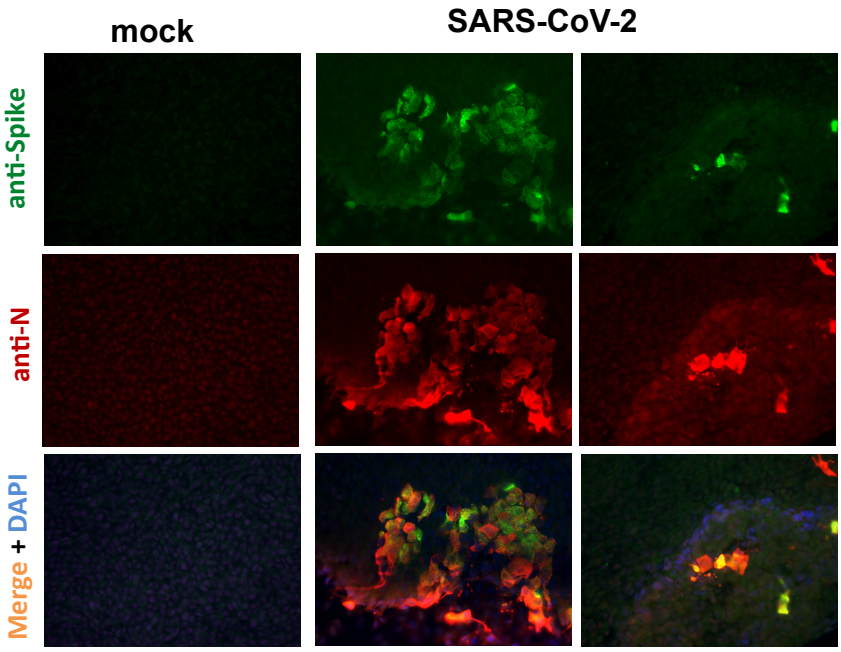

Figure S11

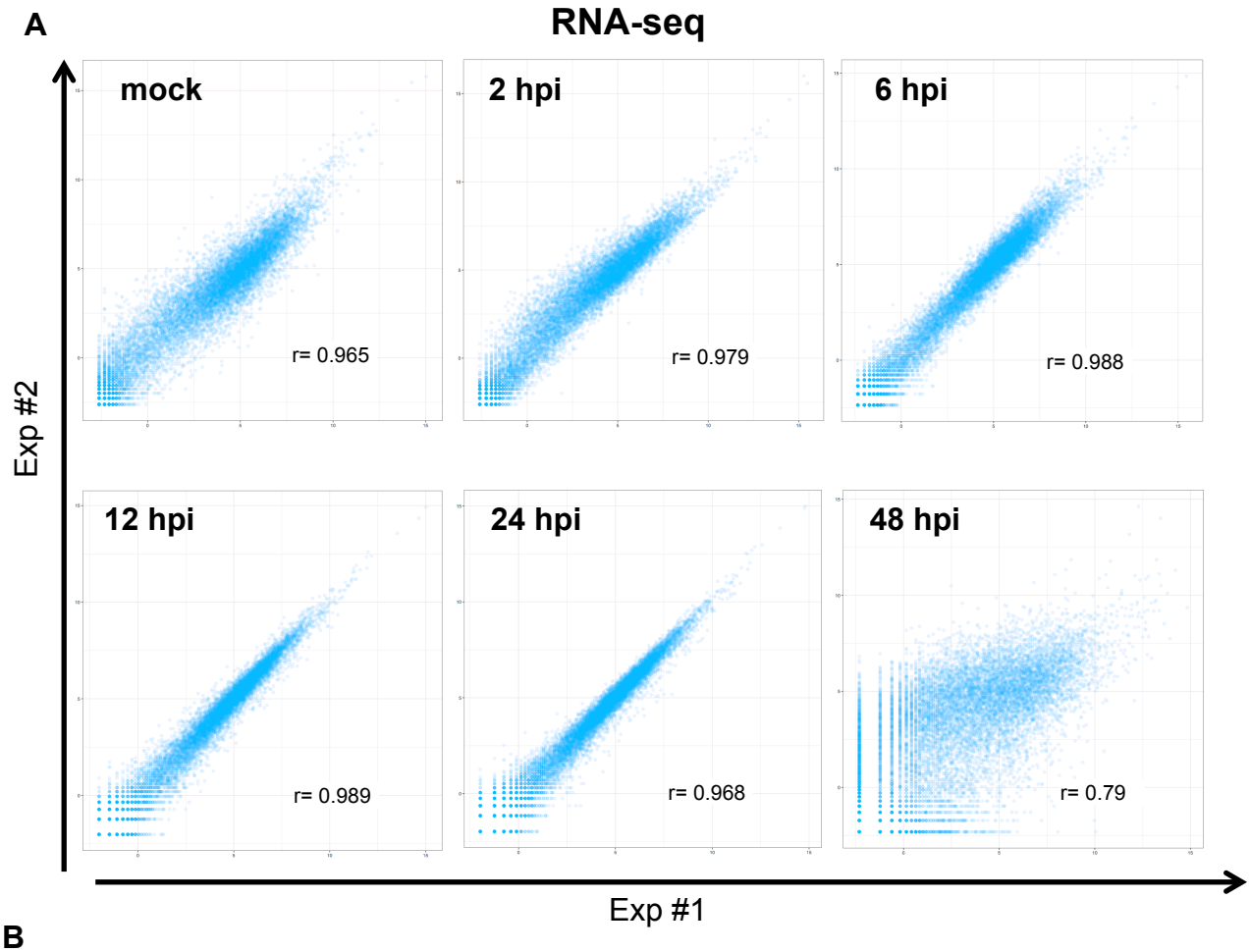
A
RNA-seq
mock
r= 0.965
2 hpi
r= 0.979
6 hpi
r= 0.988
12 hpi
r= 0.989
24 hpi
r= 0.968
48 hpi
r= 0.79
Exp #2
Exp #1

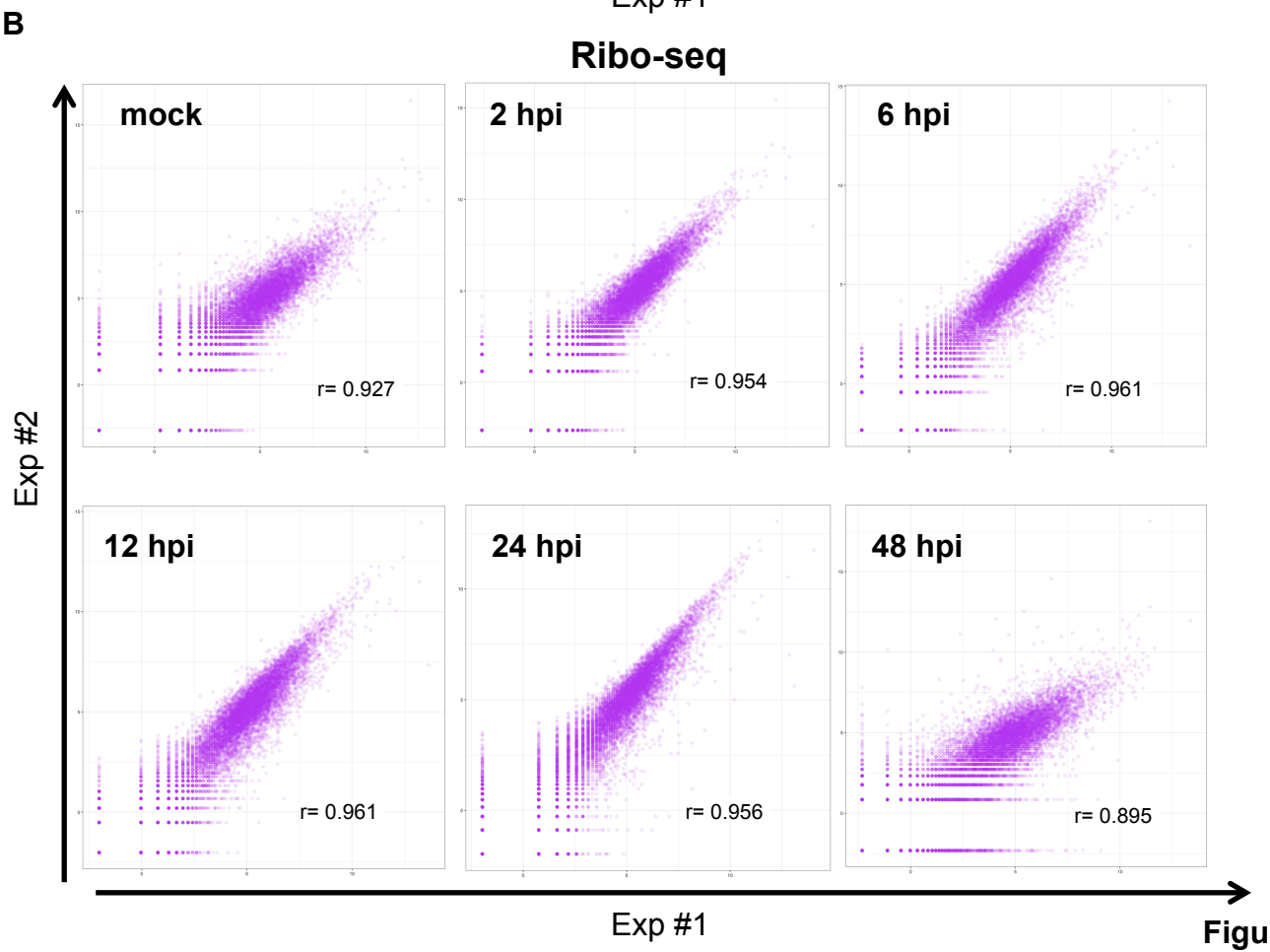
B
Ribo-seq
mock
r= 0.927
2 hpi
r= 0.954
6 hpi
r= 0.961
12 hpi
r= 0.961
24 hpi
r= 0.956
48 hpi
r= 0.895
Exp #2
Exp #1

Figure S12

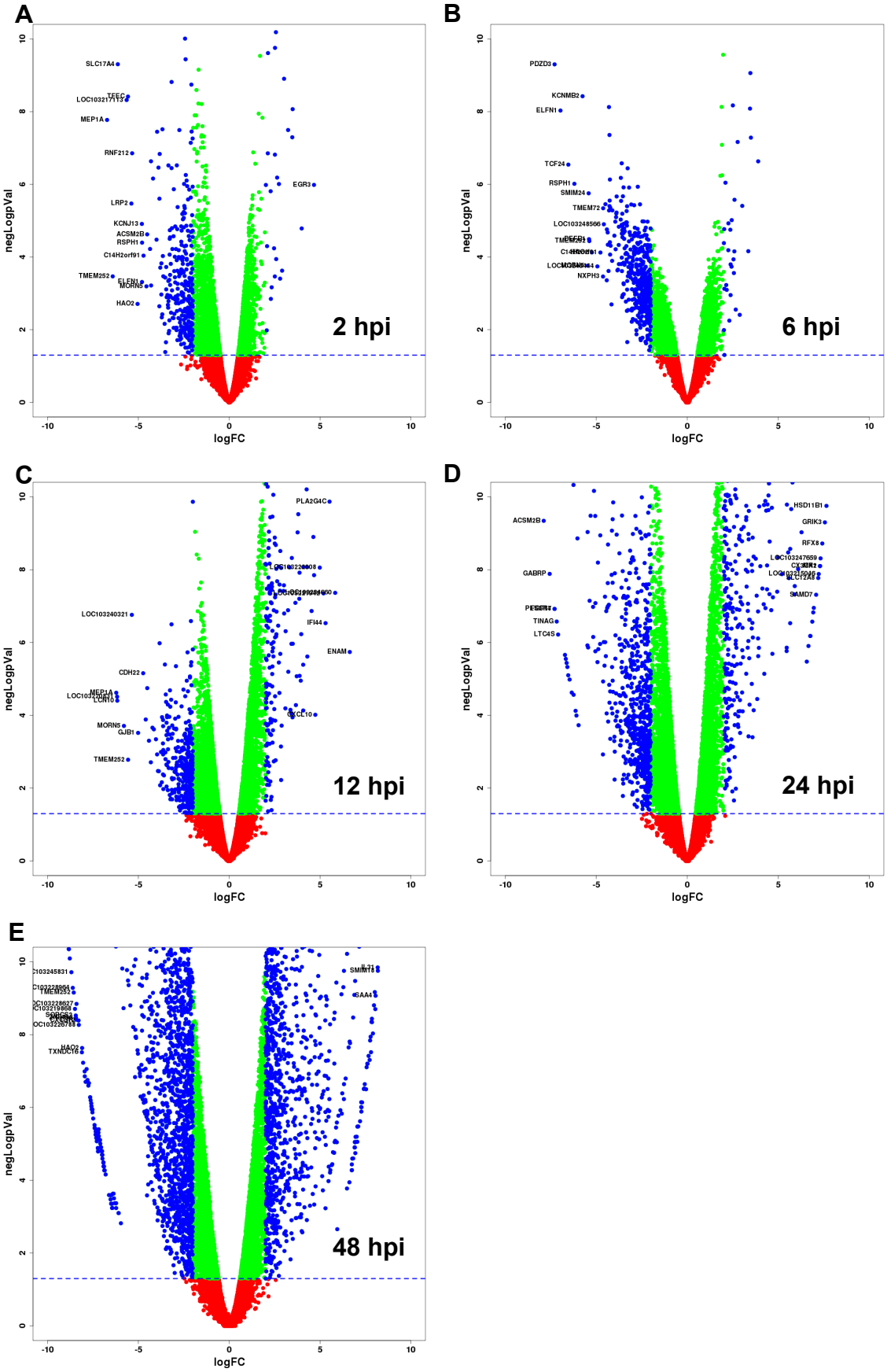
A
SLC17A4
LOC103217112
MEP1A
RNF212
EGR3
LRP2
KCNJ13
ACSM2B
RSPH1
C14H2orf91
TMEM252
MORN5
HAO2
2 hpi
B
PDZD3
KCNMB2
ELFN1
TCF24
RSPH1
SMIM24
TMEM72
LOC103248566
NXPH3
6 hpi
C
PLA2G4C
LOC103240321
IFI44
ENAM
CDH22
MEG1A
LCN10
CXCL10
MORN5
GJB1
TMEM252
12 hpi
D
ACSM2B
HSD11B1
GRIK3
RFX8
LOC103247659
GABRP
SAMD7
TINAG
LTC4S
24 hpi
E
SMIM18
SAA4
HAO2
TXNDC16
48 hpi
negLogpVal
logFC

Figure S13

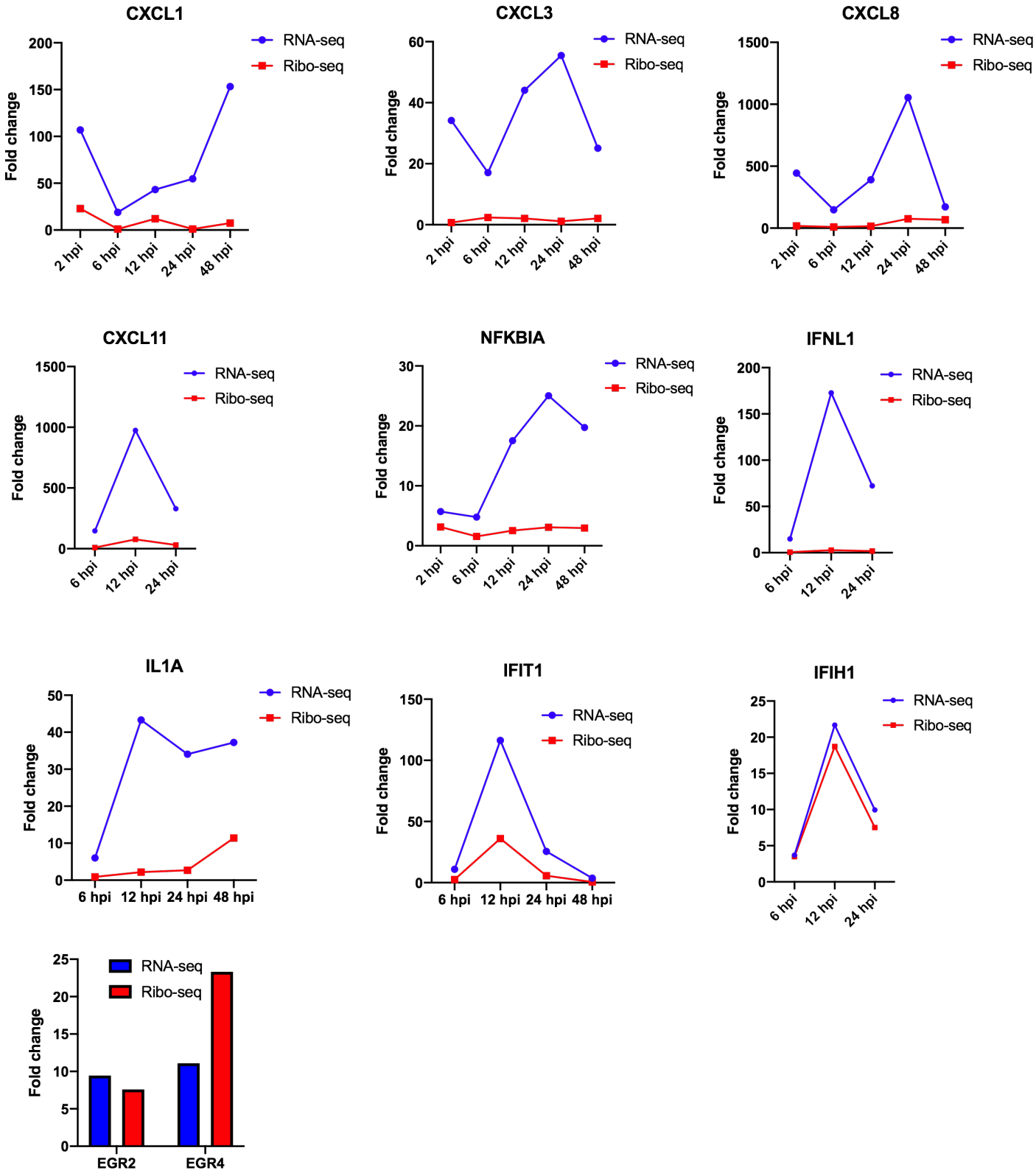
CXCL1
CXCL3
CXCL8
CXCL11
NFKBIA
IFNL1
IL1A
IFIT1
IFIH1
RNA-seq
Ribo-seq
Fold change
2 hpi
6 hpi
12 hpi
24 hpi
48 hpi
EGR2
EGR4

Figure S14

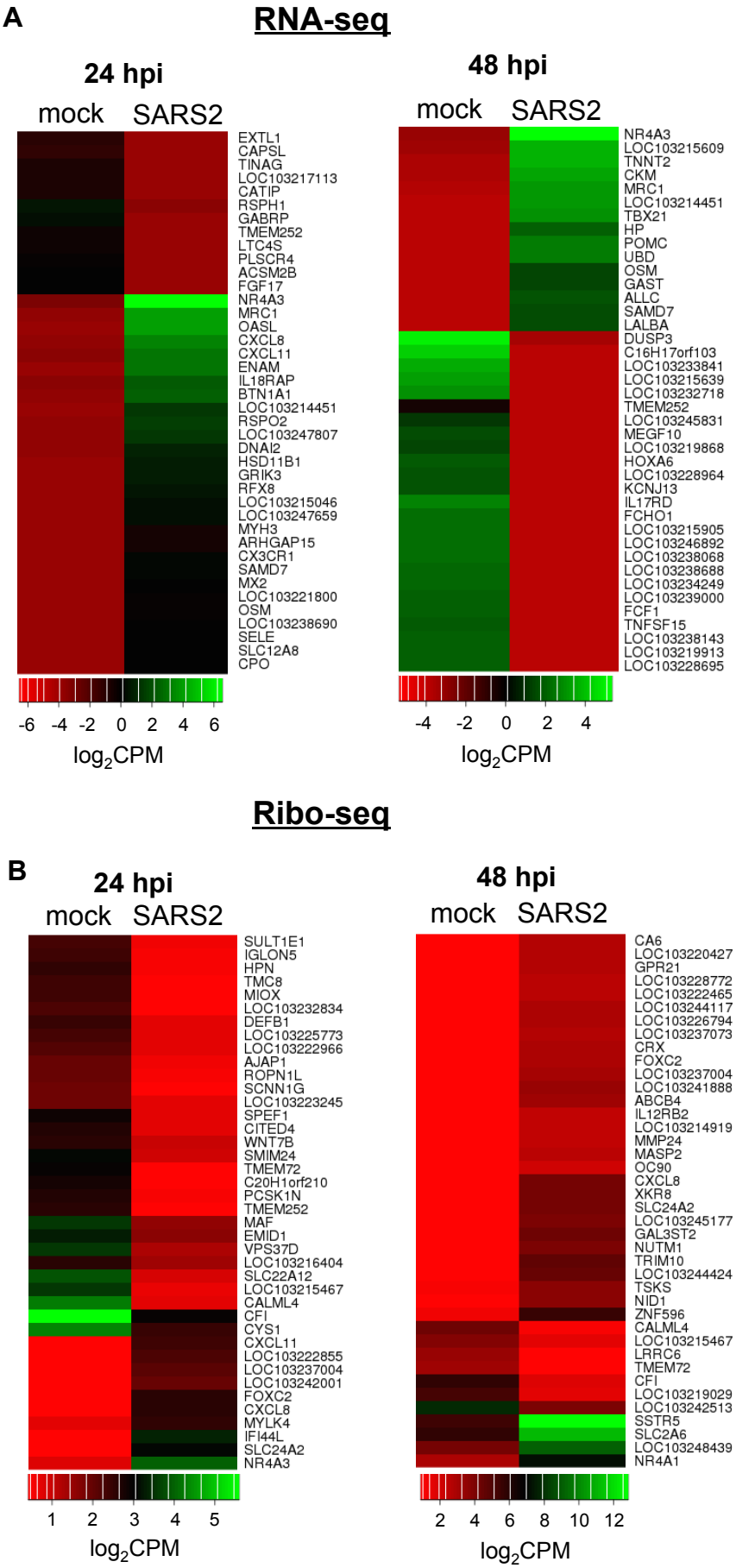
A
RNA-seq
24 hpi
mock
SARS2
EXTL1
CAPSL
TINAG
LOC103217113
CATIP
RSPH1
GABRP
TMEM252
LTC4S
PLSCR4
ACSM2B
FGF17
NR4A3
MRC1
OASL
CXCL8
CXCL11
ENAM
IL18RAP
BTN1A1
LOC103214451
RSPO2
LOC103247807
DNAI2
HSD11B1
GRIK3
RFX8
LOC103215046
LOC103247659
MYH3
ARHGAP15
CX3CR1
SAMD7
MX2
LOC103221800
OSM
LOC103238690
SELE
SLC12A8
CPO
-6 -4 -2 0 2 4 6
log2CPM
48 hpi
mock
SARS2
NR4A3
LOC103215609
TNNT2
CKM
MRC1
LOC103214451
TBX21
HP
POMC
UBD
OSM
GAST
ALLC
SAMD7
LALBA
DUSP3
C16H17orf103
LOC103233841
LOC103215639
LOC103232718
TMEM252
LOC103245831
MEGF10
LOC103219868
HOXA6
LOC103228964
KCNJ13
IL17RD
FCHO1
LOC103215905
LOC103246892
LOC103238068
LOC103238688
LOC103234249
LOC103239000
FCF1
TNFSF15
LOC103238143
LOC103219913
LOC103228695
-4 -2 0 2 4
log2CPM
Ribo-seq
B
24 hpi
mock
SARS2
SULT1E1
IGLON5
HPN
TMC8
MIOX
LOC103232834
DEFB1
LOC103225773
LOC103222966
AJAP1
ROPN1L
SCNN1G
LOC103223245
SPEF1
CITED4
WNT7B
SMIM24
TMEM72
C20H1orf210
PCSK1N
TMEM252
MAF
EMID1
VPS37D
LOC103216404
SLC22A12
LOC103215467
CALML4
CFI
CYS1
CXCL11
LOC103222855
LOC103237004
LOC103242001
FOXC2
CXCL8
MYLK4
IFI44L
SLC24A2
NR4A3
1 2 3 4 5
log2CPM
48 hpi
mock
SARS2
CA6
LOC103220427
GPR21
LOC103228772
LOC103222465
LOC103244117
LOC103226794
LOC103237073
CRX
FOXC2
LOC103237004
LOC103241888
ABCB4
IL12RB2
LOC103214919
MMP24
MASP2
OC90
CXCL8
XKR8
SLC24A2
LOC103245177
GAL3ST2
NUTM1
TRIM10
LOC103244424
TSKS
NID1
ZNF596
CALML4
LOC103215467
LRRC6
TMEM72
CFI
LOC103219029
LOC103242513
SSTR5
SLC2A6
LOC103248439
NR4A1
2 4 6 8 10 12
log2CPM

Figure S15

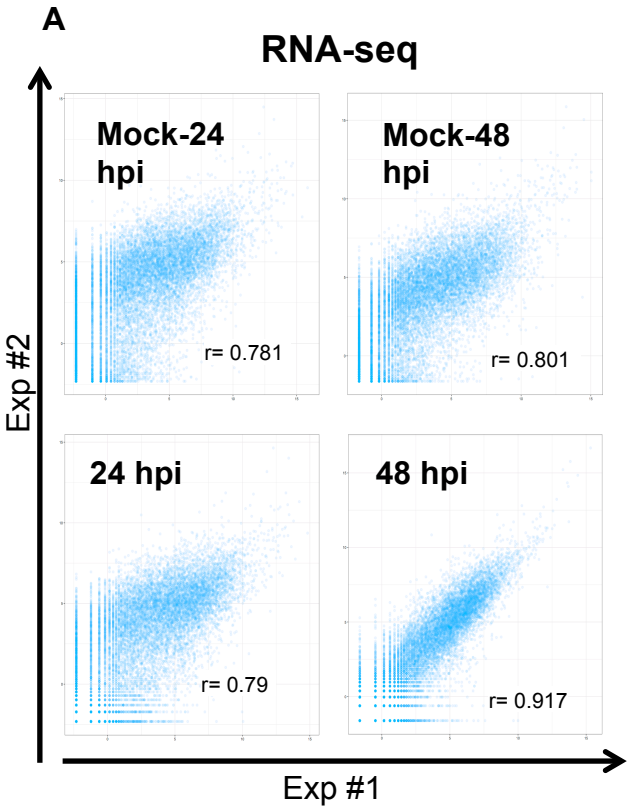
A
RNA-seq
Mock-24 hpi
r= 0.781
Mock-48 hpi
r= 0.801
24 hpi
r= 0.79
48 hpi
r= 0.917
Exp #2
Exp #1

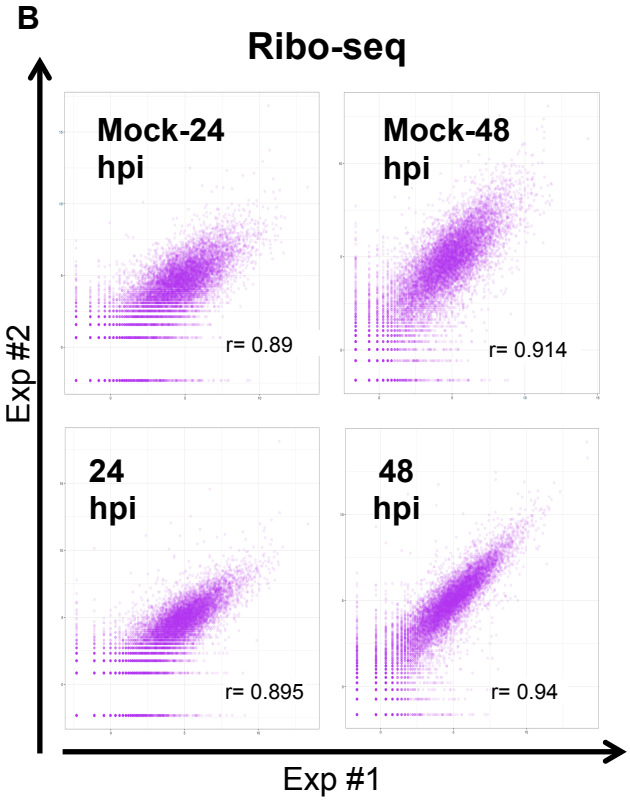
B
Ribo-seq
Mock-24 hpi
r= 0.89
Mock-48 hpi
r= 0.914
24 hpi
r= 0.895
48 hpi
r= 0.94
Exp #2
Exp #1

Figure S16

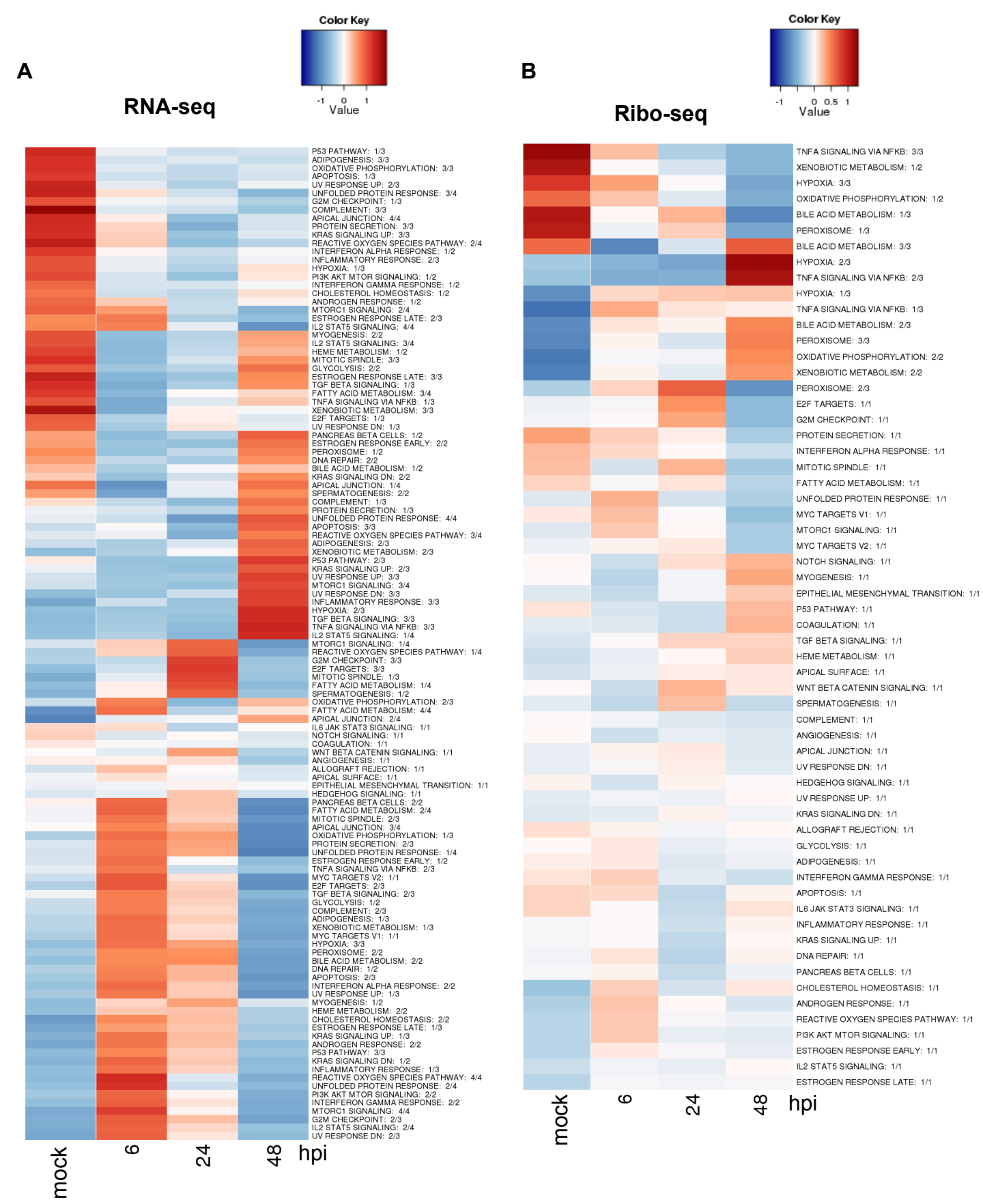
A
RNA-seq
Color Key
-1 0 1
Value
P53 PATHWAY: 1/3
ADIPOGENESIS: 3/3
OXIDATIVE PHOSPHORYLATION: 3/3
APOPTOSIS: 1/3
UV RESPONSE UP: 2/3
UNFOLDED PROTEIN RESPONSE: 3/4
G2M CHECKPOINT: 1/3
COMPLEMENT: 3/3
APICAL JUNCTION: 4/4
PROTEIN SECRETION: 3/3
KRAS SIGNALING UP: 3/3
REACTIVE OXYGEN SPECIES PATHWAY: 2/4
INTERFERON ALPHA RESPONSE: 1/2
INFLAMMATORY RESPONSE: 2/3
HYPOXIA: 1/3
PI3K AKT MTOR SIGNALING: 1/2
INTERFERON GAMMA RESPONSE: 1/2
CHOLESTEROL HOMEOSTASIS: 1/2
ANDROGEN RESPONSE: 1/2
MTORC1 SIGNALING: 2/4
ESTROGEN RESPONSE LATE: 2/3
IL2 STAT5 SIGNALING: 4/4
MYOGENESIS: 2/2
IL2 STAT5 SIGNALING: 3/4
HEME METABOLISM: 1/2
MITOTIC SPINDLE: 3/3
GLYCOLYSIS: 2/2
ESTROGEN RESPONSE LATE: 3/3
TGF BETA SIGNALING: 1/3
FATTY ACID METABOLISM: 3/4
TNFA SIGNALING VIA NFKB: 1/3
XENOBIOTIC METABOLISM: 3/3
E2F TARGETS: 1/3
UV RESPONSE DN: 1/3
PANCREAS BETA CELLS: 1/2
ESTROGEN RESPONSE EARLY: 2/2
PEROXISOME: 1/2
DNA REPAIR: 2/2
BILE ACID METABOLISM: 1/2
KRAS SIGNALING DN: 2/2
APICAL JUNCTION: 1/4
SPERMATOGENESIS: 2/2
COMPLEMENT: 1/3
PROTEIN SECRETION: 1/3
UNFOLDED PROTEIN RESPONSE: 4/4
APOPTOSIS: 3/3
REACTIVE OXYGEN SPECIES PATHWAY: 3/4
ADIPOGENESIS: 2/3
XENOBIOTIC METABOLISM: 2/3
P53 PATHWAY: 2/3
KRAS SIGNALING UP: 2/3
UV RESPONSE UP: 3/3
MTORC1 SIGNALING: 3/4
UV RESPONSE DN: 3/3
INFLAMMATORY RESPONSE: 3/3
HYPOXIA: 2/3
TGF BETA SIGNALING: 3/3
TNFA SIGNALING VIA NFKB: 3/3
IL2 STAT5 SIGNALING: 1/4
MTORC1 SIGNALING: 1/4
REACTIVE OXYGEN SPECIES PATHWAY: 1/4
G2M CHECKPOINT: 3/3
E2F TARGETS: 3/3
MITOTIC SPINDLE: 1/3
FATTY ACID METABOLISM: 1/4
SPERMATOGENESIS: 1/2
OXIDATIVE PHOSPHORYLATION: 2/3
FATTY ACID METABOLISM: 4/4
APICAL JUNCTION: 2/4
IL6 JAK STAT3 SIGNALING: 1/1
NOTCH SIGNALING: 1/1
COAGULATION: 1/1
WNT BETA CATENIN SIGNALING: 1/1
ANGIOGENESIS: 1/1
ALLOGRAFT REJECTION: 1/1
APICAL SURFACE: 1/1
EPITHELIAL MESENCHYMAL TRANSITION: 1/1
HEDGEHOG SIGNALING: 1/1
PANCREAS BETA CELLS: 2/2
FATTY ACID METABOLISM: 2/4
MITOTIC SPINDLE: 2/3
APICAL JUNCTION: 3/4
OXIDATIVE PHOSPHORYLATION: 1/3
PROTEIN SECRETION: 2/3
UNFOLDED PROTEIN RESPONSE: 1/4
ESTROGEN RESPONSE EARLY: 1/2
TNFA SIGNALING VIA NFKB: 2/3
MYC TARGETS V2: 1/1
E2F TARGETS: 2/3
TGF BETA SIGNALING: 2/3
GLYCOLYSIS: 1/2
COMPLEMENT: 2/3
ADIPOGENESIS: 1/3
XENOBIOTIC METABOLISM: 1/3
MYC TARGETS V1: 1/1
HYPOXIA: 3/3
PEROXISOME: 2/2
BILE ACID METABOLISM: 2/2
DNA REPAIR: 1/2
APOPTOSIS: 2/3
INTERFERON ALPHA RESPONSE: 2/2
UV RESPONSE UP: 1/3
MYOGENESIS: 1/2
HEME METABOLISM: 2/2
CHOLESTEROL HOMEOSTASIS: 2/2
ESTROGEN RESPONSE LATE: 1/3
KRAS SIGNALING UP: 1/3
ANDROGEN RESPONSE: 2/2
P53 PATHWAY: 3/3
KRAS SIGNALING DN: 1/2
INFLAMMATORY RESPONSE: 1/3
REACTIVE OXYGEN SPECIES PATHWAY: 4/4
UNFOLDED PROTEIN RESPONSE: 2/4
PI3K AKT MTOR SIGNALING: 2/2
INTERFERON GAMMA RESPONSE: 2/2
MTORC1 SIGNALING: 4/4
G2M CHECKPOINT: 2/3
IL2 STAT5 SIGNALING: 2/4
UV RESPONSE DN: 2/3
mock
6
24
48
hpi
B
Ribo-seq
Color Key
-1 0 0.5 1
Value
TNFA SIGNALING VIA NFKB: 3/3
XENOBIOTIC METABOLISM: 1/2
HYPOXIA: 3/3
OXIDATIVE PHOSPHORYLATION: 1/2
BILE ACID METABOLISM: 1/3
PEROXISOME: 1/3
BILE ACID METABOLISM: 3/3
HYPOXIA: 2/3
TNFA SIGNALING VIA NFKB: 2/3
HYPOXIA: 1/3
TNFA SIGNALING VIA NFKB: 1/3
BILE ACID METABOLISM: 2/3
PEROXISOME: 3/3
OXIDATIVE PHOSPHORYLATION: 2/2
XENOBIOTIC METABOLISM: 2/2
PEROXISOME: 2/3
E2F TARGETS: 1/1
G2M CHECKPOINT: 1/1
PROTEIN SECRETION: 1/1
INTERFERON ALPHA RESPONSE: 1/1
MITOTIC SPINDLE: 1/1
FATTY ACID METABOLISM: 1/1
UNFOLDED PROTEIN RESPONSE: 1/1
MYC TARGETS V1: 1/1
MTORC1 SIGNALING: 1/1
MYC TARGETS V2: 1/1
NOTCH SIGNALING: 1/1
MYOGENESIS: 1/1
EPITHELIAL MESENCHYMAL TRANSITION: 1/1
P53 PATHWAY: 1/1
COAGULATION: 1/1
TGF BETA SIGNALING: 1/1
HEME METABOLISM: 1/1
APICAL SURFACE: 1/1
WNT BETA CATENIN SIGNALING: 1/1
SPERMATOGENESIS: 1/1
COMPLEMENT: 1/1
ANGIOGENESIS: 1/1
APICAL JUNCTION: 1/1
UV RESPONSE DN: 1/1
HEDGEHOG SIGNALING: 1/1
UV RESPONSE UP: 1/1
KRAS SIGNALING DN: 1/1
ALLOGRAFT REJECTION: 1/1
GLYCOLYSIS: 1/1
ADIPOGENESIS: 1/1
INTERFERON GAMMA RESPONSE: 1/1
APOPTOSIS: 1/1
IL6 JAK STAT3 SIGNALING: 1/1
INFLAMMATORY RESPONSE: 1/1
KRAS SIGNALING UP: 1/1
DNA REPAIR: 1/1
PANCREAS BETA CELLS: 1/1
CHOLESTEROL HOMEOSTASIS: 1/1
ANDROGEN RESPONSE: 1/1
REACTIVE OXYGEN SPECIES PATHWAY: 1/1
PI3K AKT MTOR SIGNALING: 1/1
ESTROGEN RESPONSE EARLY: 1/1
IL2 STAT5 SIGNALING: 1/1
ESTROGEN RESPONSE LATE: 1/1
mock
6
24
48
hpi

Figure S17

Input Reads	Post filtering	Sample (Replicate)	Post split	After rRNA Removal	Uniquely mapping	Multi-mapping	Too many mapping	Mapped to SARS2	average input/mapped read length	Successfully Annotated
240119926	113512372	Mock-24 hpi (1)	18556130	12531252	4414181	2931147	1121087		30/30.39	3626181
		Mock-48 hpi (1)	15268068	9110461	3502306	2406928	1254006		30/30.51	2880349
		Mock-72 hpi (1)	22968629	9812576	3599181	3236894	2157977		30/30.96	2955853
		SARS2-24 hpi (1)	27048479	15329273	3515977	5008162	1236987	441312	29/28.92	2551729
		SARS2-48 hpi (1)	22153135	11600758	2847544	2505902	1614050	2099541	30/29.13	1727442
		SARS2-72 hpi (1)	7932753	5073911	661869	2846591	397944	205771	26/26.93	320947
284101233	236485610	Mock-24 hpi (2)	37263056	23908072	2302059	13609879	6711424		29/29.79	501818
		Mock-48 hpi (2)	32581794	20005244	3509329	9430008	6037787		29/30.58	1952500
		Mock-72 hpi (2)	36353119	20697301	2042733	11283854	5479310		29/29.27	600854
		SARS2-24 hpi (2)	48602708	24784599	3685011	10174801	6376524	3032246	28/28.27	674390
		SARS2-48 hpi (2)	33969369	22335764	5177096	6073398	3612968	938445	28/28.49	2708996
		SARS2-72 hpi (2)	357375	205990	33058	75522	80661	69651	22/21.72	9620

Table S1. Ribosome profiling sequencing data statistics from Vero cells infected with SARS-CoV-2 at MOI: 0.1 pfu/cell.

Sample (Replicate)	Total reads	Uniquely mapping	Multi-mapping	Too many mapping	Mapped to SARS2	Successfully Annotated
Mock-24 hpi (1)	16048877	11413147	2630393	96339	59	11413147
Mock-48 hpi (1)	31612110	20002220	2778616	102813	11	20002220
Mock-72 hpi (1)	31952785	22320398	3732850	93381	5690	22320398
SARS2-24 hpi (1)	24121125	12909565	2385337	94751	5460088	12909565
SARS2-48 hpi (1)	32038486	5744279	1044482	238260	23016982	5744279
SARS2-72 hpi (1)	35236256	20231898	3693507	89574	9809262	20231898
Mock-24 hpi (2)	53793235	46438482	6620570	91230	9997	1968195
Mock-48 hpi (2)	47305437	38324150	8204723	87923	338	1805809
Mock-72 hpi (2)	48680470	40742009	7321941	68043	74	1893306
SARS2-24 hpi (2)	44708066	8578965	1204848	13755	33552464	334906
SARS2-48 hpi (2)	53161052	6493865	1288835	20240	43222520	154923
SARS2-72 hpi (2)	29667661	7382521	807606	23561	18796772	189256

Table S2. RNA-seq data statistics from Vero cells infected with SARS-CoV-2 at MOI:0.1 pfu/cell.

Input Reads	Post filtering	Sample (Replicate)	Post-split	After rRNA Removal	Uniquely mapping	Multi-mapping	Too many mapping	Mapped to SARS2	average input/mapped read length	Successfully Annotated
311081973	284076850	Mock (1)	14980667	10468680	2332999	5042224	1944977		33/33.94	741593
		2hpi (1)	27948924	22987682	4611214	12532389	4660725	1103692	32/34.08	1092933
		6hpi (1)	43526992	31134860	6217750	15596849	6093470	1551175	33/34.69	1462573
		12hpi (1)	37963432	26927124	4503233	10892917	4384290	5832731	34/31.17	1159517
		24hpi (1)	24746845	18792952	2460916	6608054	2435334	5858205	31/30.97	579551
		48hpi (1)	47283375	32729127	5341138	6459001	2412853	15287830	34/30.21	1479158
		Mock-HT (1)	9112514	8438963	994059	4777203	2058895		29/27	121991
		2hpi-HT (1)	7082983	5896103	936276	3289668	1010619	691198	29/29.26	169394
		6hpi-HT (1)	18740076	15280202	2883116	8218937	3316821	585565	33/34.38	409827
		12hpi-HT (1)	19310811	12901743	2312025	4882964	1837394	3491991	33/33.86	635033
		24hpi-HT (1)	29678661	21459301	2792375	7756678	2698415	8634953	33/31.96	686946
		48hpi-HT (1)	14199519	10678404	1385954	4241454	783749	3039381	30/29.81	333460
302437108	252792018	Mock (2)	23882901	14876437	1593575	8022889	4456008		29/28.8	513234
		2hpi (2)	19952834	9464529	1216490	5498407	2357078	66373	29/29.46	632221
		6hpi (2)	21574214	9619099	2080250	3646810	2207937	1182070	29/29.51	1517931
		12hpi (2)	50510944	17377874	3061812	7240744	5017851	1981913	29/29.25	2024693
		24hpi (2)	38403494	11341635	3541582	4081631	2366571	1070940	28/29.14	869048
		48hpi (2)	25175115	14942682	2431154	3996162	2864413	1548449	29/28.34	168514
		Mock-HT (2)	8369058	3752674	457124	2059322	953044		27/28.89	640700
		2hpi-HT (2)	11915163	5605698	996293	2799659	1467487	50089	28/29.6	799494
		6hpi-HT (2)	13866165	6852270	1180711	2971693	2012911	531969	29/29.22	880599
		12hpi-HT (2)	26438207	10749682	1648622	4807596	2396330	1028862	28/28.54	547327
		24hpi-HT (2)	13571409	6799631	942796	3822987	1295491	376636	28/28.1	110219
		48hpi-HT (2)	5224843	3311123	309371	1901201	402832	39080	24/24.39	2914659

Table S3. Ribosome profiling sequencing data statistics from Vero cells infected with SARS-CoV-2 at MOI: 2 pfu/cell.

Sample (Replicate)	Total reads	Uniquely mapping	Multi-mapping	Too many mapping	Mapped to SARS2	Successfully Annotated
Mock (1)	37338927	31386146	5097968	60972	137	24411347
2hpi (1)	39713421	32167841	6635685	93605	5407	23438814
6hpi (1)	40516822	25114962	4525106	289009	9282471	18691668
12hpi (1)	37495946	10030544	1485647	15536	24273710	7650043
24hpi (1)	33692344	7288444	1118072	12573	23763640	5373931
48hpi (1)	49883029	9347159	1506486	27129	35156367	5806389
Mock-HT (1)	41732306	35407035	5590106	67501	342	27359651
2hpi-HT (1)	44082008	35280488	7788544	104779	6530	25541881
6hpi-HT (1)	45287025	28567578	4746019	55177	10551939	21754880
12hpi-HT (1)	38446206	9752825	1517583	16417	24821029	7526819
24hpi-HT (1)	39400410	7611935	1461503	306045	27505404	5417568
48hpi-HT (1)	50666409	8922574	1460623	31493	36519410	5573917
Mock (2)	37957138	30881275	6510403	68029	3244	21996800
2hpi (2)	36931129	30307432	6062939	67821	15067	21302828
6hpi (2)	35739671	12063334	1605738	20351	20925729	8596919
12hpi (2)	35311033	6470764	964035	18383	26505428	4630209
24hpi (2)	37104973	6513153	1111441	18498	28093183	4456958
48hpi (2)	42559697	4312593	529394	30146	34667088	1395334
Mock-HT (2)	37169747	29712344	6712049	71090	1100	21043171
2hpi-HT (2)	36268071	29846077	5793295	71890	11623	21047522
6hpi-HT (2)	37249573	12149668	1609833	19346	22215946	8760261
12hpi-HT (2)	38131757	8689865	1195175	15108	26884923	6215283
24hpi-HT (2)	39217273	8648495	1279753	20230	27889992	6086821
48hpi-HT (2)	37002102	5245805	605373	15322	28210143	1731200

Table S4. RNA-seq data statistics from Vero cells infected with SARS-CoV-2 at MOI: 2 pfu/cell.

Input Reads	Post filtering	Sample (Replicate)	Barcode splitting	Post rRNA Removal	Uniquely mapping	Multi-mapping	Too many mapping	Mapped to HIV-1	average input/mapped read length	Successfully Annotated
132858214	128522303	D1 (1)	7101140	5580026	1102964	2060579	1746294		32/33	667418
		D1 (2)	7798062	6235670	1294570	2293363	2012644		32/32.51	856489
		D2 (1)	16709968	11754019	2394829	4352369	3995087		32/32	1572955
		D2 (2)	26637844	18965602	4027477	7593265	6387969		31/31.5	2860211
		D1+HIV(1)	21586713	16868602	3852355	6008176	6147839	58291	31/31.94	2896027
		D1+HIV(2)	18173066	14643680	2848808	6687803	4470512	20468	31/31.82	2093160
		D2+HIV(1)	5205872	3519549	859274	1333760	935731	2750	31/31.52	661646
		D2+HIV(2)	24724089	18546729	3535632	8090065	6028637	17062	31/31.35	2498892

Table S5. Ribosome profiling sequencing data statistics derived from primary CD4+ T-cells infected with HIV-1.

Sample (Replicate)	Total reads	Uniquely mapping	Multi-mapping	Too many mapping	Mapped to HIV-1	Successfully Annotated
D1 (1)	20269815	16369761	3410629	91242		13350127
D1 (2)	17116347	13933060	2772236	73881		11423077
D2 (1)	13812584	11094042	2384786	59683		9185642
D2 (2)	16505434	13325514	2786310	68489		11084833
D1+HIV (1)	24954570	19121960	3810089	93496	1316706	14289511
D1+HIV (2)	17196463	13666425	2833187	71674	262213	11115813
D2+HIV (1)	13974451	11131234	2413665	60807	83150	9116782
D2+HIV (2)	12881842	10353187	2078523	55890	134218	8374759

Table S6. HIV-1 RNA-seq data statistics derived from primary CD4+ T-cells infected with HIV-1.

Gene ID (hpi)	Genome Position	Start Codon	Start	Stop	TisType	TIS Group	TIS Counts	Fisher Pvalue	AA Sequence
S (6)	21867-21924:+	AGG	305	362	Internal	0	298	9.39E-07	RLDFWYYFRFEDPVPTYC*
E (6)	26388-26472:+	GTG	144	228	Truncated	0	359	1.10E-06	VSLVKPSFYVYSRVKNLNSSRVPDLLV*
M (6)	26710-26872:+	TTG	188	350	Internal	1	663	1.78E-09	LFCACCCLQNKLDHRWNCYRNGLSCRLDVAQLLHCFFQTVCAYAFHVVIQSRN*
M (6)	26522-27191:+	ATG	0	669	Annotated	1	2393	1.19E-07	-
S (12)	21867-21924:+	AGG	305	362	Internal	0	3845	7.85E-08	RLDFWYYFRFEDPVPTYC*
S (24)	21867-21924:+	AGG	305	362	Internal	0	8900	1.10E-06	RLDFWYYFRFEDPVPTYC*
M (24)	26657-27191:+	TTG	135	669	Truncated	1	10606	3.81E-08	LYIIKLIFLWLLWPVTLACFVLAAVYRINWITGGIAIAMACLVGLMWLSYFIASFRLFARTRSMWSFNPETNILLNVPLHGTILTRPLLESELVIGAVILRGHLRIAGHHLGRCDIKDLPKEITVATSRTLSYYKLGASQRVAGDSGFAAYSRYRIGNYKLNTDHSSSSDNIALLVQ*
N (24)	28273-29533:+	ATG	0	1260	Annotated	3	16308	1.03E-13	-

Table S7. Alternative translation initiation sites in SARS-CoV-2

Input Reads	Post filtering	Sample	Post-split	After rRNA Removal	Uniquely mapping	Multi-mapping	Too many mapping	Mapped to SARS2	average input/mapped read length	Successfully Annotated
308599155	119266100	Mock	25072235	15945881	2041440	9123215	4173203	80	30/29.9	1061875
		6 hpi-MOI 0.5	12311716	6608269	983034	3625454	1487254	54	28/30.8	503754
		24 hpi-MOI 0.5	12787860	7800876	1144968	4169483	2024458	368	27/31	737704
		48 hpi-MOI 1	14759739	7902584	1114747	4350379	1868168	1249	28/31.1	748352
		72 hpi-MOI 0.5	15027944	9048779	1297674	4578063	2210898	1769	27/30.5	825972
		6 hpi-MOI 1	20194457	14194684	2065907	8457729	3328549	395	31/30.8	806193
		24 hpi-MOI 1	10316817	5766743	848917	3219550	1303416	291	27/31.2	563571
		48 hpi-MOI 1	9134078	4430741	758036	2391285	1013765	3429	29/33	418854

Table S8. Ribosome profiling sequencing data statistics from SARS-CoV-2 infected HBEC cells grown at ALI.

Sample	Total reads	Uniquely mapping	Multi-mapping	Too many mapping	Mapped to SARS2	Successfully Annotated
Mock	28366491	25311325	2811636	17644	232	20264703
6 hpi-MOI 0.5	29463488	26131689	3089144	20206	446	20480479
24 hpi-MOI 0.5	27100847	23809149	3010618	17839	42072	18990623
48 hpi-MOI 0.5	29043346	25844515	2892927	19871	87624	20135178
72 hpi-MOI 0.5	32065372	28369753	3272020	19289	161387	22898524
6 hpi-MOI 1	31640182	28129394	3262290	20587	820	22289459
24 hpi-MOI 1	32742734	29230705	3169512	22209	48104	23442713
48 hpi-MOI 1	31835471	28026215	2768743	20868	753566	21740521

Table S9. RNA sequencing data statistics from SARS-CoV-2 infected HBEC cells grown at ALI.

Gene ID (hpi)	Tid	GenomePos	Codon	Start	Stop	TisType	Fold Change	DiffPvalue
S100A4 (2)	XM_007977084.1	chr20:10259218:+	ATG	123	429	Annotated	1420	4.67E-245
LOC103221995 (2)	XM_007973466.1	chr17:45986443:+	ATG	564	975	Annotated	407.07	4.08E-224
C11H12orf75 (6)	XM_008004514.1	chr11:100538651:+	CTG	317	410	Internal:CDSFrameOverlap	0.0053	4.20E-101
S100A10 (6)	XM_007977149.1	chr20:11698268:+	ATG	493	787	Annotated	0.0027	1.15E-74
C11H12orf75 (12)	XM_008004514.1	chr11:100538651:+	CTG	317	410	Internal:CDSFrameOverlap	0.0025	1.19E-112
S100A10 (12)	XM_007977149.1	chr20:11698268:+	ATG	493	787	Annotated	0.0099	4.81E-66
OST4 (12)	XM_007971186.1	chr14:80546921:+	ATG	112	226	Annotated	0.000	3.86E-64
C11H12orf75 (24)	XM_008004514.1	chr11:100538651:+	CTG	317	410	Internal:CDSFrameOverlap	0.0077	1.76E-93
S100A10 (24)	XM_007977149.1	chr20:11698268:+	ATG	493	787	Annotated	0.02444	1.28E-51
BNIP3L (24)	XM_007961972.1	chr8:24497429:+	ATG	119	779	Annotated	0.0043	3.29E-51
OST4 (24)	XM_007971186.1	chr14:80546921:+	ATG	112	226	Annotated	0.0123	6.36E-47
LOC103215555 (24)	XM_007962062.1	chr8:27134847:-	ATG	185	740	Annotated	0.0141	2.64E-29
ID3 (24)	XM_007980074.1	chr20:109120977:+	ACG	575	929	Internal	0.02490	9.64E-25
EXOSC7 (24)	XR_495184.1	chr22:6479255:+	CTG	609	840	Novel	0.00186	1.35E-21
EXOSC7 (24)	XM_007983908.1	chr22:6479255:+	CTG	609	972	Internal	0.0019	1.35E-21

Table S10. Alternative translation initiation sites in host.